(1)

Cen Aの硬X線での観測と放射機構への示唆

平成4年12月博士(理学)申請

東京大学大学院理学系研究科
物理学専攻
宮崎聡

Hard X-ray Observation of Cen A and Implications on the Emission Mechanisms

Satoshi MIYAZAKI
University of Tokyo
7-3-1 Hongo, Bunkyo-ku, Tokyo 113, Japan

February 14, 1993

(1)

Cen Aの硬X線での観測と放射機構への示唆

平成4年12月博士(理学)申請

東京大学大学院理学系研究科
物理学専攻
宮崎聡

Hard X-ray Observation of Cen A and Implications on the Emission Mechanisms

Satoshi MIYAZAKI
University of Tokyo
7-3-1 Hongo, Bunkyo-ku, Tokyo 113, Japan

February 14, 1993

Abstract

We studied hard X-ray/γ-ray emission from Cen A (NGC 5128) in a balloon experiment with a low background detector (Welcome-1) in Brazil. The energy spectrum of CenA is obtained from 40 keV to 600 keV. We combined the energy spectrum obtained by the Ginga satellite in a similar state. The combined spectrum indicates that there is a break at 184 $\pm$ 22 keV. The spectrum is fitted to the broken power law model with the photon index of $\alpha_1 = 1.79$ up to 184 keV and $\alpha_2 = 3.7^{+0.9}_{-1.6}$ above the break.

Contents

Chapter 1

Introduction

Active Galactic Nuclei(AGN) are one of the most fascinating objects in astrophysics. Numerous observations have been extensively made for these extra-galactic objects from radio to gamma-ray energies. Nevertheless, they probably belong to the least understood class of celestial objects.

The spectrum is not explained by simple black body radiation. Over a wide energy interval from radio to gamma-ray, AGN emit a huge amount of radiation that sometimes reach up to 10^{47}erg/s. This suggests that a single physical process, thermal or non-thermal processes, cannot explain the emission mechanism of AGN.

In general, the time scale of intensity variation becomes shorter and its amplitude becomes larger as the energy of photons increases. This fact implies that higher energy photons, X-rays and gamma-rays, are more likely to be from the central engine of AGN if one estimate the size of emission region from the time scale.

From X-ray observations, AGN are commonly believed to have a super massive blackhole with $M \sim 10^8 M_\odot$ surrounded by an accretion disk. To maintain the huge luminosity (10^{42} $\sim 10^{46}$erg/sec in X-ray range) stably emitted , such an enormous mass is required. The Eddington limit provides an estimate to the minimum mass of AGN, which is $10^4 \sim 10^8 M_\odot$. This mass is concentrated in a very small region that is inferred to be $10^{13} \sim 10^{15}$ cm from the time variation. The most probable candidate of this compact system is naturally the super massive blackhole [1]. The recent Ginga observation strongly supports the blackhole model of the AGN presenting several

similarities between the galactic blackhole candidates and the AGN [2].

The primary energy source of the radiation from AGN is supposed to be the conversion of gravitational energy in the accretion of material onto the blackhole. The major problem is, however, to find how the potential energy is transferred to the radiation. Several possible models have been proposed based on thermal Comptonization process [3] and Synchrotron Self Compton model [4].

One of the most remarkable results obtained by X-ray observations is that Seyfert galaxies have universal spectra, consisting of a power law with photon index $\alpha \approx 1.7$, at least in the energy range 2 to 100 keV; this suggests that a common emission mechanism exists over a number of objects. The featureless continuum spectra in the X-ray band, however, does not give tight constraints upon the emission mechanism. It is important to search for other spectral features, *e.g.* a break in the power law. There have been indirect evidences of such breaks if one compared X-ray data with the results at higher energies, *i.e.* upper limits by SAS-2 [5] and COS-B [6]. Until this study, the break has generally been thought to occur somewhere below $\sim$ 10 MeV. From the location of the break and the power law index, the basic parameters of the physical condition in the radiation environment can be determined. Therefore, it is essential to study AGN spectra in the hard X-ray/gamma-ray range to unravel the emission mechanism of the AGN.

In hard X-ray and low energy gamma-ray region, it is however difficult to observe celestial objects because the the signal from the objects is generally weak compared with the background. The sensitivity of a celestial hard X-ray/gamma-ray detector has been limited by its signal to noise ratio. To detect the emission of hard X-ray/gamma-ray at the required level, one needs a detector which can realize very low background rate with appropriate detector size. Thus, we have developed a new balloon-borne detector, "Welcome-1".

Centaurus A (Cen A) is one of the nearest AGN, and thus, it is one of the best candidates for the study in the hard X-ray/gamma-ray region. We have observed hard X-ray/gamma-ray emission from Cen A in a balloon experiment with Welcome-1 in Brazil. Furthermore, to examine the X-ray spectra of Cen A we have analyzed

the data obtained by Ginga satellite.

In Chapter 2 we review the results of past observations of AGN and the scientific issues related to these observations. Theoretical models proposed to explain the emission are also briefly discussed. In Chapter 3 and Chapter 4 we describe the Welcome-1 detector. In Chapter 5, we discuss the background which is the major concern in the observation in the hard X-ray/gamma-ray region. In Chapter 6 we analyze the data obtained by Welcome-1 to reconstruct the incident hard X-ray spectrum. Chapter 7 deals with the observation by Ginga. In Chapter 8 we examine the spectrum obtained by Welcome-1 and by Ginga. Based on the results the implications on the emission mechanisms are discussed.

Chapter 2

Review of AGN Observations and Theoretical Models

The active galaxies are generally considered to have a compact core or nucleus, which releases the energy of 10^{42}-10^{46} erg/s and causes a violent activities of the galaxy. Such Active Galactic Nuclei (AGN) have been studied extensively from radio to gamma-ray energies. The AGN are often classified into Seyfert galaxies, radio galaxies, QSOs, and BL Lacertae objects, based on the observed properties, mainly, of the optical region. The central engine of the AGN is however believed to have a common structure as is described in Section 2.2.

2.1 Active Galactic Nuclei

The spectra of AGN are quite different from those of the ordinary stars. The spectrum at radio, IR, Optical, UV is characterized by a quasi-power law. The detection of polarization at radio indicates that the emission originates from synchrotron radiations at optically thin matters. Underlying emission lines from a variety of ionization states have been also observed. The spectrum of some AGN has a bump around UV region, (UV bump) which is described by a thermal emission whose temperature is $10^4 \sim 10^5$K. tX-ray spectrum is also characterized by a power law whose photon index is, however, harder than that of optical region. The power law component

extends at least up to 100 keV. Figure 2.1 is the energy spectra of several AGN from radio to gamma-rays. It is noticeable that the power output for these objects appears to take its maximum in X-ray to gamma-ray range.

In general, the time scale of the intensity variation becomes shorter and its amplitude larger, as the energy of photons increases. If one estimates the size of emission region (R) from the time variation (Δt) as $R \sim c\Delta t$, it suggests that X-rays and gamma-rays are emitted from the region closer to the central engine of AGN. This fact, together with the fact that power output is peaked in these energy range, implies that higher energy photons are directly originated in the central engine.

2.2 Blackhole Model of AGN

A feature common to all AGN is a large luminosity (10^{40}-10^{47}erg/s). For having a stable emission at this huge luminosity, the outward pressure of radiation has to be balanced with the inward gravitational attraction. The Eddington limit (L_{edd})gives the relation between the luminosity and the mass of the central object expressed as,

$$L_{edd} = \frac{4\pi cGMm_p}{\sigma_T} = 1.26 \times 10^{38}(\frac{M}{M_\odot})\text{erg/s}, \tag{2.1}$$

where M is the mass of central object, m_p is the proton mass, σ_T the Thomson cross section and $M_\odot$ the solar mass. The lower limits of source masses calculated from the Eddington luminosity range from $\sim 10^2 M_\odot$ for low luminosity Seyfert 1 galaxies to $\sim 10^9 M_\odot$ for high luminosity QSOs.

Observed time variability of AGN implies that the source is extremely compact. A direct evidence of the compactness comes from comparing their luminosity with their minimum variability time scales. Figure 2.2 compares the 2-10 keV luminosity of several AGN with their minimum X-ray variability times scales. The variability time scale Δt is the minimum time period over which the source flux changes by a factor of two. The lowest value is for the galactic black hole candidate, Cyg X-1. One can see the scale invariance which implies the existence of a common structure.

The compactness together with the scale invariance has motivated many models of AGN that assumes a central super massive black hole. In these models, the release of

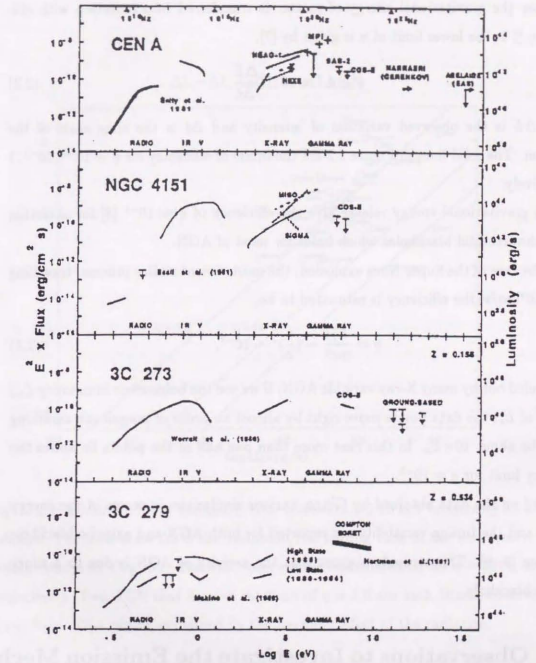

Figure 2.1: Energy Spectra samples of active galaxies from radio to gamma-rays. Flux×energy^2 gives energy output of the source per decade of photon energy.

gravitational energy is supposed to be essential source of emission from AGN, which is supported by the following argument.

When the gravitational energy of matter is transferred into radiation with efficiency $\eta \leq 1$, the lower limit of η is given by [7],

$$\eta \geq 4.7 \times 10^{-43} \frac{\Delta L}{\Delta t}. \tag{2.2}$$

where ΔL is the observed variation of intensity and Δt is the time scale of the variation. The solid lines in Figure 2.2 are the limits of efficiency for $\eta = 10^{-3}, 10^{-1}, 1$ respectively.

The gravitational energy release give the efficiency of $\eta \approx 10^{-1}$ [8] for accretion onto Schwartzshild blackholes which holds for most of AGN.

In the case of the Super Nova explosion, the most violent stellar process, travelling at $v \sim 10^4$km/s, the efficiency is estimated to be,

$$\eta = \frac{E_K}{mc^2} \sim (\frac{v}{c})^2 \sim 10^{-3}, \tag{2.3}$$

and is ruled out by many X-ray variable AGN. If we use the bolometric luminosity L_{bol} instead of L_x, the data points move right by almost an order of magnitude assuming L_{bol} to be about $10 \times L_x$. In this case more than one half of the points lie above the efficiency limit for $\eta = 10^{-3}$.

Based on the data obtained by Ginga, various similarities in terms of the energy spectra and the timing variability are reported for both AGN and galactic blackhole candidate [2, 9]. This strongly suggest that the activity of AGN is due to a super massive blackhole.

2.3 Observations to Investigate the Emission Mechanism of AGN

Higher energy photons (X-rays and gamma-rays) is likely to be direct and un-reprocessed emission from central engine. The observational facts indicates that they are emitted

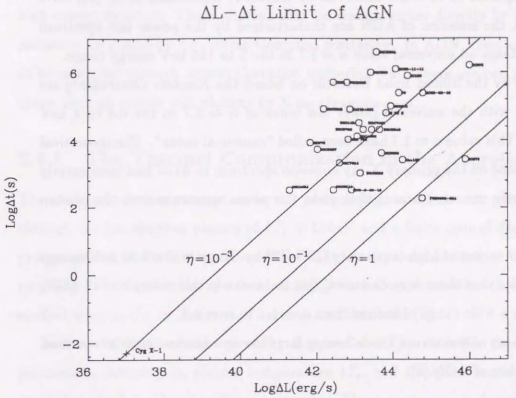

Figure 2.2: Minimum X-ray variability time scale versus 2-10 keV luminosity for active galaxies. The time-scale Δt is the minimum two folding time of the luminosity. The lowest value is for Cyg X-1. The solid lines are the efficiency limit for $\eta = 10^{-3}, 10^{-1}, 1$ respectively. Two AGN that lie over the limit of $\eta = 1.0$ are both Blazar observed in X-ray flare. This can be explained by the beaming effect of the radiation.

from the region close to the central engine of AGN, super massive blackhole. Therefore, the spectra in the X-ray/gamma-ray range give us a direct information about the emission mechanism of AGN. Number of spectral observations have been carried out mostly in the X-ray region below 100 keV.

Using the spectra of 11 AGN observed by HEAO-1, Rothschild *et al.* [10] have concluded that the emission of AGN are characterized by the power law spectrum and the index takes an universal value $\alpha \approx 1.7$ in the 2 to 165 keV energy range.

Data taken by the Silicon Solid Detector on board the *Einstein Observatory* are also consistent with the universal power law index of $\alpha \approx 1.7$ in the 0.4 to 4 keV range [11, 12]. This value $\alpha \approx 1.7$ have been called "canonical index". The theoretical studies so far done on the primary X-ray emission spectrum in AGN had been mainly devoted to clarify the mechanisms that yield the power spectrum with the photon index of $\alpha \approx 1.7$.

The spectral survey of high luminosity QSO [13] by Ginga in the 2-30 keV energy band has revealed that there is no canonical spectral index in their sample of 13 AGN; instead there is a wide range of indices from $\alpha = 1.1$ to $\alpha = 2.3$.

From the X-ray observations, the following facts has now become clear as common spectral properties of AGN [9],

1. AGN have the power law spectrum that extends at least up to 100 keV.
2. The intensity of the power law components show large and irregular changes.
3. The power law slope for each individual source remain stable even the absolute intensity changes largely.

The deviations in photon indexes however implies that the index itself might not represent a particular emission mechanism of AGN. Another clues are required to investigate the central engine of AGN.

2.4 Emission Mechanism of AGN

To investigate how AGN generate the radiation power, it is important to study the power law emission. In general, continuum emission above a few 10 keV from astronomical sources above a few 10 keV are primarily due to the non-thermal process by high energy electrons. These photons may be created either directly by synchrotron radiation, or indirectly by inverse Compton scattering. In AGN, they are supposed to be produced through inverse Compton scattering [14]. There are two possble processes that up-scatter soft photons to X-rays/gamma-rays.

2.4.1 The Thermal Comptonization in the Accretion Disk

The unsaturated Comptonization is the process [15], in which soft photons evolve through the hot electron plasma of $kT_e > 10keV$ and a finite optical depth τ. This process gives a power law spectrum followed by an exponential decline. The break is naturally introduced in the spectrum at $3kT_e$/ Such Comptonization model has been studied analytically by Sunyaev, Titarchuk and Zdziarski [3].

In the analytical solution given by Sunyaev and Titarchuk [3], there are three parameters, intensity I_0, plasma temperature kT_e, and Compton scattering optical depth (τ) which is related to the γ parameter. The γ parameter is described as,

$$\gamma = \pi^2 m_e c^2 / 3(\tau_0 + 2/3)^2 kT_e \tag{2.4}$$

where $m_e c^2$ is the electron rest mass energy. Figure 2.3 shows the spectra obtained from the model with various plasma temperature at $\tau = 5$. The output spectrum is weakly dependent on the spectrum of soft photons if $\tau > 1$.

In the thermal Comptonization model, the accretion disk is a possible reservoir of the high temperature electron plasma. To explain the hard X-ray photons of ~100 keV, T_e is required to be $10^8 \sim 10^9$ K. Soft photons to be scattered are supplied by external thermal sources, *e.g. UV bump*, or be produced by the thermal electrons via bremsstrahlung or cyclotron/synchrotron radiation inside the accretion disk if there exists the magnetic field.

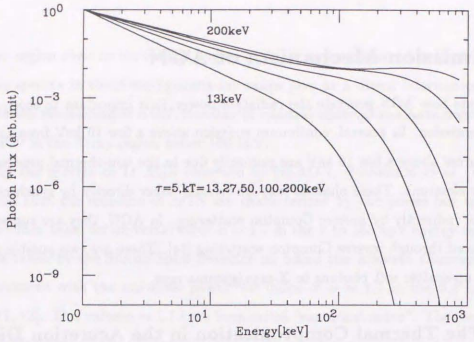

Figure 2.3: Spectra from Sunyaeve and Titarchuk Comptonization Model.

When the radiation emerges from the inner part of the accretion disk, a region of a few gravitational radii R_s ($= \frac{2GM}{c^2}$), the maximum ion temperature can be estimated by assuming the whole infalling kinetic energy is converted to the energy of protons. According to the calculation by Shakura *et al.* [16], the inner most radii of accretion disk is $\sim 3R_s$ for the non-rotating blackhole and the energy of proton becomes $kT_p \approx \frac{GMm_p}{3R_s} \approx$ 100MeV. In the fully ionized plasma, ions and electrons are coupled by the collisional energy exchange. Electrons are heated its energy through electron-proton scattering and are cooled by interaction with soft photons in the inner disk.

The electron temperature are determined from the balance of these processes. The important parameters, kT_e and τ are determined by the observation of the spectra. While a few extragalactic sources, including NGC4151, 3C273, Cen A, 3C279 and Mkn 421, have been detected at energy $\sim$ 100 keV, their spectra have not yet been measured accurately enough to determine whether the break exists.

2.4.2 Synchrotron Self Compton (SSC)

If non-thermal relativistic electrons are continuously injected with power law energy distribution extending up to $\gamma_{max} \gg 1$, the radiation spectrum by the inverse Compton scattering also shows a power law shape [15]. A possible scenario to produce the non-thermal relativistic electrons has been suggested by Protheroe and Kazanas [17]. In their scenario protons undergo first order-Fermi acceleration during infall onto a massive black hole. The non-thermal electrons are produced as secondary particles in nuclear interactions of the protons.

If the target photons to be scattered are produced as synchrotron photons by the same non-thermal electrons, the model is called "Self Synchrotron Compton Model" (SSC model) [4]. This model predicts two-component photon spectrum: the initial synchrotron spectrum in the radio to IR band and the Compton scattered spectrum in the X-ray/gamma-ray band. The X-ray spectrum is expected to mimic the shape of the synchrotron spectrum but is shifted to higher energies. Figure 2.4 is an example of such two-component spectrum calculated by Band and Grindlay [18].

In the frame work of the SSC model, the correlation between radio/IR and X-ray intensity is required. Multi-frequency observations of Blazars (BL Lacertae Objects and OVV QSOs) have revealed that this type of AGN shows the correlated variation between X-ray emission and radio and IR emission [19, 20]. This suggests that the SSC model is the most probable model at least for Blazars. The emission from Blazar are, however, supposed to come from the jet with substantial beaming factor that enhance the SSC component [21].

2.5 Importance of Observation in the Hard X-Ray Range

The observations in X-ray (<100 keV) band are little help in studying the emission mechanism of the continuum radiation; a smooth power law spectrum could be produced equally well by several alternative processes. We need another clues to study

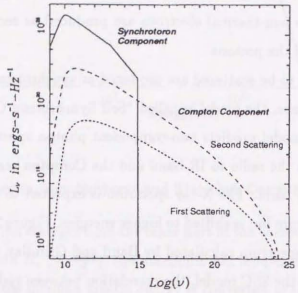

Figure 2.4: Example of calculated energy spectrum based on SSC model by Band and Grindlay[18]. In the calculation they assumed the "broken" electron distribution ; for $\gamma \geq 4500$ electrons the energy index steepen by 1 due to losses. The parameter are magnetic field of 0.2 G, electron distribution $dn_e = 1.5 \times 10^6 \gamma^{-2.4} d\gamma$ for $1 \leq \gamma \leq 4500$ in a source of radius 10^{15}cm. Solid line is the synchrotron spectrum, the line with the small dashes results from the first scattering, and the line with the large dashes from the second.

the emission mechanism of AGN such as a break in the spectrum.

Since the onset of pair-production processes makes it very unlikely that a thermal plasma will have an electron temperature of >a few MeV, photons produced by thermal Comptonization should have a break in their spectrum in the hard X-ray/gamma-ray range ($<\sim$ 10 MeV). On the other hand, photon spectra produced by the relativistic electrons is expected to have gradual decline. Therefore the fundamental question of whether the emissions from AGN are produced by thermal electron plasma or relativistic electrons may be resolved by the observations of the break in their hard X-ray spectra. In fact, the break is indirectly suggested from upper limits set by SAS-2 [5] and COS-B [6] for many AGN.

The exact determination of the energy where the spectra steepen has important consequences, not only to construct the physical models of AGN, but also to assess their contribution to the extragalactic diffuse X-ray background [22]. Figure 2.5 shows the energy spectrum of the diffuse X-ray background. The upper limit of contribution from AGN obtained by Ginga [23] is shown in the figure. Simple extrapolation of the limit already accounts for the total flux around MeV region while in the X-ray region below 30 keV the limit is merely 30%. If the diffuse background can be explained by the superposition of the emission from AGN, there must exist break in AGN spectra between 100 keV and 1 MeV.

2.6 Review of the Cen A Observation

Centaurus A (Cen A) is one of the best candidate for the study in the hard X-ray/gamma-ray region because it is one of the nearest AGN. Thus, we have observed hard X-ray/gamma-ray emission from Cen A in a balloon experiment with Welcome-1 in Brazil. In this section, we review the results of observations carried out so far.

2.6.1 Radio Galaxy Cen A

Cen A is a giant elliptical radio galaxy with a dust lane in its center which obscures the central regions. The appearance of Cen A is interpreted as a result of a merger of

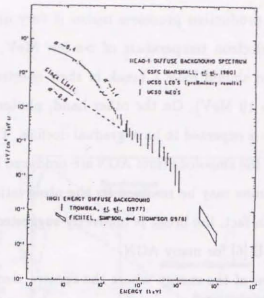

Figure 2.5: Cosmic X-ray Background

an elliptical galaxy and a spiral galaxy. The remainder of the spiral forms the dust band in the center of Cen A. Due to the heavy absorption ($n_H \sim 10^{23}/\mathrm{cm}^2$), no broad line emission has been observed from this object, and IUE observations showed no significant UV flux. VLBI observation revealed the radio structure of nucleus of Cen A [24]. The nucleus consists of compact self-absorbed core, a jet containing a set of three knots and a very long narrow component elongated along the same position angle as the knots.

Cen A is one of the first extra-galactic object observed by X-ray [25]. A detail X-ray map of Cen A was obtained from Einstein Observatory [26] which consists of variable compact nucleus, X-ray jet almost aligned with NE(north east) radio lobe and diffuse source extending several arc minutes around the nucleus.

2.6.2 Energy Spectrum of Cen A in X-ray/gamma-ray

For last two decades, the energy spectra have been obtained by a number of workers, most of them are below 100 keV. Mushotzsky et al. [27] carried out the first precise

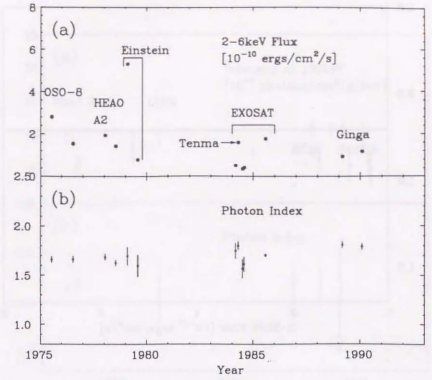

Figure 2.6: Intensity and photon index variation of Cen A (X-ray range)

observation of Cen A in X-ray range($2 \sim 60$keV). They reported the photon spectrum in the range is well characterized by a power law with a photon index of 1.66 ± 0.03 with a significant absorption due to $1.3\times 10^{23} n_H/\mathrm{cm}^2$ and 6.4 keV Fe fluorescent line with 7.1 keV absorption edge. The photon index of the power law kept stable within statistical error while the total flux varied by a factor of 2 between 1975 and 1976 [27]. Figure 2.6(a) shows the measured long-term variations of the $2 \sim 6$ keV intensity from OSO-8 up to Ginga observation, 1990. These subsequent X-ray observations shows the photon index stable at around 1.7 ± 0.1(RMS). The variations of photon indexes are shown in Figure 2.6(b). In Figure 2.7, the correlation of above two values are presented. The most remarkable change of intensity was observed by Einstein [26], which was a factor of 7 decrease between 6 months apart. Even in this case, significant change in index was not be seen.

As for the hard X-ray observation, the same plots are presented in Figure 2.8 and 2.9. Although the measurements are sparse in the hard X-ray range, the photon index tend to be stable and consistent with the value of 1.7 ± 0.1 obtained above.

Featureless power law spectrum observed in the 10-165 keV energy by HEAO

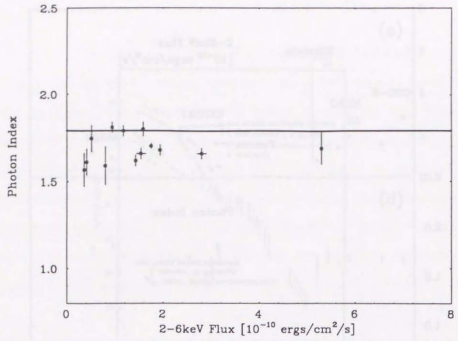

Figure 2.7: Intensity and photon index Correlation of Cen A (X-ray range)

A4 [28] was confirmed by subsequent observation by HEXE [29] in the 20-160 keV range (Figure 2.10) and POKER [30] in the 15-150 keV range. Therefore, the power law spectra measured in the X-ray range extends up to at least 100 keV and the photon index is stable at 1.7±0.1.

High energy upper limits have been given by SAS-2 [31] COS-B [32] in the range above ~ 10 MeV. This implied spectral steepening between 100 keV and ~10 MeV.

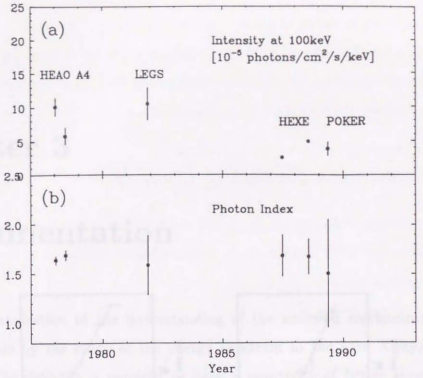

Figure 2.8: Intensity and photon index variation of Cen A (Hard X-ray range)

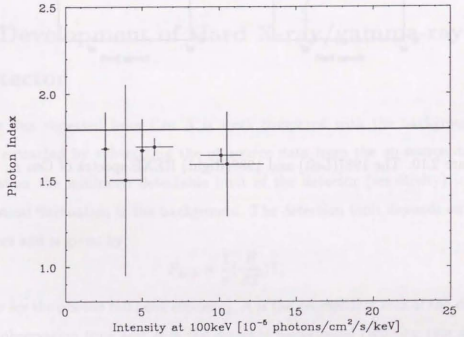

Figure 2.9: Intensity and photon index Correlation of Cen A (Hard X-ray range)

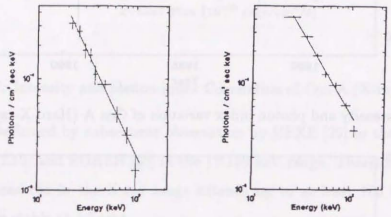

Figure 2.10: The 1987(Left) and 1988(Right) HEXE spectra of Cen A.

Chapter 3

Instrumentation

Important contribution to the understanding of the emission mechanism of Cen A can be made by the study of the energy spectrum in the hard X-ray/gamma-ray range. The detector is required to have a sensitivity of better than $\sim 2 \times 10^{-6}$photons/cm^2/s/keV at 500 keV according to the previous X-ray measurement.

3.1 Development of Hard X-ray/gamma-ray Detector

Since the flux expected from Cen A is weak compared with the background, the signal is extracted by subtracting the off-source data from the on-source data. In this situation the minimum detectable limit of the detector (sensitivity) is set by the statistical fluctuation in the background. The detection limit depends on several parameters and is given by

$$F_{min} \propto \frac{1}{\varepsilon}(\frac{B}{AT})^{\frac{1}{2}}, \tag{3.1}$$

where ε is for the photon full peak efficiency, A is the geometrical area of the detector, T is the observation time and B is the detector background counting rate per unit area.

In the balloon or satellite experiment, A is primarily set by the lifting capability of vehicle. The typical observation time is 10^4 s for the balloon experiment. Under

such circumstances, in order to attain high sensitivity, it is essential (1) to employ the detection part that has high full peak efficiency (ε) and (2) to figure out the most effective configuration to reduce the background (B). The detector used in the experiment has been developed based on these ideas.

3.2 Welcome-1 Detector Overview

The detector, called Welcome-1 is designed for the measurement in the energy range from 40 keV to 800 keV. The telescope of the detector consists a newly developed well-type phoswich counter.

The schematic drawing of the detector is shown in Figure 3.1. The telescope is attached to a platform by two bearings which allows changes in elevation angle of the telescope. The platform is also made of aluminium-honeycomb plate and has four chambers on each side. The associated electronics and batteries are mounted inside the chambers. The torque motor for azimuth control is located on the top of detector.

Total weight of the detector is 680 kg. The detector is flown by a balloon of 8.8 million ft^3 filled with hydrogen gas to reach an altitude of $\sim$ 37 km for the observation.

Table 3.1 summarizes the basic characteristics of the Welcome-1. The effective area is 740cm^2 for 122 keV and the geometrical field of view (FOV) is 7.4° (HWHM).

3.3 The Telescope

3.3.1 Well-Type Phoswich Counter

It is essential to reduce the background counting rate in order to achieve the high sensitivity. In the space environment, the background components are : (1) a contribution from the atmospheric and the diffuse cosmic photons entering through the collimator aperture, (2) the leakage of photons through a shield and (3) non-aperture contribution from the cosmic-ray activation of the detector material. In addition

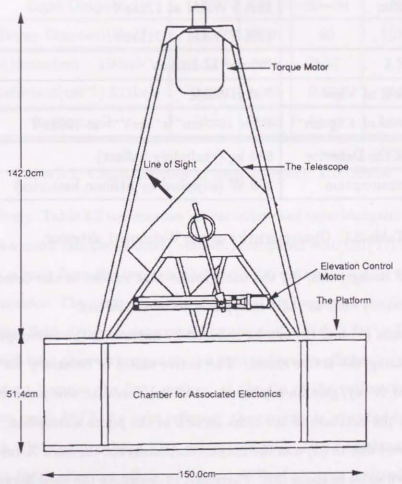

Figure 3.1: The Welcome-1 detector showing its configuration during the flight.

Primary Counters	64 Well type phoswich counters of GSO and CsI(*Tl*) combination
Anti Counters	36 CsI(*Tl*) counters
Energy Range	40 keV $\sim$ 800 keV
Energy Resolution	28% FWHM at 122keV 12% FWHM at 511keV
Effective Area	740cm^2 at 100keV
Geometrical Field of View	7.4° HWHM
Background Level at 4.5g cm^{-2}	1.5×10^{-4}cm^{-2}s^{-1}keV^{-1} at 100keV
Total Weight of the Detector	680 kg (excluding ballast)
Total Power Consumption	200 W (supplied by lithium batteries)

Table 3.1: Characteristics of the Welcome-1 detector.

to these external background, (4) the background that resides in the detection part (internal background) such as radio isotopes is to be considered

The components (1) and (2) can be reduced by narrowing the telescope aperture and/or by increasing the active shield. The active shield is necessary for the measurement of hard X-ray/gamma-ray over $\sim$ 150 keV because the passive shield is inefficient due to the decrease of the cross section of the photo absorption.

The background due to (3) was the major component for the hard X-ray/gamma-ray detectors flown so far in space [33]. Therefore, in designing the hard X-ray/gamma-ray detector it is essential to suppress this component effectively.

Figure 3.2 shows the cross-sectional view of the well type phoswich counter. A small detection part, GSO(Ce) (Gd_2SiO_5 doped by Ce), is buried deep in the well-shaped anti scintillator, CsI(*Tl*) . The size of GSO is 3.4cm × 3.4cm × 1.0cm. The counter is viewed by a single 2-inch photomultiplier tube (PMT).

GSO is the inorganic scintillator newly developed by Hitachi Chemical [34, 35]. High attenuation coefficient of GSO scintillator enables us to make detection part small. For example, the full peak efficiency of 1cm GSO and NaI(*Tl*) is 30 % and

	NaI(*Tl*)	BGO	GSO:Ce	CsI(*Tl*)
Eff. Atomic Number(Z)	50	74	59	54
Density (gcm^{-3})	3.7	7.1	6.7	4.5
Emission Wavelength(nm)	410	480	430	550
Light Output	100	12	20$\sim$30	50
Decay Constant(nsec)	230	300	60	1050
Attenuation 150keV	2.22	9.84	5.37	3.24
Coefficient(cm^{-1}) 511keV	0.34	0.955	0.674	0.47
Hygroscopic	Yes	None	None	Little

Table 3.2: Characteristics of some inorganic scintillator

10%, respectively. Table 3.2 summarizes characteristics of some inorganic scintillators. The GSO has a much fast decay time ($\sim$60nsec) compared with CsI(*Tl*) ($\sim 1\mu$sec) and therefore the signals from the two scintillator can be separated easily with the pulse shape discriminator. The protruded part of the CsI(*Tl*) works as an active collimator. The geometrical field of view is determined by the well, which is 7.4° × 7.4°(HWHM).

For the well-type phoswich counter, the light collection efficiency in the well becomes important because the light emitted at the tip of the collimation part must travel 22cm to reach PMT. As light reflector, the counter is wrapped by white plastic sheet with white paint with a high reflectance [36]. These combination provides with excellent light collection efficiency; about 95% of photons emitted at the tip is collected compared with those at the bottom.

In the Figure 3.3, the background of the GSO scintillator with and without CsI(*Tl*) well is compared. The scintillators are located inside the cave of Pb(5cm)+Cu(5cm) to measure the internal background of the scintillator. The spectrum includes a peak around 300 $\sim$ 400 keV (calibrated gamma-rays) due mostly to ^{152}Gd (natural abundance 0.2%, 2.14MeV α decay, half-life 1.1×10^{14}y). It is evident that the well-type configuration substantially reduces the gamma-rays from $\beta - \gamma$ decays of the unstable isotope. This is because the well-type configuration provides with a nearly

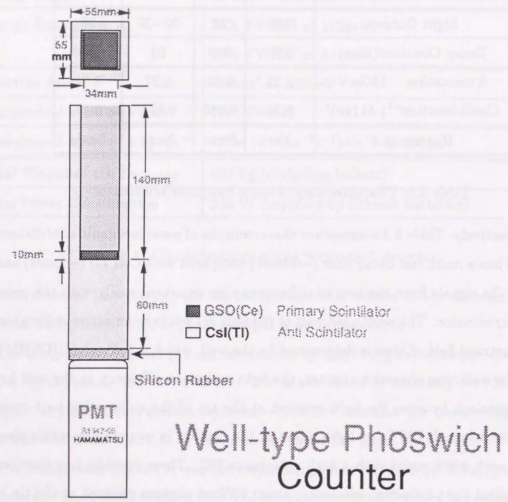

Figure 3.2: Well-Type Phoswich Counter

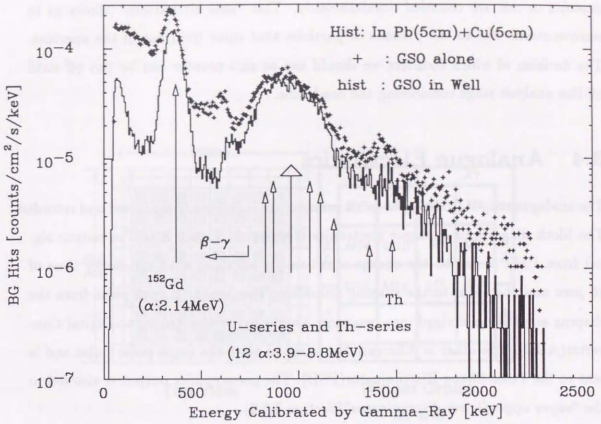

Figure 3.3: Spectra of the internal background: +, the naked GSO crystal; histogram, the GSO in the CsI(*Tl*) well

4π anti counter for the detection part. This implies the background due to the nuclear activation caused by high energy charged particles or neutrons are able to be reduced.

3.3.2 Compound-Eye Configuration (Welcome-1)

The 64 well-type phoswich counters are assembled together in an array of 8×8 matrix (Compound Eye Configuration) to enlarge a effective area. Figure 3.4 shows a cross-sectional view of the detector assembly. As additional shield for the outermost phoswich counters 36 CsI(*Tl*) anti counters surround the matrix.

The advantage of the compound eye configuration is that each counter acts not only as an usual counter but also as an active anti counter with each other. When the energy is deposited in one counter, the information whether there exists energy

deposits or not are recorded simultaneously. This "anti hit pattern" allows us to remove events due to the photons or particles that enter from out of the aperture. The decision of which counters we should use as anti counter can be put off until off-line analysis stage considering the dead time.

3.4 Analogue Electronics

The analogue output from 64 phoswich counters are individually processed and recorded. The block diagram of analogue electronics is shown in Figure 3.5. The output signal from PMT is fed to the charge sensitive pre-amplifier with the decay time of 16 μsec and then sent to the shaping amplifier. The bipolar output pulse from the shaping amplifier is divided into two ways. One is fed to the Analog to Digital Converter(ADC). The other is differentiated again to form the triple polar pulse and is sent to the Pulse Shape Discriminator(PSD). The pre-amplifier output is also fed to the "super upper/lower discriminator"(Section 3.5.2).

The output of the 36 anti counters are summed in analogue sum units in groups of 4 or 6 and sent to the discriminators.

3.4.1 Pulse Shape Discriminator

The PSD circuit employed here is designed for the GSO/CsI(*Tl*) well type phoswich counter [37]. Since signals originated from GSO have faster decay time than those from CsI(*Tl*) , the measurement of the interval between the first and the second zero crossover point of the triple-polar pulse allows us to pick up only events that photon deposits its energy purely in GSO (GSO event).

Time to Amplitude Converter (TAC) is equipped to monitor the operation of the PSD during the flight by measuring the time interval. The TAC monitors 16 counters out of 64 because of the limitation of the space and the electric power. Figure 3.6 shows the 2-dim distribution for the TAC value and the ADC value produced by calibration sources (122 keV line from ^{57}Co and 511 keV line from ^{22}Na). In the figure, the band on the left side corresponds to GSO events and the band on the right

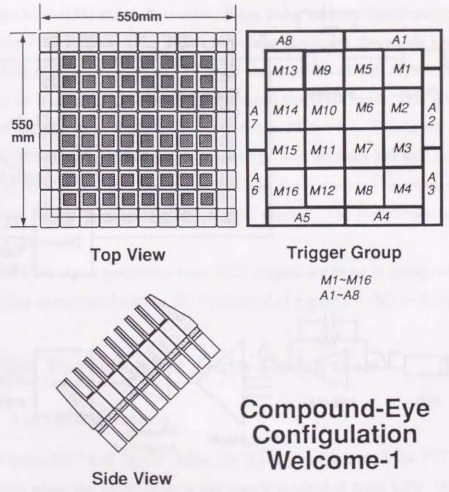

Figure 3.4: Welcome-1 Detector

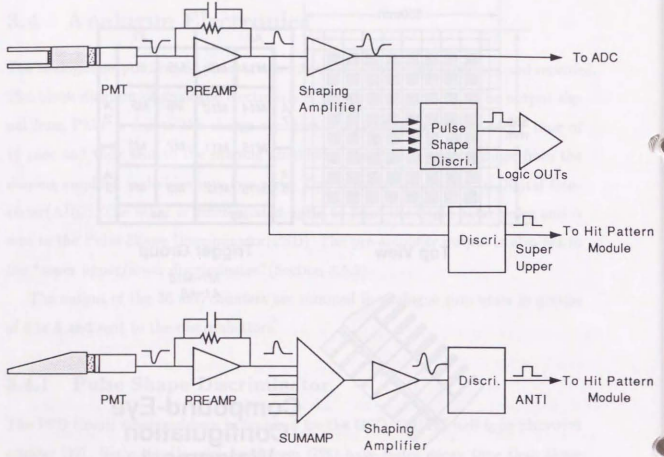

Figure 3.5: Analogue Electronics

is due to the events in which photons deposit some or all energy in CsI(Tl) shield crystal. In the PSD, a timing window which we refer to as "PSD window" adjusted to select GSO event as shown in Figure 3.7. Only when the input signal enter the window, the PSD issues trigger signal.

When the number of photo-electrons becomes low ($n_e \leq 50 or E \leq 50 keV$), the pulse shape of CsI(Tl) pulses fluctuates. If the pulse narrows significantly, it passes through the PSD window. This seems to set the minimum detectable energy limit of the well-type phoswich counter. To avoid the intrusion of CsI(Tl) event the PSD window is set narrower than that is fully covered the GSO band. This gives rise to the loss of the detection efficiency as indicated in Figure 3.7. The figure shows the TAC distribution of No.35 counter in the energy interval from 330 keV to 600 keV. The histogram is fitted by a Gauss function and the inefficiency is estimated as the fraction that extends beyond the limit of PSD window. The inefficiency amounts to 3% in this case.

To reduce the signal processing load, PSD triggers are or-ed in groups of 4. There are 16 trigger groups as shown in the right panel of Figure 3.4 (M1 $\sim$ M16).

3.5 Hit Patterns for Data Reduction

3.5.1 Anti Hit Pattern

The PSD generates "Anti Signal" when the input signal is out of the PSD window. This happen when the input pulse is not purely originated from GSO. When some counter issues the PSD trigger, the Anti Signal of all counters and the discriminator output from surrounding CsI(Tl) anti counters are latched by the hit pattern module. This "anti hit pattern" consists of 16 bits from PSDs plus 8 bits from surrounding counters. (Figure 3.8).

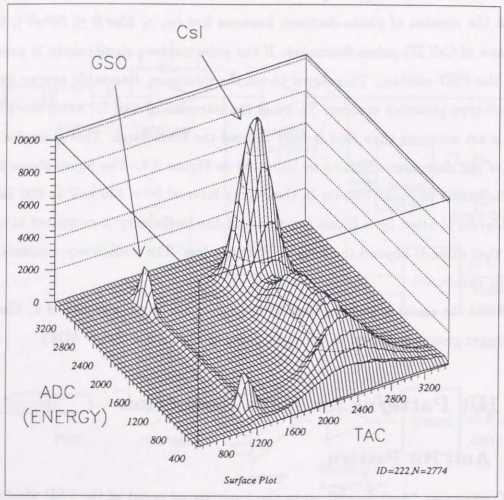

Figure 3.6: Two-dim distribution of ADC's and TAC's obtained by Welcome-1 when it is irradiated by ^{57}Co and ^{22}Na. The band of the left corresponds to GSO events and the band on the right to CsI(Tl) events.

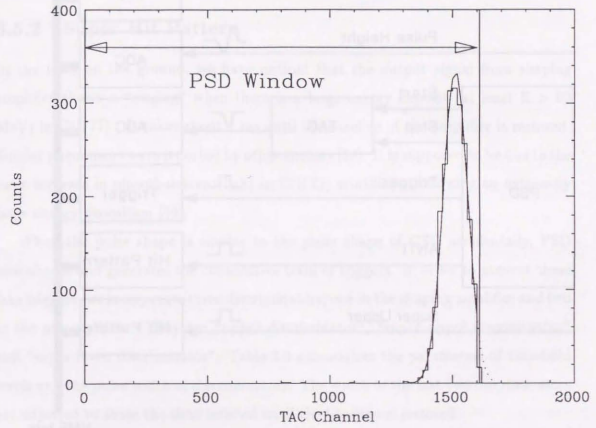

Figure 3.7: The PSD window

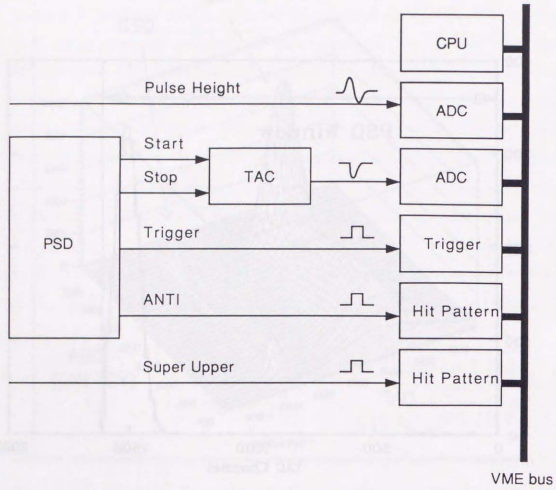

Figure 3.8: Digital Electronics

	Threshold	Width
Upper Discriminator	800 keV	300μs
Super Upper Discriminator	$\sim$ 20 MeV	420μs
Super Lower Discriminator	$\sim$ 200 MeV	730μs

Table 3.3: Threshold level and pulse width of discriminators

3.5.2 Super Hit Pattern

In the tests on the ground, we have noticed that the output signal from shaping amplifier shows a "ringing" when there is a large energy deposit (at least E > 60 MeV) in CsI(*Tl*) . It takes about 1 ms until the baseline of the amplifier is restored. Similar phenomena were reported by other authors [38]. It is supposed to be due to the large increase in phosphorescent light in CsI(*Tl*) scintillator following an extremely large energy deposition [39].

When the pulse shape is similar to the pulse shape of GSO accidentally, PSD misbehaves and generates the consecutive train of triggers. In order to prevent these fake triggers, we incorporate three discriminators; one in the shaping amplifier and two in the preamplifiers. They are "upper discriminator", "super upper discriminator" and "super lower discriminator". Table 3.3 summarizes the parameters of threshold levels and the pulse width of discriminators. The width of the last two discriminators are adjusted to sense the time interval until the baseline is restored.

Among them only the upper discriminator serves the veto signal for the PSD trigger for 300μ sec. The threshold level was set at 800 keV. The super upper and lower discriminator generates the pulse of 420 μsec width and 730 μsec respectively (Figure 3.9). Both pulses are or-ed and latched as "super hit pattern" (16bit) in the same manner as the anti hit pattern.

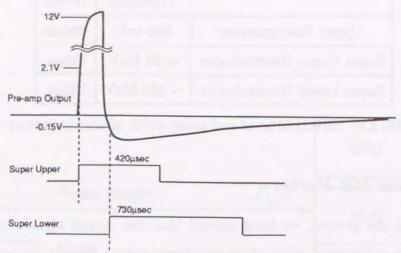

Figure 3.9: Pre-amplifier output and super upper and lower discriminator

3.6 Data Acquisition System

When a trigger signal is generated from one counter, the pulse height in the particular group of four and the hit pattern are recorded along with the time of the event. All the system is controlled by a 32-bit microprocessor through VME (Versa Module Europe) bus. The microprocessor is MC68000 CMOS CPU operated at 10MHz. Data processing is carried out by a set of interrelated processes and interrupt routines executing under control of the real time operating system, OS9/68000 [40]. The software including operating system are stored in the EPROM. The 512kB RAM provides data buffer in which data is reformatted for the transmission and recording. One event data consists of 34 bytes and the Welcome-1 detector typically generates triggers about 350 Hz at the ceiling.

The scaler are used to measure the count rate to monitor the detector status. The measured signals include the "Anit Signal" from PSD, "Upper Signal" from the upper discriminator and "Super Signal" from the super upper/lower discriminator. Among them the Upper Signal are dedicated to measuring the live-time together with the

"dead time monitoring system" described in

3.7 Pointing System

The pointing is done by the azimuth control and the elevation control system. On the top of the gondola, a torque motor is attached. The whole detector is suspended by the straps through the motor axis. Azimuth pointing and rotation are achieved by "Yorimodoshi" method [41]. A magnetometer on the gondola and torque motor form the stabilization system. The elevation angle is controlled by a ball screw drive located on the gondola.

The orientation of the pointing is monitored by two independent systems. One is the combination of a magnetometer for azimuth and slope gauge for elevation. The other is Star/Solar imaging system. During the night, a MCP (micro channel plate) coupled to a CCD camera images the sky. Its field of view is 9.1×6.3 degrees and identifies stars of magnitude ~ 8.1. The star image on the CCD camera (512×512 pixels) is digitized by the image processing board on the VME bus. The microprocessor selects the bright points to the ground through the telemetry. On the ground station the star image is reconstructed every 2 seconds by using a workstation. After the dawn the star camera was switched to the solar one with wide field lens (60×60 degrees). Using the same readout system as star camera, the position of sun can be known within the accuracy of 0.5 degrees.

3.8 Response to Hard X-rays/Gamma-rays

In order to study a incident spectra from celestial objects, the detector response to incident photons are to be considered.

3.8.1 Full Peak Efficiency of GSO crystal

We measure the "full peak efficiency" of 1cm GSO used in the well-type phoswich counter. The full peak efficiency is defined as a ratio of the number of photons that deposite their full energy to GSO over the number of incident photons. In Figure 3.10, the efficiency measured with the calibration sources is compared with the calculation by using the Monte Calro code, EGS4 [42]. In EGS4, photoelectric absorption, Rayleigh scattering, Compton scattering and pair production are included down to 1 keV for photons and 10 keV for electrons.

The three lines in the figure correspond to the cases of three different thicknesses of GSO used in the calculation. The contribution from the uncertainty in the GSO thickness is considered to give the largest error in estimating the efficiency, and thus, from these lines, the systematic uncertainty in the calculation is estimated to be less than 3%.

3.8.2 Compton Rejection in the Well-type Phoswich Counter

In the Compton scattering, incident photon sometimes deposits its fraction of energy to the detection part and escape. The Compton scattered events contaminate the spectrum if scattered photons are not detected in the shield.

In the well-type phoswich counter, the contamination is reduced significantly compared with the conventional detector. Figure 3.11 shows the measured energy spectra of GSO with and without well irradiated by ^{22}Na. This figure indicates that active well provides excellent Compton rejecton.

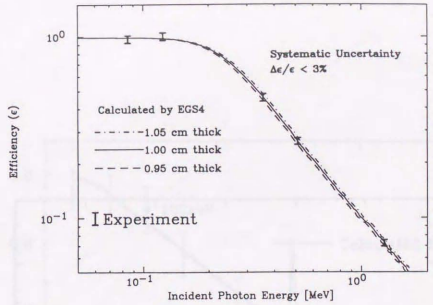

Figure 3.10: The full peak efficicency of GSO. The data with error bar is the result of the experiment. The lines are calculated efficiencies using EGS4. The three lines are from differece in thickness of GSO. From these lines, the systematic uncertainty in the calculation is estimated to be less than 3%.

3.8.3 Angular Acceptance of the detector

Energy dependence of the angular acceptance (detector field of view) was measured using the calibration sources ^{57}Co (122 keV) and ^{22}Na. Figure 3.12 is the results of the experiments and the comparison with the Monte Carlo calculation. By fitting the data, the angular acceptance (HWHM) is calculated to be 7.7±0.1° at 122 keV and 9.1±0.2° at 511 keV and consisted with the calculation.

3.8.4 Response of the Welcome-1 detector

The instrument response is calculated by using the program based on EGS4. In the calculation, the telescope is irradiated by the plane wave incident photons. The measured energy resolution and anti rejection are included. Figure 3.13 shows the simulated spectrum and the incident spectrum used in the simulation.

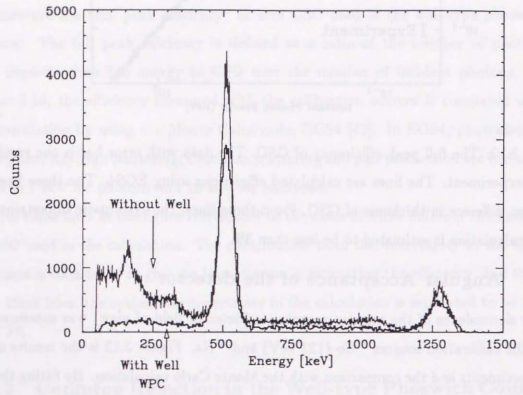

Figure 3.11: The measured energy spectrum of GSO irradiated by ^{22}Na. The spectrum of without/with CsI(*Tl*) well are compared. Both are normalized by the area of 511 keV peak. The energy resolution deteriorate from 10% to 12% at 511 keV when GSO is put in the CsI(*Tl*) well due to the attenuation of scintillation light from GSO.

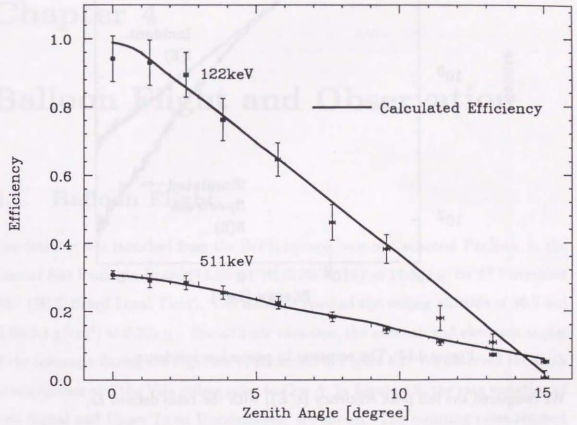

Figure 3.12: The Angular acceptance of the telescope.

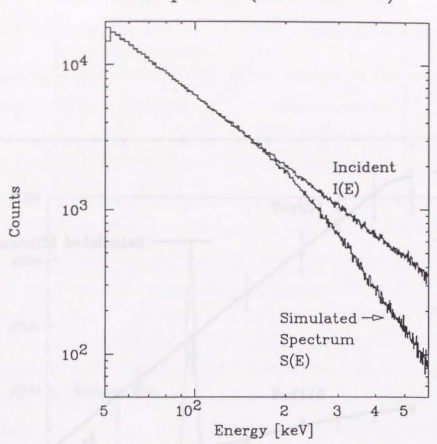

Figure 3.13: The response to power law incidence .

We compared the full peak efficiency ($\varepsilon(E)$) with the ratio defined as,

$$f(E) = \frac{S(E)}{I(E)}. \tag{3.2}$$

where $I(E)$ and $S(E)$ is the incident spectrum used in the calculation and the simulated spectrum. The result was $\varepsilon(E) \approx f(E)$. This means that the contamination due to the Comton scattered events can be neglected in Welcome-1 detector.

Chapter 4

Balloon Flight and Observation

4.1 Balloon Flight

The detector was launched from the INPE balloon base in Cachoeira Paulista, in the state of São Paulo, in Brazil ($45.00'.34''W, 22.39'.44''S$) at $11{:}50_{\text{P.M.}}$ on 18 November 1991 (BLT:Brazil Local Time). The detector reached the ceiling altitude of 36.7 km (4.6 ± 0.1 g/cm^2) at $2{:}30_{\text{A.M.}}$. The altitude variation, the azimuth and elevation angles of the telescope during the flight are summarized in Figure 4.1. We observed the Crab nebula/pulsar and the Vela pulsar prior to Cen A. In Figure 4.2, the rate variation of Anti Signal and Upper Level Discriminator are shown. The counting rates reached maximum at an altitude of around 100g/cm^2, Pfotzer Maximum.

Throughout the observations, all counters operated normally. Figure 4.3 shows the variation of the temperature of well-type phoswich counters. The temperature decreased as time went by, and reached an almost equilibrium by the time of the observation of Cen A.

4.2 Cen A Observation

The observation of Cen A started at $7{:}40_{\text{A.M.}}$, November 19, 1991 (BLT). In total 9 cycles of ON and OFF-source observations (~10 minutes each) were performed until $11{:}00_{\text{A.M.}}$ (BLT). In the ON-source observation, we followed Cen A by redirecting the

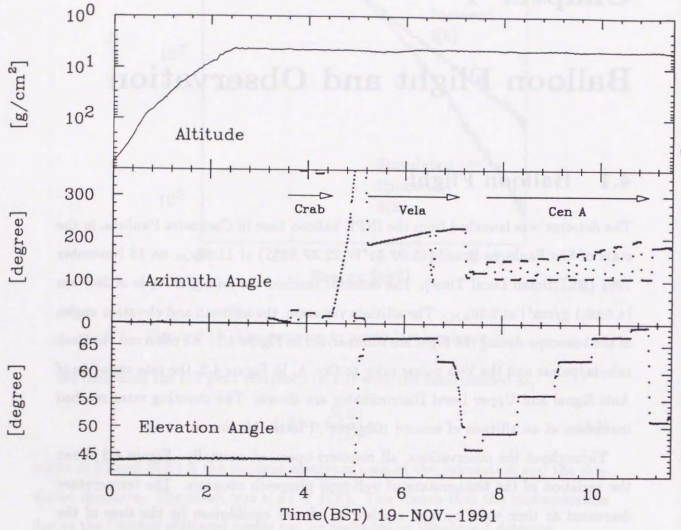

Figure 4.1: Altitude, azimuth angle and elevation angle of the telescope during the flight.

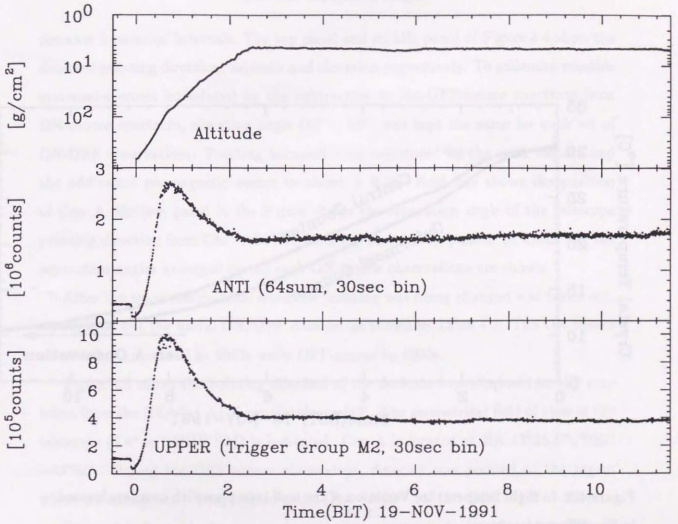

Figure 4.2: Altitude, ANTI, clocked UPPER

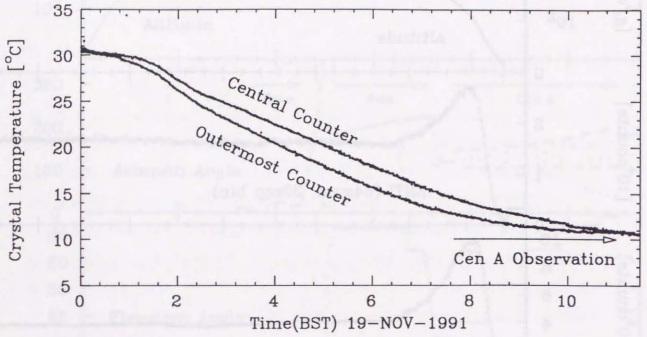

Figure 4.3: In flight temperature Variation of the well type phoswich counters located in the different position.

ON	1	2	3	4	5	6	7	8	9
Separation[deg.]	2.53	2.12	2.26	2.44	2.04	2.08	1.12	1.73	0.80
Direction[deg.]	227.8	130.8	238.9	131.4	213.8	132.7	212.6	136.3	172.9

Table 4.1: Separation Angle

detector 5 minutes' intervals. The top panel and middle panel of Figure 4.4 show the detector pointing direction, azimuth and elevation respectively. To minimize possible systematic errors introduced by the subtraction of the OFF-source spectrum from ON-source spectrum, elevation angle ($40° - 68°$) was kept the same for each set of ON-OFF observations. Pointing accuracy were monitored by the solar camera and the additional geomagnetic sensor to about $\pm$ 0.2°. Bold line shows the position of Cen A. Bottom panel in the Figure shows the separation angle of the telescope pointing direction from Cen A derived from top and middle panels. In Table 4.1, the separation angles averaged during each ON source observations are shown.

After the transmission time when the pointing was being changed was taken out, we selected out the useful ON/OFF data set as shown in Table 4.2. The ON-source observation amounted to 5040s while OFF-source to 4800s.

Figure 4.5 shows the pointing direction of the detector superimposed on sky map taken from the HEAO-1 A1 X-ray Catalogue [43]. The geometrical field of view of the telescope ($7.4° \times 7.4°$HWHM) is indicated. Cen A is located at RA $13^h25.5^m$, DEC $-43°01'$. During the OFF-source observation, detector was pointed to the region where no strong hard X-ray source exists (RA 13^h28^m-15^h12^m DEC $-14°$- $-19°$).

Figure 4.6 shows the background energy loss spectrum during the observation of Cen A.

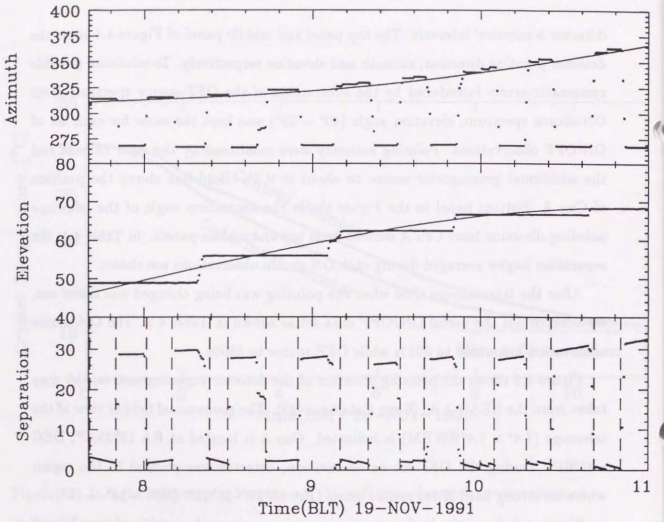

Figure 4.4: Cen A Observation

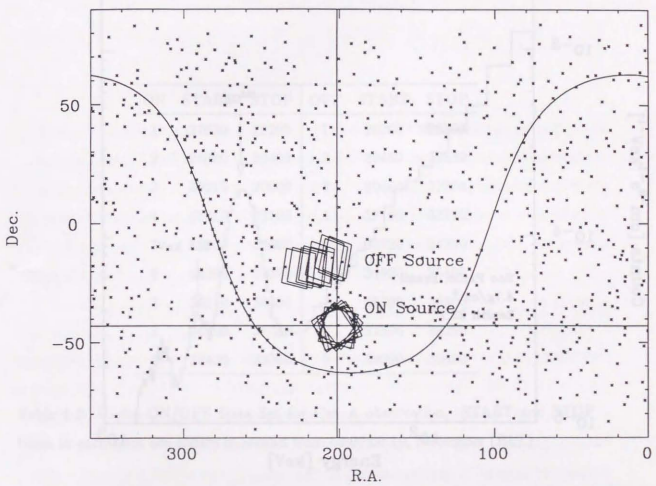

Figure 4.5: Telescope Pointing Direction. The geometrical field of view of the telescope is indicated.

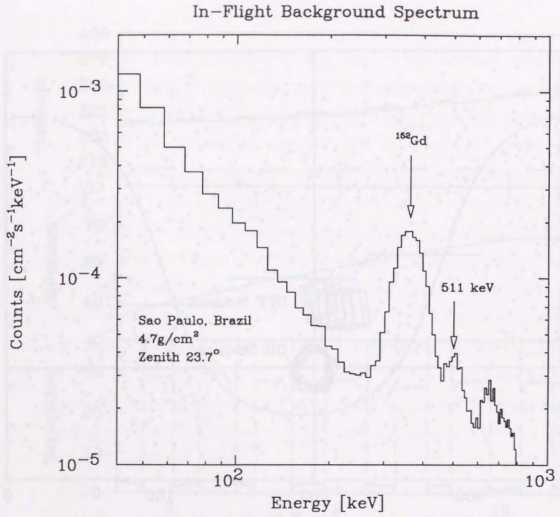

Figure 4.6: The background energy loss spectrum during the flight of the Welcome-1 instrument in November of 1991. The spectrum was taken at 4.7g/cm^2 of atmospheric depth with the detector pointed 23.7° from the zenith.

ON	START	STOP	OFF	START	STOP
1	27630	28200	1	28260	28800
2	28860	29400	2	29460	29880
3	30210	30600	3	30660	31260
4	31410	32100	4	32160	32730
5	33000	33600	5	33720	34230
6	34290	34800	6	34920	35400
7	35640	36300	7	36390	36900
8	36990	37500	8	37590	38250
9	38430	39000	9	39090	39600

Table 4.2: Useful ON/OFF Data Set for Cen A observation. START and STOP times in each term are shown in second from 00:00:00 19, November (BLT)

Chapter 5

Background of the Detector

Background is a major concern in the hard X-ray/gamma-ray astronomy. The background counting rate is normally an order of magnitude higher than the source counting rate in this energy range (a few 10 keV $\sim$ a few MeV). It is important to understand the sources of background because time variation of some unknown background sources can introduce a systematic error when we extract the signal by subtraction.

5.1 Background in Balloon Experiments

Low energy gamma-ray background at balloon altitude have been measured by several authors[44, 45, 33]. Background radiation is originated in the atmosphere or is the primary cosmic gamma-rays. Photons of cosmic origin are interesting object in itself, but also become background against point source observations. They may enter the instrument through its aperture, penetrate its shield or be generated in the instrument materials by atmospheric neutrons and protons.

5.1.1 Atmospheric and Cosmic Gamma-rays

Atmospheric gamma-rays are produced predominantly bremsstrahlung from electrons in the electro magnetic shower initiated by the primary cosmic nuclear particles.

Ling [44] studied the background spectrum from 300 keV up to 10 MeV in detail using the semiempirical model. He compared it with the result of balloon experiments

over Palestine, Texas. According to the study, the spectrum of the downward flux, atmospheric and cosmic photons, can be approximated by single power law in this energy range. Ling also derived the angular distribution. His calculation shows that the flux from lower hemi sphere is $2 \sim 3$ times as large as from upper hemi sphere below 500 keV.

Kinzer *et al.* [33] measured the downward flux between 20 keV to 200 keV at $5 g/cm^2$ over Palestine. The result is represented by the power law of $10.4 \times 10^{-2} E^{-1.75}$[photons/$cm^2$/s and agrees reasonably well with the index of Ling's result($\alpha = 1.9$).

5.1.2 Induced Radioactivity

Induced radioactivity due to nuclei produced in interactions of cosmic ray particles may be a serious problem. Dyer and Morfill [46] have calculated the radioactivity produced in a CsI(*Tl*) crystal exposed to the primary cosmic radiation and to the particles in the radiation belts. They concluded that the most copiously produced radioactive species is the neutron-deficient isotopes of iodine and cesium. Another radioactive nuclide is produced by the absorption of slow neutrons by ^{128}I to form ^{129}I. The net result of the subsequent decays of these radioactive nuclide is a continuum spectrum with a strong peak at $\sim$ 200keV due to the decay of ^{123}I by electron capture. Gehrels [47] reported the same line feature observed at balloon altitude with Ge detector surrounded by NaI scintillator.

The background spectrum obtained in our balloon experiment in Brazil shows no line features around 200 keV (Figure 4.6). As described in Section 3.3.1, the detection part of the well-type phoswich counters is shielded almost in 4π sr by active collimator/shield. Gamma-rays from $\beta - \gamma$ decays of unstable isotopes produced by the activation are all to be detect efficiently by the shield.

Small difference between the spectra taken in the flight and on the ground suggests that the induced radioactivity of GSO crystal is not a large source of the background for the balloon experiment.

5.2 Monte Carlo Calculation

We performed Monte Carlo calculations to study the detector performance for gamma-rays using EGS4 photon/electron transport code [42]. In EGS4, photoelectric absorption, Rayleigh scattering, Compton scattering and pair production are included down to 1 keV for photons and 10 keV for electrons.

In the simulation, the 64 well type phoswich counters and 36 CsI(*Tl*) anti counters are placed inside a sphere. We assume photons are emitted inwards with the photon index of 1.7. Its surface position and emission direction are chosen to be isotropic.

The photon energy deposit on each of 64 GSOs are recorded for each photon. If CsI(*Tl*) receives an energy deposit that exceeds the measured threshold(40 keV), the event is rejected.

The results of the calculation are shown in Figure 5.1. Dashed line (denoted as WPC) shows the background spectrum where each counter acts independently. The bump around 500 keV is due to the positron annihilation occurred in the detector material and one 511 keV photon hits GSO while the other escapes from the counter. Thick-solid line (denoted as AHP) in Figure 5.1 is the background spectrum when hits in the surrounding counters registered in the anti hit pattern are used to veto the background events. The bump due to positron annihilation is suppressed by the anti hit pattern. Two thin-solid lines show its breakdown, the flux entering through aperture and shield leakage respectively. It is evident that the flux from the aperture is a dominant component below 250 keV .

5.3 Comparison with the Observation

The results of the calculation are compared with the observed background spectrum in Figure 5.2. Data points with error bar are the observed background spectrum taken at an altitude of 4g/cm^2. The dash-dot histogram shows the internal background. This was obtained when a well-type phoswich counter with PMT was placed in an enclosure of 5cm Cu and 5cm Pb. The dashed line is the result of Monte Carlo

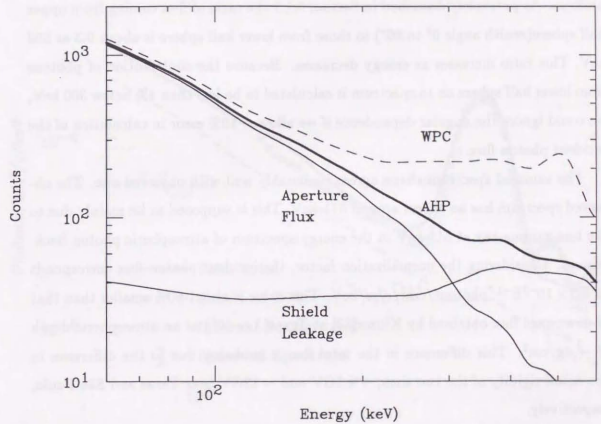

Figure 5.1: The calculated continuum background spectrum and its breakdown. Dashed line shows the background spectrum where each counter acts independently. Thick-solid line (denoted as AHP) represents the background spectrum when hits in the surrounding counters registered in the Anti Hit Pattern. Two thin-solid line show the breakdown of AHP, the flux entering through aperture and shield leakage respectively.

calculation corresponding to the thick solid line in Figure 5.1. The solid line is the sum of the dashed line and the dash-dot line. The overall normalization factor is adjusted so that the intensity of observed and calculated spectrum agrees.

Angular distribution of incident background photon direction is assumed to be uniform. As previously described in Section 5.1.1 the ratio of flux coming from upper half sphere(zenith angle 0° to 90°) to those from lower half sphere is about 0.3 at 500 keV. This ratio increases as energy decreases. Because the contribution of photons from lower half sphere on to spectrum is calculated to be less than 4% below 300 keV, we could ignore the angular dependence if we allow $\sim$ 10% error in calculation of the incident photon flux.

The summed spectrum shape agrees reasonably well with observed one. The observed spectrum has an excess around 511 keV. This is supposed to be mainly due to the line gamma-ray at 511 keV in the energy spectrum of atmospheric photon background. Considering the normalization factor, the incident photon flux corresponds to $3.5 \times 10^{-3} E^{-1.7}$ photons/cm^2/s/sr/keV. This value is about 60% smaller than that of downward flux obtained by Kinzer[33] at Texas($\lambda \sim 40°$) at an atmospheric depth of $\sim$ 4g/cm^2. This difference in the total flux is probably due to the difference in the cutoff rigidity of the two sites, $\sim$ 4.5GV and $\sim$ 12GV over Texas and São Paulo, respectively.

The detector background is broken down to the background from aperture and internal background in the lower energies. In the higher energies above 250 keV, the internal background and the shield leakage dominate. Our simulation and the observed spectrum by Welcome-1 shows that anti-coincidence based on the well-type configuration works properly to reduce the background.

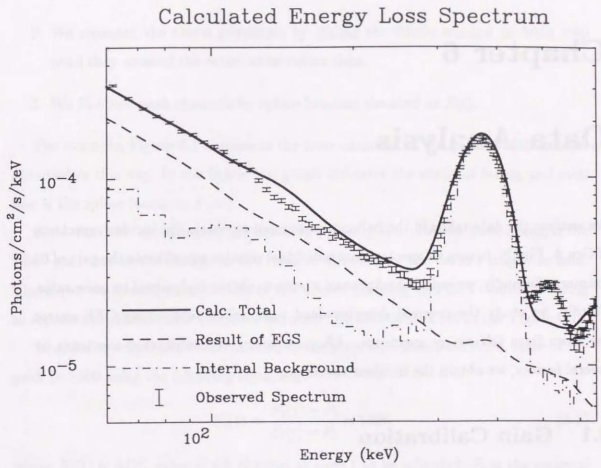

Figure 5.2: The calculated continuum background and observed background in Welcome-1 detector. The dash-dot histogram is internal background measured in the cave of Pb(5cm)+Cu(5cm) on the ground. The dashed line represents the result of Monte Carlo simulation. Calc.Total(the solid line) is the sum of the dashed line and the dash-dot line. The data points with error bar show observed background spectrum taken at an altitude of 4g/cm^2.

Chapter 6

Data Analysis

We analyze the data taken in the balloon experiment to obtain the incident spectrum of Cen A. Firstly, to sum 64 spectra from individual counter we calibrate the gain of 64 counters. Secondly, we reduce background events to obtain high signal to noise ratio. Thirdly, we study the precised detector dead time before subtracting OFF source spectrum from ON source spectrum. After correcting the subtracted spectrum by several factors, we obtain the incident spectrum.

6.1 Gain Calibration

The accurate gain calibration is required to sum all counters spectra. The gain was calibrated for every counter by using the peak position of α-decay of ^{152}Gd in GSO.

Time variation of the gain is supposed to be caused by two distinct reason. First, the light yield of GSO increases as the temperature goes down (-0.5%/degree). Second, the earth's magnetic field vector at the telescope influences on the gain of the PMT. This occurred because the electrostatic focussing of the photoelectrons to the first dynode in the PMT is affected by weak magnetic field.

Since the α-decay rate is very low (0.17$\pm$0.003Hz), in order to follow the time variation of the gain we need integrate the data over a time interval longer than typical observation time scale of 10 min. We introduce the "sliding window method" as described below by assuming the variation took place smoothly.

1. To know a peak channel at a certain time we accumulated the data of 60 min duration where that time was located in the center. Then we calculated the peak channel by computer fitting.

2. We repeated the above procedure by sliding the 60min window in 5min step until they covered the entire observation time.

3. We fit these peak channels by spline function denoted as $S(t)$.

For example, Figure 6.1 represents the time variation of the gain of 25th counter obtained in this way. In the figure, bar graph indicates the result of fitting and solid line is the spline function, $S_{25}(t)$.

Note that the switching of the detector pointing is known to have changed the PMT gain due to the change in the relative direction of the earth's magnetic field. Therefore, we treated the intervals of ON source pointing and OFF source pointing as separate data sets. The difference between ON and OFF is 5% in the Figure 6.1.

In order to adjust the time variation of the gain, we normalized ADC value of the peak to 1500 using the following equation,

$$N_i'(t) = \frac{N_i(t) - P_i}{S_i(t) - P_i} \times 1500 \tag{6.1}$$

where $N_i(t)$ is ADC value of ith channel at time t to be adjusted, P_i is the pedestal value of ADC.

The calibration procedure is verified in Figure 6.2; the α peak comes out constant of time and uniform over all 64 counters. The ADC value of the peak in the summed spectrum over the 64 counters is stable within 0.28%(RMS).

6.2 Data Reduction

The data reduction is the most important part of the analysis. Welcome-1 features low background partly because the data reduction reduces events associated with Compton scattering or charged particles.

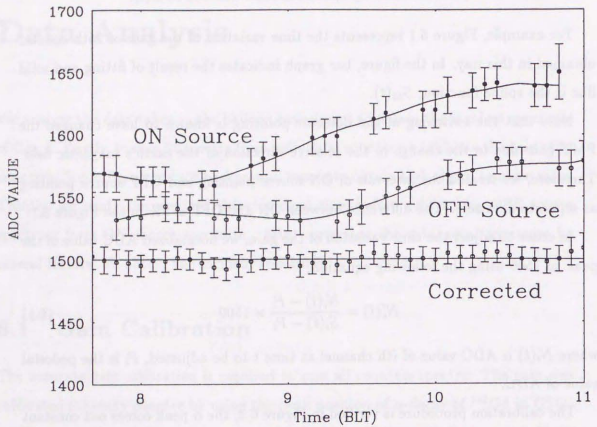

Figure 6.1: Time variation of the overall gain of the No.25 counter.

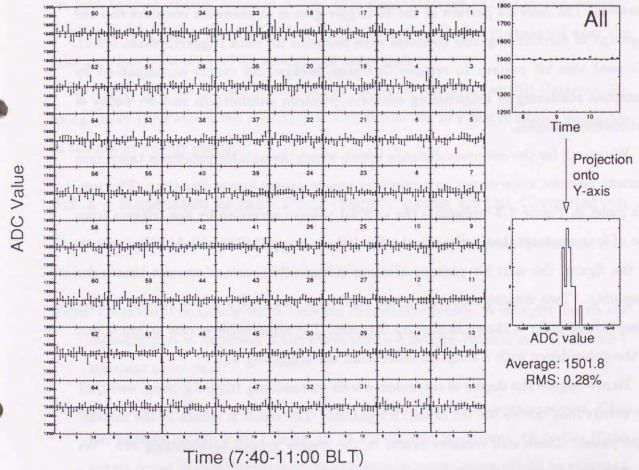

Figure 6.2: Time variation of peak channel after gain calibration.

The data reduction is divided into two steps; use of the hit patterns and rejection of fake PSD trigger using event correlation. In this section, these steps are explained in detail and its effficiencies is also summarized.

6.2.1 Use of the Hit Patterns

In the compound-eye configuration each counter is surrounded by eight neighboring counters. The Anti hit pattern of the 16 trigger groups of phoswich counters and the 8 groups of surrounding anti counters were recorded for each trigger(Section 3.5.1). We used this hit pattern to remove Compton background events accompanied by Compton scattering in neighboring counters, positron annihilation and $\beta\gamma$ decay of radioactive isotopes.

We search for the optimum distance within which the anti hit pattern is taken into account because unnecessary anti rejection merely causes loss of live time. The top-left panel in Figure 6.3 represents the anti hit pattern recorded by the triggers from one of four counters that belong to the 6th trigger group (M6 denoted in Figure 3.4). In the figure, the anti hit pattern of surrounding anti counters are not shown for simplicity. Two dimensional histogram represents the real position of the trigger group whose order is shown in the top diagram. The remarkable excess at M6 is due to the coincidence with 3 counters other than the triggering unit.

To investigate the degree of coincidence with surrounding trigger groups, we reject the events that carries M6 bit of anti hit pattern. The result is shown in the middle-right panel. There still remains excess in the trigger groups surrounding M6. We rejected the events with anti hit pattern bit of triggering group itself or those of the surrounding groups. After removing these events no correlation is shown, which means that further extension of the anti coincident region was not required.

The super hit pattern is introduced to reduce the fake PSD trigger. The analysis described above is performed for super hit pattern. Bottom-left panel of the Figure 6.3 shows the super hit pattern for M6 events and bottom-right shows the events remaining after the events that carry the M6 bit of the super hit pattern is subtracted. No excess can be seen in this plot. This is a reasonable result considering that high

energy charged particles/photons deposit energy on several counters. Therefore, they are rejected efficiently by using the super hit pattern bit of the same trigger group.

In order to evaluate the effectiveness of the reduction using the hit pattern, the background spectrum summed over all counters is integrated as shown in Figure 6.4. The dashed line is the background spectrum summed over all counters and the thin solid line is the spectrum passed through the reduction. Significant reduction can be seen over all energy range at a cost of a small increase ($\leq$5%) in the detector deadtime. The bump around 500 keV due to pair annihilation in material near the telescope has been reduced by an order of magnitude.

In Figure 6.4, the dotted line shows the combined result of two Hit Patterns. By using Super Hit Pattern the reduction is 30% below 100 keV but is almost negligible in the higher energy region.

6.2.2 Rejection of fake PSD trigger using Event Correlation

To examine whether fake PSD triggers are fully removed by the use of the hit patterns, we introduced "Event Correlation" that we denoted as,

Time Interval The time interval between consecutive events. A straight line on the semi-log plot is expected if the event obeys a simple Poisson statistics with a constant event rate.

Channel Correlation Subtraction between unit number of consecutive events. Channel number ranges from 1 to 64, so its subtraction does from -64 to 64. If the events occur in completely random sequence, triangle shape would be expected on the plot whose apexes are located on (-64, 0), (64, 0), (0, y) where y is a point on the vertical axis.

Figure 6.5 shows the event correlations while we observed the background region; the left panels are Channel Correlation, and right are Time Interval. The top two panels are for all recorded events, when the middle two panels are after the reduction using the hit pattern. There still remains excess from the expected distributions, which suggest there are non-random fake events.

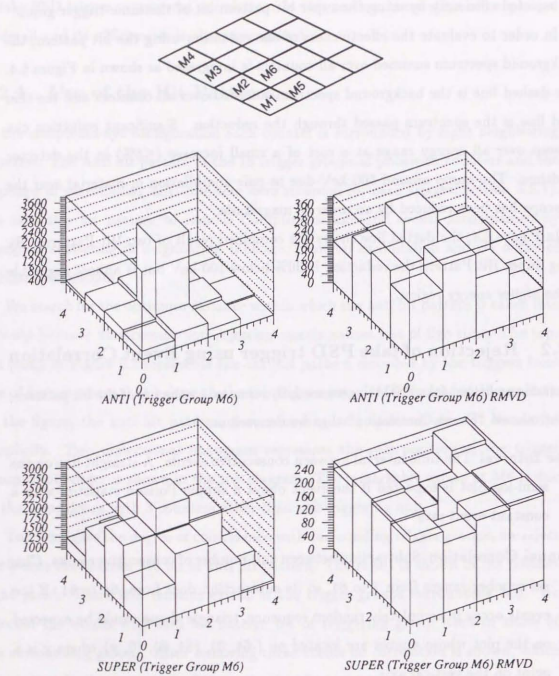

Figure 6.3: Data reduction using the anti hit pattern and the super hit pattern

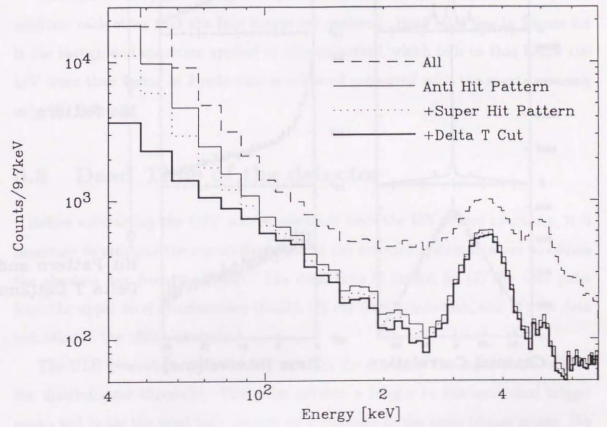

Figure 6.4: Effects of the data reduction.

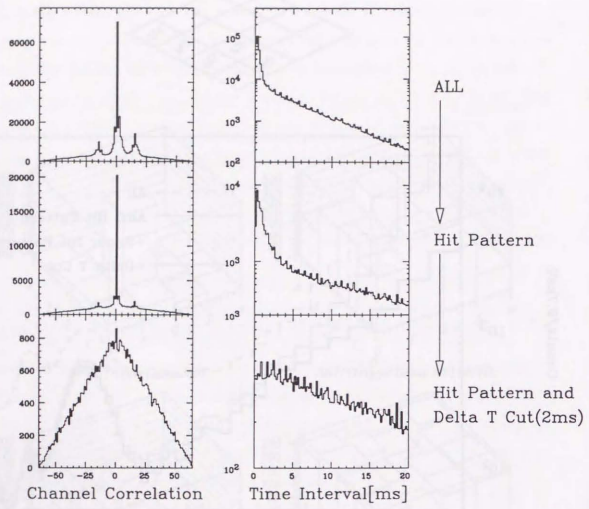

Figure 6.5: Left:Channel Correlation. Subtraction between counters id number of consecutive events. Unit number ranges from 1 to 64, so its subtraction does from -64 to 64. If the events occur in completely random sequence, triangle shape would be expected on the plot whose apexes are located on (-64, 0), (64, 0), (0, y) where y is a point on the vertical axis. Due to the order of numbering, $\mid x \mid \simeq 16$ corresponds to neighbors. Right: Time interval between consecutive events. A straight line on the semi-log plot is expected if the event obeys a simple Poisson statistics with a constant event rate.

It is evident that we had not removed all the fake events after rejecting background events using the hit patterns. We introduced another reduction to reduce the fake events. The reduction criteria are as follows,

> Events that follow or proceed an event that occurs in the neighboring units within a certain time interval (Δt) should be removed.

The bottom two panels in Figure 6.5 show the result for Δt =2ms. The two panels confirms each other that the fake events are removed. Bold solid line in Figure 6.4 is the background spectrum applied by this reduction, which tells us that below 100 keV more than factor of 2 reduction is achieved compared with the spectrum using only Hit Patterns.

6.3 Dead Time of the detector

. Before subtracting the OFF source spectrum from the ON source spectrum, it is necessary to estimate the overall dead time of the detector system in order to obtain the absolute flux from the object. The dead time is caused by (1) the veto pulse from the upper level discriminator (ULD), (2) the data acquisition, and (3) the data reduction in the offline analysis.

The ULD generates a pulse for 300 μs when the energy of the input pulse exceeds the discriminator threshold. The pulse inhibits a trigger to the individual trigger group and cause the dead time against all 4 counters in the same trigger group. We directly measured the duration of the pulse by using the clock pulse (125 Hz). The dead time due to the veto pulse from the ULD is calcuulated as,

$$\text{dead time ratio} = M[Hz] \times 8 \times 10^{-6}, \tag{6.2}$$

where M and 8μsec are the count rate of the clock pulse and its width, respectively. The live time ratio (1–the dead time ratio) due to the pulse from the ULD is presented in the upper panel of Figure 6.7. They are calculated for each observation time interval.

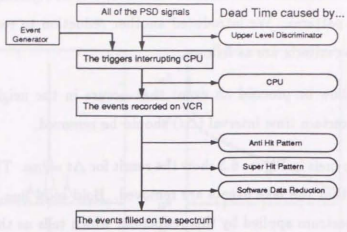

Figure 6.6: The origins of the dead time and the pseudo-event generator.

In order to estimate the the dead time caused by the data acquisition system and the successive data reduciton, we adopted a test pulse module in the data acquisition system. The module is called as "pseud-event generator". The pseud-event generator generates a pseud trigger pulse (3.815Hz). The events are processed in the same manner as for the normal triggers in the data acquisition system.

In the data reduction, the dead time is caused by (a) the anti hit pattern (b) the super hit pattern and (c) Delta t cut. These selections in the offline analysis are applied to the pseud-triggered events. To calculate the dead time for each well-type phoswich unit, we regard pseud-triggered event as a certain unit. Since the pseud-event sampled the anti hit pattern and the super hit pattern randomly, the accidental dead time is calculated by counting the pseudo-events; we can obtain the dead time by a following formula:

$$deadtimeratio = (1 - \frac{n}{N}) \pm \sqrt{\frac{n(N-n)}{N^3}}. \tag{6.3}$$

Here N is the total number of pseudo-events generator and n is the number of events generated and accepted by the data reduction. The live time which can be calculated using pseudo-event generator is shown in the lower panel of Figure 6.7. The total live time ratio is the product of these two components in the figure.

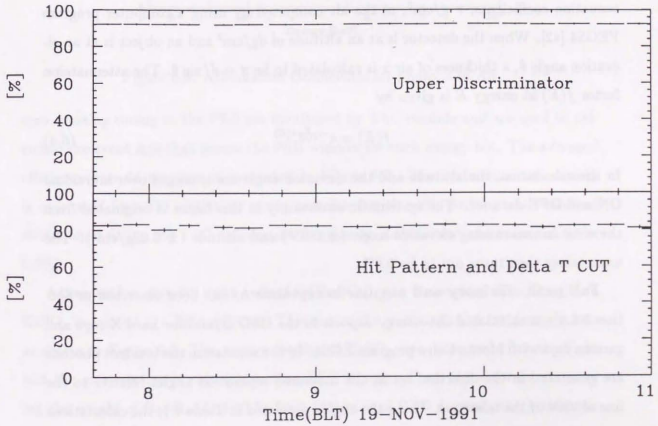

Figure 6.7: Live time ratio

6.4 Factors Affecting the Detection Efficiency

Hard X-ray and gamma-rays from a celestial objects are attenuated through the atomosphere and materials in front of the detector. Photons may not deposit its full energy in the detection part. Angluar acceptance (F.O.V) depends on the energy of incident photons and the incident direction relative to the telescope. We must correct these factors to derive the incident spectrum from the raw count spectrum.

Atomospheric attenuation of hard X-rays/gamma-rays. Hard X-ray and Gamma-rays are attenuated by interacting with air. Figure 6.8 shows the mass attenuation coefficients, τ g/cm^2, of the air computed by using a computer program PEGS4 [42]. When the detector is at an altitude of dg/cm^2 and an object is at an elevation angle θ, a thickness of air x is calculated to be $x = d/\sin\theta$. The attenuateion factor $f(E)$ at energy E is given by

$$f(E) = e^{-\frac{d}{\sin\theta}\tau(E)} \tag{6.4}$$

In the calculation, the altitude and the elevation angle are averaged over individual ON and OFF data set. The systematic uncertainty in this factor is originated from the error in measureing elevation angle ($\pm$ 0.05°) and altitude ($\pm$ 0.02g/cm^2). The uncertainty then turns out to be 0.6%.

Full peak efficiency and angular acceptance As has been described in Section 3.8.4, we calculated the energy deposit in the GSO crystal for hard X-rays and gamma rays with Monte Calro program EGS4. In the simulation the incident photons are generated in the direction set at the measured separation angles relative to the line of view of the telescope. Using the angles presented in Table 4.1, the calculations are performed for each ON source interval. The obtained response factor as a function of energy during the observation No.5 is shown in Figure 6.9. The systematic uncertainty is as much as 3% in the calculation as is shown in Section 3.8.

Inefficiency due to the PSD window. As discussed in Section 3.4.1, a fraction of clean hits on GSO may not pass the PSD window, when the temperature of the crystal goes down at the ceiling altitude. We estimate the fraction of hard X-rays/gamma-rays which is cut away by the PSD window. The distribution of the

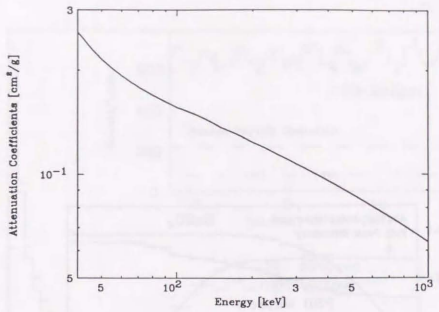

Figure 6.8: Attenuation Coefficients for photons in Air

zero crossing timing in the PSD are monitored by TAC module and are used to calculate the event rate that passes the PSD window for each energy bin. The averaged efficiency over 64 counters is presented in Figure 6.9. The systematic uncertainty is estimated from the statistical errors associated with peak position and standard deviation in fitting the TAC distribution to gaussian distribution and turns out to be 0.9%.

Attenuation due to light reflector($BaSO_4$). On the surface of GSO crystal, $BaSO_4$ is painted as a light reflector. This causes the attenuation of incident photons as shown in Figure 6.9. The surface density of $BaSO_4$ was measured after the flight and the cross-section is calculated using PEGS4 code. From the error in measureing the weight of $BaSO_4$ (41.4$\pm$0.5g from 64 pieces of GSO crystal), the systematic uncertainty in the factor is estimated to be 0.9%.

The total efficiency is the product of these factors and is shown in Figure 6.9. The systematic uncertainties in factors are demonstrated in the 9th energy bin. Among them, the largest uncertainty is in the calculation of "full peak efficiency and angular acceptance" (3%). The total efficiency is the product of these individual factors The systematic uncertainty is estimated to be 3.3% in total.

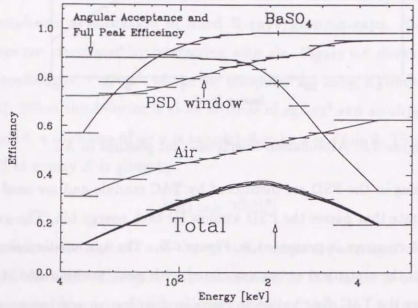

Figure 6.9: Energy dependent efficiency factors for No.5 ON source interval in the observation of Cen A. The systematic uncertainties in factors are demonstrated in the 9th energy bin (indicated by the arrow). Among them, the largest uncertainty is in the calculation of "full peak efficiency and angular acceptance" (3%). The total efficiency is the product of these individual factors The systematic uncertainty is estimated to be 3.3% in total.

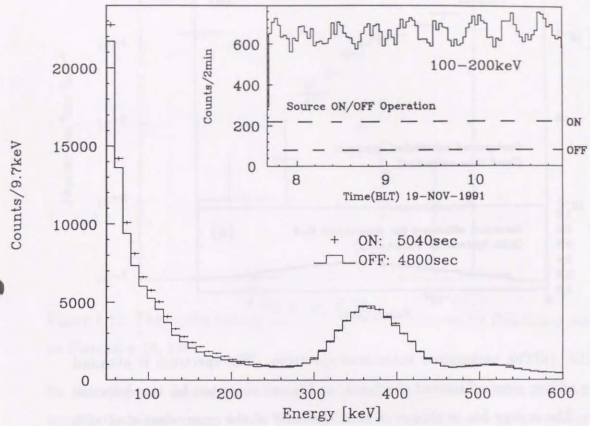

Figure 6.10: The ON and OFF source spectra obtained during the observation of Cen A summed over 64 counters. One bin in the histogram corresponds to be 9.7 keV. Observation time is 5040 sec for ON source and 4800 sec for OFF source. Upper right panel shows the time variation of integrated counts between 100 keV and 200 keV.

6.5 Energy Spectrum of Cen A

We present the ON source and OFF source spectra summed over the 64 counters in Figure 6.10. The total time of ON and OFF source observation is 5040 sec and 4800 sec, respectively. The OFF source spectrum is scaled by a factor of $\frac{5040}{4800}$ in the figure. Upper-right panel in the Figure shows the time variation of integrated counts between 100 keV and 200 keV and the pointing operation. These two figures demonstrate that the signal-to-background ratio for the observation of Cen A is about 15% in the energy range 100-200 keV.

Using the dead time derived in Section 6.3, the ON source and OFF source spec-

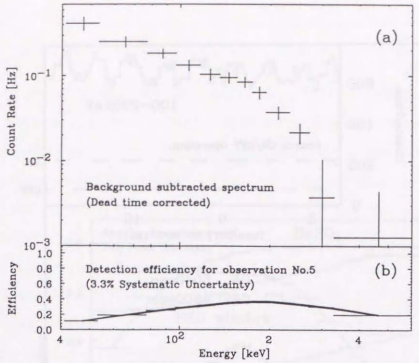

Figure 6.11: (a)The background subtracted spectrum. The spectrum is obtained simply by adding nine subtracted spectrum, and is not corrected for the detection efficiency. The energy bin is chosen so that the ratio of the error associated with count rate(Δy) over count rate(y) has similar value in each energy bin ($\Delta y/y \sim$ 20%). (b)The detection efficiency is shown for comparison. The error shown in the figure is the systematic uncertainty described in Section6.4.

trum are corrected separately before the latter is subtracted from the former. In Figure 6.11(a) we present the background subtracted spectrum. The spectrum is obtained simply by adding nine subtracted spectrum. The spectrum is not corrected for the detection efficiency and is "raw" spectrum. The energy bin is chosen so that the ratio of the error associated with count rate(Δy) over count rate(y) has similar value in each energy bin ($\Delta y/y \sim 20\%$).

These nine spectra are corrected for the effcinecy factors prepared for each time interval as described in the previous section. Summing these spectra, the spectrum of Cen A is obtained as presented in Figure 6.12.

Figure 6.13 shows the time variations of the count rate. integrated between 53 keV and 116 keV (a), 116 keV and 271 keV (b). The data in the figure were corrected

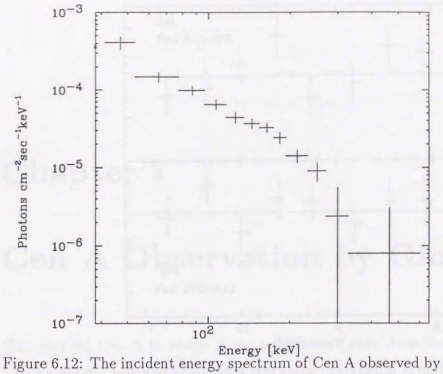

Figure 6.12: The incident energy spectrum of Cen A observed by Welcome-1 detector on November 19, 1991

for the efficiency factors (Section 6.4). The horizontal lines indicate the averaged count rates in each energy band. The nine points are consistent with a constant flux.

6.6 Energy Spectrum of the Crab Nebula

We used the Crab Nebula/Pulsar as a calibration source to calibrate the absolute flux. The period of the observation was , however, devoted to the calibration of the pointing accuracy of the telescope using our star camera. In this calibration period, the Crab Nebula/Pulsar was observed 11° degrees away from the line of insight of the detector. Figure 6.14 shows the energy spectrum of the Crab Nebula plus Pulsar in 1410s observation time when the telescope pointed 11 degrees away from the Crab Nebula/Pulsar. The analysis was carried out along with the procedure described in the previous Sections. The spectrum reasonably agrees with the reported measurements by other experiments [48].

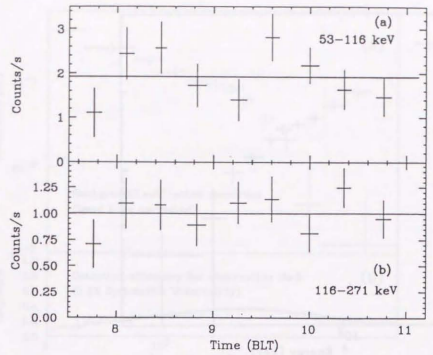

Figure 6.13: Time variation of integrated counts rate between 53 keV and 116 keV (a), 116 keV and 271 keV (b). The data in the figure were corrected for the efficiencies.

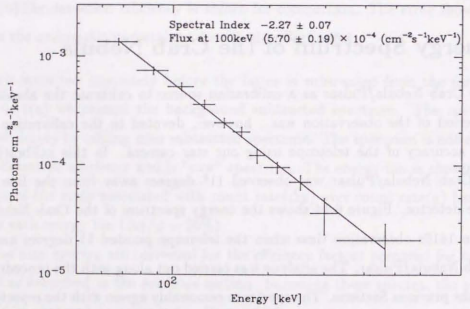

Figure 6.14: Energy Spectrum of the Crab Nebula/Pulsar in 1410s observation time when the telescope pointed 11 degrees away from Crab Nebula/Pulsar (~300 mCrab emissions).

Chapter 7

Cen A Observation by Ginga

We observed Cen A to study X-ray spectra by Large Area Counter(LAC) [49] on board *Ginga* satellite [50].

7.1 Instrumentation

The LAC consists of eight indentical proportional counters with a total area of 4000cm^2 which covers the energy range 1.5-37 keV. The field of view is 1.08°×2.0° (FWHM). The efficiency of the LAC is shown in Figure 7.1 where solid line denoted as "TOP+MID" is applicable to the observation of Cen A. A Detail description of LAC is presented in Turner *et al.* [49].

7.2 Observation

Ginga observed Cen A on March 8~9, 1989 and February 7~9, 1990. Six LACs out of 8 were used in the observation; the total geometrical area was 3000cm^2. Removing the time interval when the background counting rate was high, we prepared useful 7 data set (two set in 1989 and five set in 1990) for spectral analysis(Table 7.1). Detail descriptions about selecting time intervals and background subtraction are presented by Kano [51]. Using the count rate spectra, we carry out the spectra analysis of Cen A in X-ray range (Section 8.2).

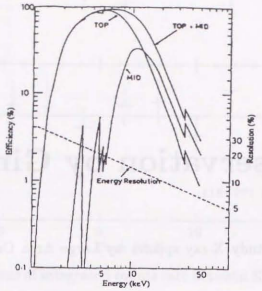

Figure 7.1: The efficiency of the LAC. Solid line denoted as "TOP+MID" is applicable to the observation of Cen A.

Observations	Observed Date	Exposure [sec]
1	Mar. 3, 1989	6049.3
2	Mar. 3, 1989	12981.1
3	Feb. 7, 1990	3772.3
4	Feb. 8, 1990	4164.4
5	Feb. 8, 1990	4721.9
6	Feb. 8, 1990	2186.6
7	Feb. 9, 1990	7691.3

Table 7.1: The observation log for Cen A by Ginga.

7.3 Analysis of the X-ray Spectra

We use the standard method adopted by Ginga group in the anlysis of X-ray spectra. A trial model function is assumed for the X-ray spectra: then fold it through the response matrix and make a trial spectrum. We compare it with the observed spectrum by means of the least χ^2 method. The spectral parameters are determined by minimizing the χ^2 of the fit.

We prepared several model functions to account for the observed spectrum. They includes

1. Power law spectrum for the continuum emission
2. Absorption due to the matter along the line of sight
3. Gauss function for the emission line
4. Thermal bremsstrahlung spectrum

Among them the absorption(No. 2) is introduced as a multiplicative factor expressed as,

$$exp(-n_H\sigma(E)) \tag{7.1}$$

where n_H is equivalent hydrogen column [cm^{-2}] and σ is the photoelectric cross section using Wisconsin [52]. The thermal bremmsstrahlung spectrum(No. 4) is based on the Kellogg, Baldwin and Koch polynomial fits to the Kanzas and Latter numerical values [53].

The fits to the data are described in Section 8.2.

Chapter 8

Results and Discussion

8.1 Hard X-ray Spectrum of Cen A (40-600 keV)

We analyze the spectra of Cen A obtained in the balloon experiment (Figure 6.12) to gain insight about the radiation mechanism of AGN. As is reviewed in Chapter 2, the radiation mechanism is characterized by its spectral shape.

The continuum emission of AGN is known to have a power law shape below 100 keV, we firstly fit the observed spectrum to the single power law expressed as,

$$F = I(E/100)^{-\alpha_1}, \tag{8.1}$$

where I is the photon flux at 100 keV in [photons/cm^2/sec/keV] and α_1 is the power law index. The best fit values for the parameters and their associated errors are shown in the first row of Table 8.1. The best fit gives χ^2=11.3 (degree of freedom (dof) of 10). The measured intensity at 100 keV is higher by $\sim$ 60% than that observed by the POKER on May 1989 [30], the most recent observation in hard X-ray range.

Secondly, we apply fit to the broken power law. The broken power law model is not a model derived from physical processes at the emission site, but rather an empirical model to describe the spectrum. It is expressed as,

$$F = \begin{cases} I(E/100)^{-\alpha_1} & E \leq E_b \\ IE_b^{(\alpha_2-\alpha_1)}(E/100)^{-\alpha_2} & E > E_b \end{cases} \tag{8.2}$$

Model	χ^2/dof	I	α_1	E_b (keV)	α_2
Single Power Law	11.3/10	7.2± 0.4	2.06±0.10		
Broken Power Law	4.3/8	7.4± 0.4	1.84±0.15	186±24	$3.7^{+1.8}_{-0.9}$

Table 8.1: The best fit parameters for the hard X-ray spectrum of Cen A. The parameters are defined in Equation (8.1) and (8.2).

where E_b is the break point in the spectrum, and α_1 and α_2 are photon indexes below and above the break respectively. The best fit gives 4.3/8 for χ^2/dof (Table 8.1). According to the F TEST [54], the 0.59 reduction in χ^2 per degree of freedom generally has only 0.3% chance of being exceeded by random data, and thus favors the break in the spectrum. The confidence level is 33 % for χ^2/dof= 11.3/10, however, and it is hard to exclude the single power law model from from the hard X-ray spectrum alone.

Even when the systematic uncertainty associated with the detection efficiency (3.3%, see Section 6.4) is involved with the statistical errors of the spectrum, the confidence level does not change significantly, 36% for the single power law fit.

8.2 X-ray Spectrum of Cen A (2-30 keV)

The emission from Cen A in the X-ray region is studied using the spectrum obtained by Ginga. We carry out fits for the data along the standard Ginga method described in Section 7.3. Since the intrinsic absortion was reported in Cen A by other experiments [27, 55], we firstly fit the data to power law with absorption. The result for the Observation 3 is shown in Figure 8.1(a). The fit gives χ^2/dof = 1565/33 and is not acceptable. In the residual plot, one can see the emission feature around 7 keV and low energy excess below $\sim$ 3 keV.

We then add two components to the model function: a gaussian function for the emission feature and bremsstrahlung for the low energy excess. The best fit parameters and associated errors are listed in Table 8.2. The center energy of the

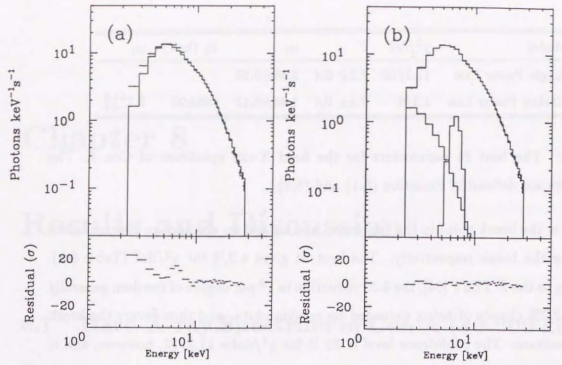

Figure 8.1: X-ray Spectrum of Cen A. Fits to models (Observation 3)

emission line is consistent with the line from the Fe fluorescence emission.

Throughout the seven observations(Observation 1$\sim$ 7), the spectra show a power law shape with absorption by $n_H = 1.6 \times 10^{23}\mathrm{cm}^{-2}$ below 10 keV.

We now concentrate on the variability of the power law component with time. Table 8.3 summarizes the results of fits to the power law for the 7 observations. Although the power law intensity varies by about 30% within a day, the photon index of the power law spectrum remains stable at around 1.80 (1.79 - 1.82) for all 7 observations.

We unfold the Ginga spectra in order to compare them spectra with the hard X-ray spectrum. The result for the third data set is presented in Figure 8.2. The thin line is the best fit model to the power law with the absorption($\alpha = 1.79, n_H = 1.57 \times 10^{23}\mathrm{cm}^{-2}$).


```
-------------------------------------------------------------------------------
mo = wabs (powerlaw) + bremss + gaussian
Model Fit Model   Component     Parameter   Value
par   par comp index  type
  1    1    1    1  powerlaw    PhoIndex    1.78878      +/- 0.15860E-01
  2    2    1    0  powerlaw    norm        431.475      +/-  18.036
  3    3    2    1  wabs        nH 10^22    15.2763      +/-  1.6019
  4    4    3    1  bremss      kT(keV)     1.68971      +/-  2.8610
  5    5    3    0  bremss      norm        30.4164      +/-  80.079
  6    6    4    1  gaussian    LineE       6.45016      +/- 0.60638E-01
  7    7    4    2  gaussian    Sigma      0.365769      +/- 0.10124
  8    8    4    0  gaussian    norm        2.12518      +/- 0.34511
-------------------------------------------------------------------------------
%Current statistic =      45.59     using     36 PHA bins.
```

Table 8.2: Best fit parameters for X-ray data obtained Ginga (Observation 3)

Observations	1	2	3	4	5	6	7
Power Law Intensity(I)	4.4	5.0	5.4	4.9	4.6	3.9	5.0
Photon Index(α)	1.79	1.80	1.79	1.82	1.81	1.81	1.81
Absorption (n_H)	1.64	1.64	1.57	1.55	1.61	1.57	1.54

Table 8.3: Best fit parameters for X-ray data obtained by Ginga; including power law intensity(I) of 1-10 keV interval [10^{-10}erg/cm^2/s], photon index(α), column density of hydrogen (n_H) [$\times 10^{23}\mathrm{cm}^{-2}$] at each time interval. Errors for each parameter is as much as 0.2 for I, 0.02 for α and 0.08 for n_H, respectively at 90 % confidence.

8.3 Results of Combined Spectrum

In this section, we compare the hard X-ray data obtained by Welcome-1 with X-ray data by Ginga and study the wide-band energy spectrum from 10 keV to 600 keV. Among the seven sets of X-ray data, we choose the one obatined in Observation-3 because the absolute flux extrapolated to Welcome-1 energy range(40keV to 150keV) reaches 60% in intensity as shown in Figure 8.2. The photon index determined for this data set is $\alpha = 1.79 \pm 0.01$ while that for Welcome-1 spectrum from 40 keV to 190 keV gives $\alpha = 1.8 \pm 0.14$: they coincide with each other perfectly well.

We assume that the photon spectrum of Cen A extended with the photon index $\alpha = 1.8$ from the Welcome-1 region down to the Ginga region at the time of Welcome-1 observation. This assumption is natural when we consider the observational fact for Cen A that the photon index of the power law component remains stable even the absolute intensity changes largely [9]. as has been reviewed in Section 2.6.2; below $\sim$ 100 keV the photon index have been distributed within narrow range of 1.6$\sim$1.8 for past two decades. We analyze the combined spectrum under this assumption.

Firstly, we fit hard X-ray spectrum to the single power law with the photon index obtained from the Ginga ($\alpha_G = 1.79$). The fit gives χ^2=18.7 for hard X-ray range (40 keV - 600 keV) and it is inconsistent at 6.7% confidence level (dof=11)(Figure 8.3). Even if we take the systematic uncertainty of 3.3% into account, the confidence level remains 7.4%.

To obtain better representation of the data we apply the fit to the broken power law expressed as Equation(8.2). The result is presented in Figure 8.4. The break point in the spectrum is determined to be $E_b = 184 \pm 22$ keV when we fix the photon index of the lower energy portion to be α_G. The photon index above the break is $\alpha = 3.7^{+1.6}_{-0.9}$ (χ^2=4.4, dof=9 for hard X-ray part). Table 8.3 lists the results of the fits.

The value of α_G is indicated as horizontal line in Figure 2.7 and 2.9. Note that if we use the mean index of 1.7 inferred from past observations (Section 2.6.2), the single power law fit is inconsistent at 1.2% confidence level and the break is stressed

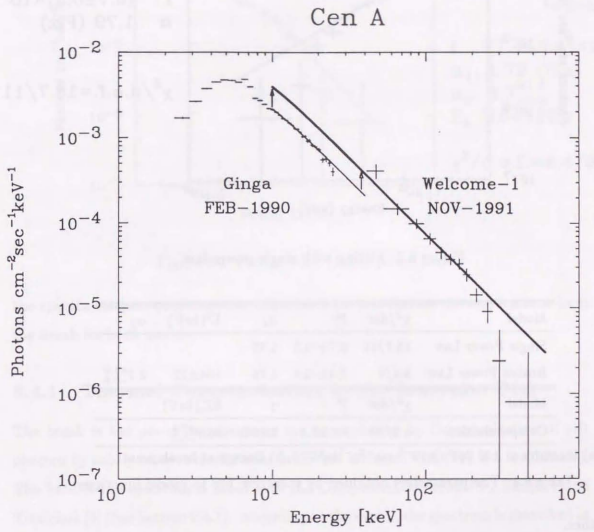

Figure 8.2: Comparison with Ginga data. The thin line is the best fit model of power law spectrum with absorption(α =1.79,$n_H = (1.57 \times 10^{23})$ to the combined spectrum (10-600 keV). and the bold line is the same extended to the Welcome-1 energy range with 60 % increase in intensity. The value of 60% was determined as the result of fitting of the Welcome-1 spectra with fixed α of 1.79

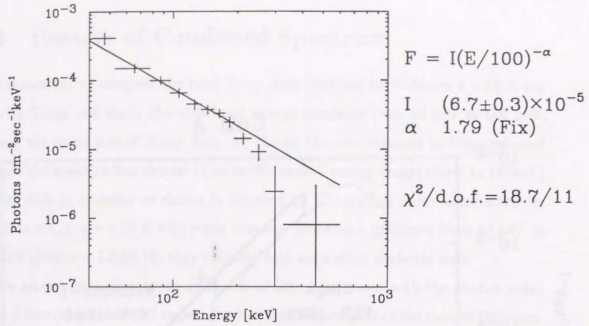

Figure 8.3: Fitting with single power law

Model	χ^2/dof	I[a]	α_1	E[b](keV)	α_2
Single Power Law	18.7/11	6.7± 0.3	1.79		
Broken Power Law	4.4/9	7.4± 0.4	1.79	184±22	$3.7^{+1.6}_{-0.9}$
Model	χ^2/dof	I[a]	γ	kT_e(keV)	
Comptonization	4.9/10	7.6±0.5	2.9941	$56.9^{+7.5}_{-5.7}$	

a) Intensity at 100 keV ($\times 10^{-5}$ cm^{-2}s^{-1}keV^{-1}), b) Energy at break point

Table 8.4: The parameters obtained by spectrum fits to model functions

further.

8.4 Implications on the Emission Mechanism

The main conclusion derived in the previous sections is that the energy spectrum of Cen A shows a break around 200 keV. The constraint on the emission mechanism can be set by the spectral feature around break point: Comptonization predicts exponential decline above the break while the SSC model predicts more smooth decline. Due to the limited statistics in the data of the present study it is difficult to discuss how

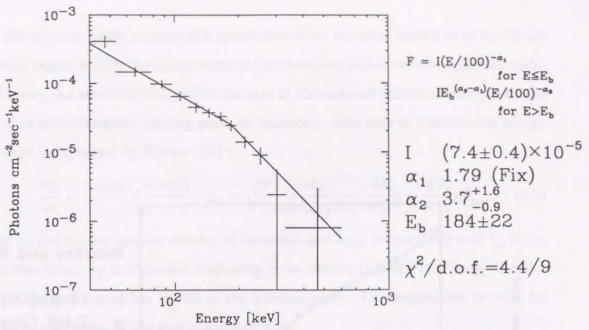

Figure 8.4: Fitting with broken power law

the spectra steepen quantitatively. Therefore, we will discuss the implications from the break for both models.

8.4.1 Thermal Comptonization in the Accretion Disk

The break in the power law spectrum can be explained by Comptonization of soft photons by mildly relativistic electrons in the hot accretion disk ($kT_e >$ a few 10 keV). The hard X-ray spectrum is fitted with the Comptonization model by Sunyaev and Titarchuk [3] (See Section 2.4.1). According to the model, the spectrum is described in terms of the electron temperature (kT_e) and γ. An index of a power law approximation to the data for $E_b < kT_e$ is given by $\alpha = (\gamma + 9/4)^{1/2} - 1/2$. We use $\gamma = 2.99$ which is calculated from $\alpha = 1.79$. The result is presented in Figure 8.5. The best fit parameter is the temperature of $kT_e = 56.9^{+7.5}_{-5.7}$. For a spherical geometry, an optical depth is given by,

$$\tau = \sqrt{\frac{\pi^2 m_e c^2}{3kT\gamma}} - \frac{2}{3}$$

and becomes $\tau = 2.5 \pm 0.2$.

The electron temperature and the optical thickness extracted from our observa-

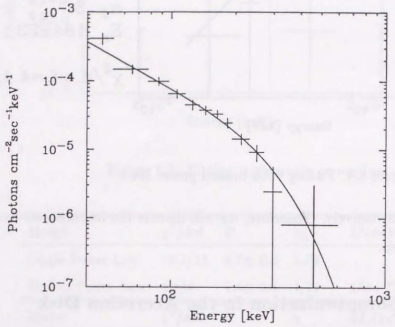

Figure 8.5: Fitting with Sunyaev and Titarchuk[3] model

tion allows us to make a reasonable guess about the physical condition of the X-ray emitting region within the frame work of the standard picture of the accretion disk.

To keep the accretion disk stable the rate of electron-ion energy exchange and the rate of inverse Compton cooling must be balanced. The rate of electron-ion energy exchange is expressed by Spitzer [56] :

$$\frac{dE}{dt} = \frac{3}{2}\frac{n_e(kT_p - kT_e)}{t_{eq}}, \quad t_{eq} = \sqrt{\frac{\pi}{2}}\frac{m_p}{\sigma_T c m_e n_p ln\Lambda}\left(\frac{kT_e}{m_e c^2} + \frac{kT_p}{m_p c^2}\right)^{3/2} \tag{8.3}$$

where n_e and n_p are number density of electrons and ions, respectively and t_{eq} is the relaxation time. σ_T is Thomson scattering cross section (=6.65×10^{-25}cm^2) and $ln\Lambda$ is the Compton logarithm ($\approx$ 20 in the present case). This expression is valid for two-body relaxation in the non-relativistic case.

In the steady-state, above heating rate must be balanced with the rate of inverse Compton cooling which is given by [15]:

$$\frac{dE}{dt} = \left(\frac{4kT_e}{m_e c^2}\right)\sigma_T c n_e U_{ph}. \tag{8.4}$$

In Equation(8.4) U_{ph} is the radiation energy density; if the source is optically thick to scattering, then diffusion enhances the radiation energy density which becomes [57]

$$U_{ph} = \frac{L}{4\pi R^2 c}(1 + \tau/3), \tag{8.5}$$

where L is the observed luminosity and R is the size of the emission region.

By equating Equation(8.3) and (8.4), n_e becomes

$$n_e = 1.2 \times 10^{-6}\left(\frac{kT_e}{m_e c^2} + \frac{kT_p}{m_p c^2}\right)^{\frac{3}{2}}\frac{kT_e}{m_e c^2}(1 + \tau/3)\frac{L}{R^2}, \tag{8.6}$$

where we assume that $n_p = n_e$.

On the other hand, using the optical thickness τ, n_e is given by

$$n_e = \frac{\tau}{\sigma_T R} \tag{8.7}$$

By substituting measured electron temperature of $kT_e = 57$ keV and optical thickness $\tau = 2.5$, the relations between R and n_e are calculated from Equation (8.6). Equation (8.7) gives another constraint on R and n_e.

The luminosity L caluculated from the photon spectrum obtained in this study is 1.4×10^{43}erg/s. Here we integrated the Comptonization spectrum (Figure 8.5) in the energy range over 2 keV. Then, R becomes $(4.1^{+0.5}_{-0.3}) \times 10^{11}$cm and n_e becomes $(9.1 \pm 0.5) \times 10^{12}$cm^{-3} respectively. Here we assumed that $kT_p = 100$ MeV (See Section 2.4.1). Note that R obtained here corresponds to $(13^{+4}_{-3}) \times R_s$ which is calculated under the assumption that the observed luminosity reaches the Eddington limit. The errors associated with R, n_e R_s are from the statistical errors with T_e and τ.

The size of the hard X-ray emitted region obtained from our observation is significantly smaller than the upper limit $10^{13} \sim 10^{15}$cm placed by the previous observations of X-ray intensity variation [55, 58].

In the calculation, we assumed $kT_p = 100$ MeV. It is however difficult to estimate the exact value of T_p. The uncertainty of R is calculated is expressed as,

$$\frac{\Delta R}{R} = \frac{3}{2} \frac{\Delta T_p^*}{T_e^* + T_p^*}, \tag{8.8}$$

where T_p^* is $\frac{kT_p}{m_p c^2}$ and T_e^* is $\frac{kT_e}{m_e c^2}\tau$. Here, we fix the luminosity L and the optical thickness. This suggests that the uncertainty of T_p^* results in the same order of that of R as far as T_p^* has the similar value as T_e^* [59].

8.4.2 The SSC Model

As has been reviewed in Section 2.4.2, the SSC model assumes that non-thermal electrons produce soft photons (*e.g.* radio - IR) via synchrotron radiation in magnetic fields and then the synchrotron photons are scattered to hard photons (X-rays/Gamma-rays) by the same electrons. Several authors considered the SSC model for the source model of Cen A [28, 27, 60]. Their discussions are mainly based on the similarity of the spectral indices in the radio-IR and X-rays of the spectrum. The photon index obtained by our observation (1.79) is consistent with those used in their models($\alpha = 1.3 \sim 1.8$).

In order to verify the SSC model however simultaneous multi-frequency observations must detect the correlation between the fluxes in the two wave bands. Beall *et al.* carried out such observation at radio frequencies of 10.7, 31.4, 85.2, and 89

GHz and at X-ray energies greater than 20 keV. They reported that the variations in X-ray observations did not follow those in the radio band. This means that the link between these two components is weak and the SSC model does not apply to the Cen A emission mechanism.

8.5 Comparison with Other Observations

We compare our results with the results of previous observations in the hard X-ray and gamma-ray range. Gehrels *et al.* obtained the flux from Cen A on November 1981 by Low Energy Gamma-Ray Spectrometer(LEGS) in the energy range 70-500 keV [61]. On October 1982, the MPI Compton Telescope detected the gamma-ray from Cen A in the energy range 700 keV to 10 MeV whose statistical significance of the source was 4.1σ [62]. The combination of the MPI data with the limit set by SAS 2 [31] and COS B [32] above 35 MeV suggests that the spectrum of Cen A had once steepened somewhere around 10 MeV. These data are shown in Figure 8.6 together with the data of the present experiment.

Figure 8.6 suggests that over ~200 keV the photon index of the spectrum of Cen A have varied with time. If the power law spectrum continued to $\sim$ 10 MeV in the past as in the MPI observation, the break point must have moved left some time between 1982 and 1991.

Within the frame work of the Comptonization model, change in the break point is tied to change in electron temperature. Since the change in luminosity is small, this suggests that the source was more optically-thin and the emission region was larger at the time of the MPI observation.

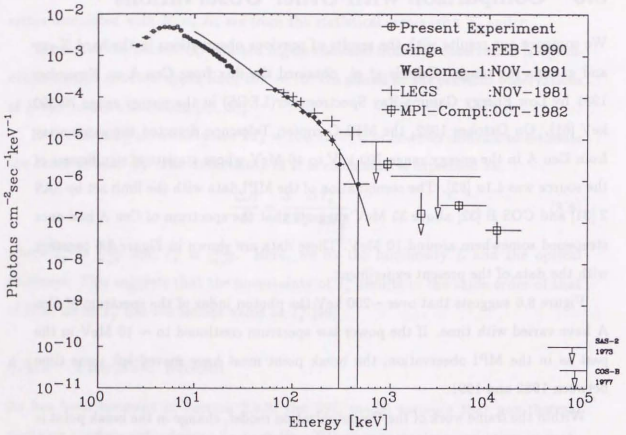

Figure 8.6: Comparison with Other Observations

Chapter 9

Conclusion

The hard X-ray and gamma-ray (40-600 keV) spectrum of Cen A was observed with the Welcome-1, which is newly developed and on-board a balloon on 19 November 1991. The observed flux at 100 keV was 7.2±0.4 photons/cm^2/s/keV. The intensity at 100 keV was found to have increased by $\sim$ 60 % since the latest hard X-ray observation (15-150 keV) by POKER in May 1989. The spectrum shape is best reproduced by a broken power law shape.

To study X-ray spectra of Cen A from 2 keV to 30 keV we also analyzed the data obtained with LAC on board Ginga. Above 10 keV the spectra are well characterized by a power law shape with $\alpha = 1.8$. The Fe emission line is also visible at 6.4±0.1 keV.

We analyzed the combined spectrum of Cen A under the asumption that the photon spectrum of Cen A extends with the photon index $\alpha = 1.8$ from the Welcome-1 region down to the Ginga region at the time of Welcome-1 observation. This assumption is consistent with the observational fact for Cen A that the photon index of the power law component remains stable even the absolute intensity changes largely. The result indicates that there is a break at 185 ± 22 keV. The spectrum is fitted with the broken power law model, one photon index is $\alpha_1 = 1.79$ up to 184 keV and the other is $\alpha_2 = 3.7^{+1.6}_{-0.9}$ above the break.

The indexes obtained by other previous measurements in the 10 keV to a few hundred keV are harder than the ones observed by the Ginga satellite: If we take

the harder or flatter spectrum, the break in the spectrum is more pronounced. We conclude from these analysis that the spectrum is very likely to have a break around 150-200 keV at the time of Welcome-1 observation.

The observed break can be accounted for by the thermal Comptonization model. With the Sunyaev-Titarchuk Comptonization model in the hot accretion disk, the present data determines the electron temperature and the optical thickness to be $kT_e = 56.9^{+7.5}_{-5.7}$ keV and $\tau = 2.5 \pm 0.2$ as the best fit values of our data.

Assuming the two temperature disk model proposed by Shapiro *et al.* for the center of Cen A, we obtain the size of emission region(R) and the density of electrons (n_e) to be $R = (4.1^{+0.5}_{-0.3}) \times 10^{11}$cm and $n_e = (9.1 \pm 0.5) \times 10^{12}$cm^{-3}. Here we use the luminosity of 1.4×10^{43}erg/s caluculated from the spectrum by Welcome-1. The proton temperature is fixed at $kT_p = 100$ MeV. The obtained value of R is significantly smaller than the upper limit ($10^{13} - 10^{15}$cm) placed by the previous X-ray intensity variation. Assuming that the luminosity reaches the Eddington limit, R becomes about 13 times of the gravitational radii. The Fe fluorescence line observed in the present Ginga data gives a strong evidence that the emission is from the accretion disk. Thus, it is very likely that we directly view the the central power house, a super massive blackhole.

Several authors considered the SSC model as the emission mechanism of Cen A. Their discussions are mainly based on the similarity of the spectral indexes between the radio-IR and X-rays of the spectrum. The photon index obtained in the present study (1.79) is consistent with those used in their models. The recent results of multi-frequency observations by Beall *et al.*, however, do not favor the SSC model for Cen A, and we presume that the thermal Comptonization model is more likely the case.

Comparison of our spectrum with other observations in hard X-ray and gamma-ray range implies that the break point moves downwardly from $\sim$ 5 MeV (1982) to $\sim$ 200 keV in our observation(1991).

The present study suggests that the hard X-ray and gamma-ray observation can reveal a clue to clarify the features of the emission of AGN. In order to have further insight to AGN, more sensitive observations in hard X-ray and gamma-ray are

required. The analysis of the background shows that the well-type phoswich configuration works properly to reduce the background. To improve the sensitivity of the detector, we propose for the future observation (1) to narrow the opening angle to reduce the background from the aperture, (2) to develop purer GSO to reduce the internal background, (3) to employ the higher density scintillator(*e.g.* BGO) as the shield part to reduce the background leaking through the shield.

Acknowledgements

This paper is written under the guidance of Professor Tuneyoshi Kamae who gave me valuable advices. The experiment was carried out in collaboration with Brazil. I am indebted to a number of scientists and staffs of the collaborations. Among them are Dr.Takamasa Yamagami; Institute of Space and Astronautical Science, Dr.Ricard Correa and Dr.Angelo Neri; Institute de Pesquisas Espaciais, Mr.Hiroyuki Murakaimi; Rikkyo University, Dr.Masaharu Nomachi; National Laboratory for High Energy Physics. I would like to thank Dr.Tadayuki Takahashi for helpful suggestions and comments in writing the manuscripts. I wish to thank Dr.Hajime Inoue for giving the opportunity to analyze the data of Ginga satellite. I am obliged to my colleagues in lab, especially Dr.Tadahisa Tamura and Mr.Yutaro Sekimoto who patiently helped me in finishing this work.

Finally, my special thanks are due to my family for continuous supports and encouragements.

Bibliography

[1] M. Rees, Observatory **98**, 210 (1978).

[2] Y. Tanaka, "Black Hole X-Ray Binaries," in *Ginga Memorial Symposium* (1992), p. 19.

[3] R. Sunyaev and L. Titarchuk, "Comptonization of X-rays in Plasma Clouds. Typical Radiation Spectra," Astron. Astrophys. **86**, 121 (1980).

[4] T. Jones, S. O'Dell, and W. Stein, "Physics of Compact Nonthermal Sources. I. Theory of radiation processes," **188**, 353 (1974).

[5] G. Bignami *et al.*, "Galaxies and Gamma-Ray Astronomy," Astrophys. J. **232**, 649 (1979).

[6] A. Pollock *et al.*, "Search for Gamma-radiation from Extragalactic Objects Using a Likelihood Method," Astron. Astrophys. **94**, 116 (1981).

[7] A. Fabian and M. Rees, M.N.R.A.S. **187**, 13 (1979).

[8] J. Frank, A. King, and D. Raine, "Accretion Power in Astrophysics," , year (1992).

[9] H. Inoue, "Ginga Observations of the X-ray Spectra of AGN," in *23rd ESLAB Symposium* (1989), p. 783.

[10] R. Rothschild *et al.*, "2-165keV Observations of Active Galaxies and the Diffuse Background," **269**, 423 (1983).

[11] R. Petre *et al.*, "Soft X-Ray Spectral Observations of Quasars and High X-Ray Luminosity Seyfert Galaxies," **280**, 499 (1984).

[12] G. Reichert, "Soft X-Ray Spectral Observations of Low-Luminosity Active Galaxies," **296**, 69 (1985).

[13] O. Williams *et al.*, "The X-ray Spectra of High-Luminosity Active Galactic Nuclei Observed by Ginga," **389**, 157 (1992).

[14] A. Fabian, "X-rays from Active Galactic Nuclei," Physica Scripta **T7**, 129 (1984).

[15] G. Rybicki and A. Lightman, *Radiative Processes in Astrophysics* (Wiley-Interscience, 1979), Chap. 6.

[16] N. Shakura and R. Sunyaev, "Black Holes in Binary Systems. Observational Apperance," Astron. Astrophys. **24**, 337 (1973).

[17] R. Protheoe and D. Kazanas, Astrophys. J. **265**, 620 (1983).

[18] D. Band and J. Grindlay, "The Synchrotron-Self-Compton process in spherical geometries II. Application to Active Galactic Nuclei," **308**, 576 (1986).

[19] F. Makino *et al.*, "X-ray Outburst of the Quasar 3C279," Astrophys. J., Lett. **347**, L9 (1989).

[20] N. Kawai *et al.*, "Multifrequency Observation of BL Lacertae in 1988," Astrophys. J. **382**, 508 (1991).

[21] "BL Lacertae Objects: Accretion, Jets, and Winds," in *The Physics of Accretion onto Compact Objects*, edited by Mason *et al.* (Springer Verlag, 1986).

[22] R. Rothschild *et al.*, "2-165 keV Observations of Active Galaxies and the Diffuse Background," Astrophys. J. **269**, 423 (1983).

[23] K. Hayashida, *Fluctuations in the Cosmic X-ray Background and their Relation to Active Galactic Nuclei*, PhD thesis, University of Tokyo, 1989.

[24] D. Meier *et al.*, "The high-resolution structure of the Centaurus A nucleus at 2.3 and 8.4 GHz," Astron.J. **98**(1), 27 (1989).

[25] C. Bowyer *et al.*, Astrophys. J., Lett. **161**, L1 (1970).

[26] E.D.Feigelson, "The X-ray Structure of Centaurus A," Astrophys. J. **251**, 31 (1981).

[27] R.F.Mushotzky *et al.*, "The X-ray Emitting Galaxy Centaurus A," Astrophys. J. **220**, 790 (1978).

[28] W.A.Baity *et al.*, "Centaurus A (NGC5128) at 2keV-2.3MeV: HEAO 1 Observations and Implications," Astrophys. J. **244**, 429 (1981).

[29] M.Maisack *et al.*, "Hard X-ray Observation of AGN," in *22rd Symp. on Two-Topics in X-Ray Astronomy* (Bologna, Itary, 1989), p. 975.

[30] P.Ubertini *et al.*, "Hard X-ray Observation of Cen A," in *22nd International Cosmic Ray Conference* (Dublin, 1991). OG 1.7.

[31] G.F.Bignami *et al.*, "Galaxies and Gamma-ray Astronomy," Astrophys. J. **232**, 649 (1979).

[32] G.F.Bignami *et al.*, Astron. Astrophys. **93**, 71 (1981).

[33] R. L. Kinzer, W. N. Johnson, and J. D. Kurfess, "A Balloon Observation of the Diffuse Cosmic X-radiation above 20keV," Astrophys. J. **222**, 370 (1978).

[34] K. Takagi and T. Fukuzawa, "Cerium-activatedGD_2SiO_5 single crystal scintillator," Appl. Phys. Lett. **42**, 43 (1983).

[35] H. Ishibashi *et al.*, "Cerium Doped GSO Scintillators and its Application to Position Sensitive Detector," Nucl. Instrum. Methods **NS-36**, 170 (1989).

[36] N. Hanada, *New Gamma Ray Telescopes Using Silicon Detectors*, Master's thesis, University of Tokyo, 1989.

[37] H. Murakami *et al.*, "A Simple Pulse Shape Discriminator Method for the Phoswich Counter," IEEE-NS **39**, 5 (1992).

[38] W. Jonhnson *et al.*, "The Oriented Scintillation Spectrometer Experiment Instrument Description." submitted to Astrophys. J (1992).

[39] W. Johnson *et al.*, Ap and SS **42**, 35 (1976).

[40] MICROWARE, *OS9/68000 ADVANCED SYSTEM SOFTWARE* (1987).

[41] J. Nishimura *et al.*, ISAS REPORT, 1969. 6-1(C),133 (in Japanese).

[42] W. R. Nelson *et al.*, *The EGS4 Code System* (Stanford Linear Accelerator Center, 1985). SLAC-Report-265.

[43] K. Wood *et al.*, "The HEAO A-1 X-ray Catalog," Astrophys. J. **56**, 507 (1984).

[44] J. C. Ling, "A semiempirical model for atromspheric γ Rays from 0.3 to 10 MeV at $\lambda = 40°$," Journal of Geophysical Research **80**(22), 3241 (1975).

[45] V. Shönfelder, F. Graml, and F. P. Penningsfeld, "The Vertical Component of 1–20 MeV Gamma Rays at Balloon Altitudes," Astrophys. J. **240**, 350 (1980).

[46] C. S. Dyer and G. E. Morfill, Astrophys. space Sci. **14**, 243 (1971).

[47] N. Gehrels, "Instrumental Background in Balloon-Borne Gamma-ray Spectrometers and Techniques for Its Reduction," Nucl. Instrum. Methods **A239**, 324 (1985).

[48] W. Cook *et al.*, "Recent Results of Gamma-ray Imaging Observations of the Galactic Center and Crab/A0535+26 Regions," Adv. Space Res. **11**, 8 (8) 191 (1991).

[49] M. Turner *et al.*, Publ. Astron. Soc. Japan **41**, 345 (1989).

[50] F. Makino *et al.*, Astrophys. Letters Commun. **25**, 223 (1987).

[51] T. Kano, *Observations of Cen A by Ginga*, Master's thesis, Rikkyo University, 1991.

[52] R. Morrison and D. McCammon, "Interstelar Photoelectric Absorption Cross Sections, 0.03-10 keV," Astrophys. J. **270**, 119 (1983).

[53] R. Gould, "Thermal Bremsstrahlung from High-temperature Plasmas," Astrophys. J. **238**, 1026 (1980).

[54] P. Bevington and D. Robinson, *Data Reduction and Error Analysis for the Physical Sciences*, 2nd ed. (McGraw-Hill, 1992).

[55] B. Wang, H. Inoue, K. Koyama, and Y. Tanaka, "X-Ray Observation of Centaurus A from Tenma," Publ. Astron. Soc. Japan **38**, 685 (1986).

[56] L. Spitzer, *Physics of Fully Ionized Gases* (Wiley, New York, 1956).

[57] C. Done, G. Ghisellini, and A. Fabian, "Pair loading in compact sources," M.N.R.A.S. **245**, 1 (1990).

[58] A. Lawrence *et al.*, M.N.R.A.S. **181**, 93 (1977).

[59] S. Shapiro, A. Lightman, and D. Eardley, "A Two-temperature Accretion Disk Model for Cygnus X-1: Structure and Spectrum," Astrophys. J. **204**, 187 (1976).

[60] J.E.Grindlay, "Compton-Synchrotron Model for the Nucleus of Centaurus A (NGC 5128)," Astrophys. J. **199**, 49 (1975).

[61] N.Gehrels *et al.*, "The Gamma-ray Spectrum of Centaurus A: A High-Resolution Observation between 70keV and 8MeV," Astrophys. J. **278**, 112 (1984).

[62] P. Ballmoos *et al.*, "Centaurus A Observation at MeV–Gamma-ray Energies," Astrophys. J. **312**, 134 (1987).

参　考　論　文　1

Well-Type Phoswich Counter for Low-Flux X-Ray/γ-Ray Detection

宮崎聡

Well-Type Phoswich Counter for Low-Flux X-Ray/γ-Ray Detection

T. Kamae, S. Gunji, M. Hirayama, S. Miyazaki, T. Nagato, A. Nakao, Y. Sekimoto,
K. Suzuki, T. Takahashi, T. Tamura, M. Tanaka, N. Yamaoka
Dept. of Physics, University of Tokyo, Bunkyo-ku, Tokyo, JAPAN 113
T. Yamagami
Inst. Space Astronautical Science, Yoshinodai, Sagamihara, Kanagawa, JAPAN 229
M. Nomachi
Nat. Lab. for High Energy Physics (KEK), Tsukuba, Ibaraki, JAPAN 305
and
H. Murakami
Dept. of Physics, Rikkyo University, Toshima-ku, Tokyo, JAPAN 171

Abstract

We have developed a new kind of phoswich counters that are capable of detecting low flux hard X-ray/γ-ray from localized sources. The counter consists of a small inorganic scintillator with a fast decay time (the detection part) glued to the interior bottom surface of a well-shaped block of another inorganic scintillator with a slow decay time (the shielding part). The well-shaped shielding part acts as an active collimator as well as an active shield. The whole assembly is viewed by a phototube from the exterior bottom surface of the shielding part. By using an appropriate pulse-shape discriminator (PSD), hard X-rays/gamma-rays that have deposited energy only in the detection part can be selected.

The first model counter was built by using a new scintillator (GSO) in the detection part and CsI(Tl) in the shielding part. A detector system consisting of 64 such phoswich counters (total area $\sim$740cm^2) was flown on board a balloon, setting a limit to the ^{57}Co line flux from SN1987A at around 10^{-4}cm^{-2}s. The sensitivity for continuum flux was around a few $\times 10^{-6}$cm^{-2}s^{-1}keV^{-1} between 100 and 200keV.

Efforts to lower the sensitivity further are underway. In the second model, CsI($T\ell$) was replaced by BGO and radioactive contaminations in GSO were reduced. More improvements are to be made in near future to reach a sensitivity (3σ) around 5×10^{-7}cm^{-2}s^{-1}keV^{-1} for continuum.

I. Well-type Phoswich Counter

The sensitivity of celestial hard X-ray and γ-ray detectors are limited by the background counting rate. In most cases the signal is extracted by subtracting the off-source data from the on-source data. For low flux sources, the S/N ratio in the on-source data is below 1% and the statistical fluctuation in the background sets the sensitivity. Under such circumstances the detector sensitivity can be improved in the following two ways: by enlarging the area to attain higher statistics for the data; or by reducing the background counting rate. The new phoswich counter presented here point to the latter direction.

To reduce the background we have to shield the detector from various external sources and reduce internal background sources. The external radiations are shielded by a planar active shield in a phoswich configuration: in some cases with separate active collimators. The well-type phoswich integrates these two parts by making a deep well out of an inorganic scintillator (Fig.1a). This configuration not only facilitates long active collimation essential in reducing the external background but also provides with a nearly 4π anti-counter for internal $\beta-\gamma$ background as will be shown below.

The well-type phoswich counter has a simple shape and operates at a reduced counting rate by itself. Many units can be assembled in the compound-eye configuration as shown in Fig.1b. Here each unit is surrounded by eight neighbors which can be used as additional active shields.

For the well-type phoswich counter, the light-collection efficiency in the well becomes important. The detection part is viewed, typically, through 8cm of CsI(Tl) (the 1st model) or 6cm of BGO (the 2nd model). The light emitted at the tip of the collimation part must travel 22cm and 27.5cm, respectively, to reach the phototube. We obtained excellent light collection efficiency for the two model counters. In the third model being designed now the depth of the BGO well is 35cm. The pulse shape discriminator becomes very important too: it must work very effectively because the percentage of clean hits on the detection part decreases in proportion to the ratio of the volume of the detection part to that of the shielding part.

We note here some thoughts about the optimum combination of the two phoswich scintillators in reducing the background. The detection part need to have a faster decay time than the shielding part, otherwise two consecutive hits in the shielding part may simulate clean hits on the detection part at an appreciable rate. BGO is the best scintillator for active shielding today.

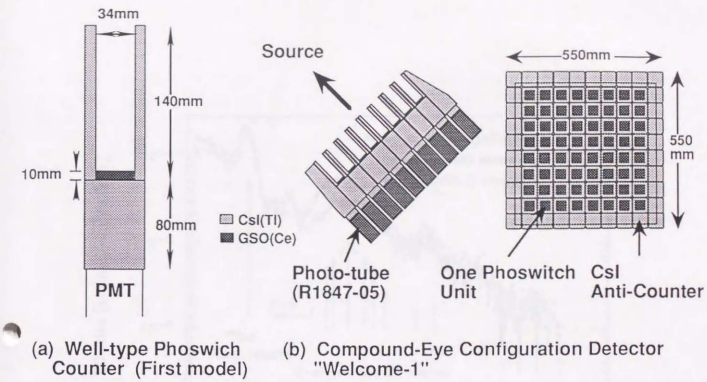

Figure 1: The first model of the well-type phoswich counter and the compound-eye confuguration "Welcome-1".

The problem left to us is to find a scintillator that has both a fast decay time ($\ll$ 300ns) and a high light yield (comparable with NaI($T\ell$)). These thoughts led us to choose the new inorganic scintillator, GSO (Gd_2SiO_5 doped by Ce) developed by Hitachi Chemical (see Table 1) [1,2] for the detection part.

Through the tests on the models and the data taken by a detector ("Welcome-1") flown on a balloon, we learned that the following two points are most important in lowering the background: reduction of internal radioactive impurities and the angular acceptance of the counter. This report will describe what we have accomplished until now and what we plan to do in near future on these points.

Table I Characteristics of Some Inorganic Scintillators

	GSO	CsI($T\ell$)	NaI($T\ell$)	BGO
Density[g/cm^3]	6.7	4.5	3.7	7.1
Decay Time[ns]	60	1050	230	300
Rad. Length[cm]	1.38	1.85	2.59	1.12
Light Yield (PT)	35	60	100	12
Index Refr.	1.85	1.80	1.85	2.15
Hydroscopic?	no	little	yes	no

II. The First Model

The first model counter has been made using CsI($T\ell$) in the shielding part and GSO (Gd_2SiO_5 doped by 0.5%mol Ce) [1,2] in the detection part (Fig.1a). Welcome-1 was made of 64 such units and 36 CsI(Tl) shields (Fig.1b).

In the first model the light emitted at the tip of the CsI($T\ell$) well is attenuated only by 5-10% when it reaches the photo-tube (Hamamatsu R1847-05). The light from GSO, on the other hand, is attenuated to ~50% in the shielding part: CsI($T\ell$) attenuates light significantly near the peak of the GSO emission spectrum (~410nm). With the first GSO samples (Mk1), the light yield measured by the photo-tube was typically 25% of NaI($T\ell$): corresponding to an energy resolution (fwhm) around 8.5% for 662keV gamma-rays. In the well of the first model, however, the resolution deteriorated to ~12%.

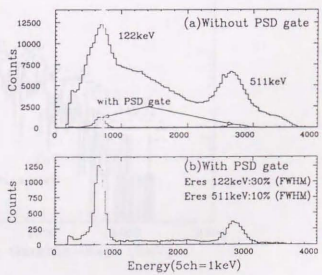

Figure 2: Energy spectra obtained by the first model when irradiated by ^{57}Co and ^{22}Na:(a) Before the PSD filtering (the upper curve) and after the PSD filtering (the lower curve); (b) The enlargement of the lower curve in (a).

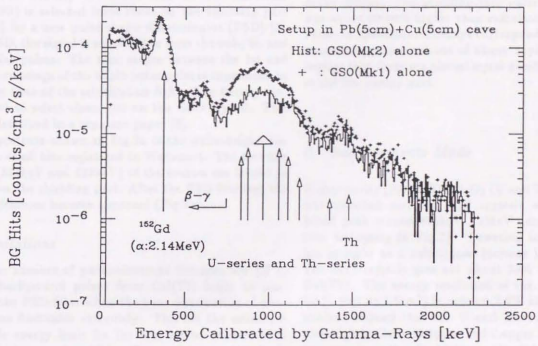

Figure 3: Spectra of the internal background for naked GSO crystals: +, the first sample (Mk1);histogram, the improved sample (Mk2).

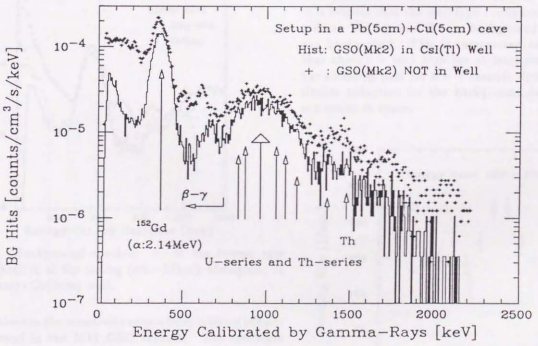

Figure 4: Spectra of the internal background: +, the naked GSO crystal (Mk2); histogram, the GSO in the CsI(Tℓ) well (the first model).

A. *Pulse Shape Discrimination*

In the first model, the clean hits on the detection part (GSO) is selected from those on the shielding part (CsI(Tl)) by a new pulse shape discriminator (PSD) [3]. In the PSD, the signal is amplified to form the uni-, bi- and triple-polar pulses. The time elapse between the 1st and 2nd zero-crossings of the triple-polar pulse is dependent on the decay time of the scintillation light. The timing window is set to select clean hits on the GSO crystal. This PSD is described in a separate paper [3].

The spectrum shown in Fig.2a is the pulse-height distribution of all hits registered in Wecome-1. The two line spectra (511keV and 122keV) of the sources are buried in the hits on the shielding part. After the PSD filtering, the two line features become apparent (Fig.2b).

B. *Limitations*

When the number of photo-electrons becomes low ($E \leq$ 50keV) background pulses from CsI(Tl) begin to pass through the PSD filter when the time distribution of photoelectrons fluctuates extremely. This set the minimum detectable energy limit for the first model counter with this PSD circuit. As will be discussed below, this limit can be pushed down to ~30keV by adopting a different PSD scheme.

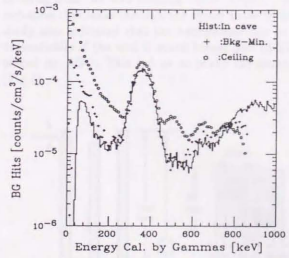

Figure 5: Background spectra: +, at the lowest rate (alt.~1-5km); o, at the cieling (alt.~37km); histogram, in the Pb(5cm)+Cu(5cm) well.

Limitations in the sensitivity comes from internal rdioactivities found in the Mk1 GSO crystals. The spectrum shown by + marks in Fig.3 was obtained when a GSO crystal (Mk1: 3.4×3.4×1.0cm^3) was attached to the phototube and placed in an enclosure made of 5cm Cu and 5cm Pb. In this spectrum, contamination of radioactive isotopes in GSO is apparent. The spectrum include a peak around 300-400keV (calibrated by γ-rays) due mostly to ^{152}Gd(abundance=0.2%, 2.14MeV α decay, half-life 1.1 × 10^{14}y) and a broad enhancement around 800keV-1.2MeV due to the α decays in the uranium and thorium decay chains. The counting rate under the ^{152}Gd peak was about 80-90% higher than calculated and that of the uranium and thorium decays corresponded roughly to the measured contaminations of about 2ppb in weight. This implies that there are almost equal number of $\beta-\gamma$ decays in the low energy part.

C. *Improvements Made*

Higher purity (99.999%) Gd_2O_3 (U and Th less than 1ppb) was obtained and the Mk2 crystals were made. The broad peak around 800keV-1.2MeV decreaced by 30-50% (the histogram in Fig.3). Lowering impurities in GSO has brought us a substantial increase in the light yield. The Mk2 crystals give out about 35% of the yield from NaI(Tl). The energy resolution of the stand alone crystal (1.8×1.8×1.5cm^3) is around 7.0% at 662keV. Furhter analysis showed that the U and Th contaminations are very high in CeO_2 (1.4ppm and 5.4ppm respectively). We are now requesting for higher purity Gd_2O_3 (U and Th < 0.3ppb) and CeO_2 (U and Th < 10ppb).

The well-type configuration serves to reduce the background by $\beta-\gamma$ decays. In Fig.4 the background of a Mk2 crystal with and without a CsI(Tl) well is compared. It is evident that the well-type configuration substantially reduces the internal $\beta-\gamma$ background and the cosmic-ray background. This is interpreted as due to the fact that chance is very high for at least one gamma-ray hit the shielding part for $\beta-\gamma$ cascade decays. This implies similar reduction for the background due to the nuclear activation in space.

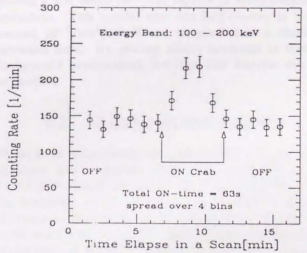

Figure 6: Counting rate variation when the crab nebula/pulsar cross the detector opening.

D. *Balloon Flight*

Welcome-1 was flown onboard a balloon from the INPE balloon base in Cachoeira Paulista, Brazil in 1990. The background spectra observed at the lowest rate (altitude~1-5km) and at the ceiling (altitude~37km~4.0mb) are compared with the one obtained in the Pb(5cm)/Cu(5cm) cave on the ground in Fig.5. Note that the background rate at the minimum is roughly the same as that measured in the Pb and Cu cave. The increase at the ceiling altitude is consistent with estimations of the flux generated in the earth atomosphere [4]: a part from the opening (hwhm: $7.4\times7.4\mathrm{deg}^2$) and the other through the CsI($T\ell$) shield.

The potentiality of the well-type phoswich detector is borne out in Fig.5: The intrinsic background rate is a few $\times10^{-5}/\mathrm{cm}^2/\mathrm{s/keV}$. This point is also demonstrated by the S/N ratio for the Crab nebula/pulsar taken during a pointing operation (Fig.6). We note here that atomosphere ($4\mathrm{g}/\sin40^\circ$) attenuates the signal by a factor around 2.0-2.5: Should this attenuation go away as for a satelite observation, the S/N ratio will be greater than 1.

III. The Second Model

A Monte Carlo study showed that the background spectrum observed in the flight is dominated by the radiation entering from the well opening below 200keV and by the radiation that leaks through the shield above 200keV. The study also indicated that the background can be reduced dramatically if the well is made longer and CsI(Tl) is replaced by BGO. This led us to make the second model (Fig.7).

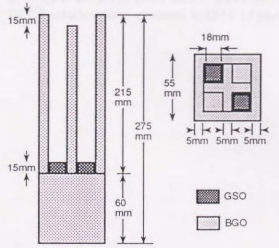

Figure 7: The second model counter.

In the second model, the Mk2 GSO crystals were used. The scintillation decay time is shorter for BGO than for CsI($T\ell$) (Table 1) and the PSD used with the first model [3] will not reliably work. Another PSD in which the photo-tube signal is integrated by two amplifiers with different time constasts (τ ~100ns and 500ns) is used in the second model. In Fig.8, the background spectra of the Mk2 GSO crystal ($1.8\times1.8\times1.5\mathrm{cm}^3$) in the CsI($T\ell$) well (the first model) and in the BGO well (the second model) are compared. The $\beta-\gamma$ decays are rejected more efficiently now. The background level is already below $10^{-5}/\mathrm{cm}^2/\mathrm{s/keV}$. Besides the radioactivities, the two gamma-lines due to ^{207}Bi are now visible. A thorough study has been made about this ^{207}Bi contamination in BGO crystals by Lewis[5]. We are now in the process of obtaining ^{207}Bi-free BGO crystals.

IV. Improvement Plans

Besides the efforts already mentioned, a new BGO well (the third model) has been designed. The lowest energy the well-type phoswich works efficiently is lowered to around 30keV in the second model. The bottom of the well provides now a perfect low-background environment. The background level will be lowered farther if we obtain purer materials. We plan to place several layers of thick PIN-type Si detectors (eg. [6]) in the well to intercept hard X-rays. A reasonable detection efficiency is expected to extend up to ~130keV. These efforts are focussed toward the proposed hard X-ray satelite project[7].

V. Conclusions

The well-type phoswich counter concept has been proven to be very effective in reducing the external and internal backgrounds. We expect the background level to be around a few times $10^{-6}/\mathrm{cm}^2/\mathrm{s/keV}$ in astronomical observations. This implies that low-flux sources at a level around $10^{-7}/\mathrm{cm}^2/\mathrm{s/keV}$ can be studied in a short observation time. By placing silicon detectors in this low background environment, low-level line features can also be studied.

VI. Acknowledgements

We wish to acknowledge the collaboration by the INPE scientists and engineers under the leadership of Dr. V.W.J.H.Kirchhoff and by the ISAS balloon group under the leadership of Dr. N.Yajima in the balloon flight of Welcome-1. Reduction of the radioactive contamination in Gd and Ce would not have been possible without active cooperation of Hitachi Chemical and Shinetsu Chemical. This work has been carried out under a support of Grant-in-Aid by Monbusho.

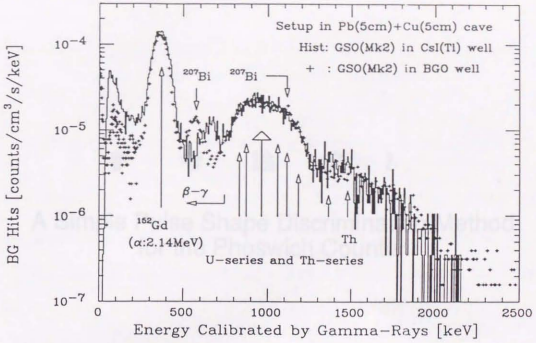

Figure 8: Spectra of the internal background: +, the naked GSO crystal (Mk2); histogram, the GSO in the BGO well (the second model).

References

[1] K. Takagi and T. Fukazawa, *Appl. Phys. Lett.* **42** 43 (1983).

[2] H. Ishibashi, K.Shimizu, and K.Susa, *IEEE* **NS-36** 170 (1989).

[3] H. Murakami et al., *This conference.*

[4] V. Schönfelder, F. Graml, and F.-P. Penningsfeld, *Astrophys. J.*, **240** 350 (1980).

[5] T. A. Lewis, *Nucl. Instr. Meth.*, **A264** 534 (1987).

[6] S. Gunji et al., *Nucl. Instr. Meth.*, **A295** 400 (1990).

[7] DUET collaboration: proposal to ISAS (Approved).

参　考　論　文　2

A Simple Pulse Shape Discrimination Method for the Phoswich Counter

宮崎聡

A Simple Pulse Shape Discrimination Method for the Phoswich Counter

H. Murakami
Dept. of Physics, Rikkyo University, Toshima-ku, Tokyo, JAPAN 171
S. Gunji, M. Hirayama, T. Kamae, S. Miyazaki, Y. Sekimoto,
T. Takahashi, T. Tamura, M. Tanaka, N. Yamaoka
Dept. of Physics, University of Tokyo, Bunkyo-ku, Tokyo, JAPAN 113
T. Yamagami
Inst. Space Astronautical Science, Yoshinodai, Sagamihara, Kanagawa, JAPAN 229
M. Nomachi
Nat. Lab. for High Energy Physics (KEK), Tsukuba, Ibaraki, JAPAN 305
and
K. Mori
Clear Pulse Co.,Ltd., Chuo, Ohta-ku, Tokyo, JAPAN 143

Abstract

We have developed a simple pulse shape discriminator (PSD) for applications where a large number of channels are used within limited space and electric power. In the PSD, the output signal from a photomultiplier is differentiated and integrated to form a triple-polar pulse. The time interval between the first and second zero crossings depends on the decay time of the scintillation light. The circuit selects signals from the proper scintillator by using this interval. By this method, we can significantly reduce the effect of time slewing in the low energy region. We have successfully operated sixty four channels of the PSD in a balloon borne hard X-ray experiment.

I. Introduction

We have developed a simple pulse shape discriminator (PSD) for a new type phoswich counter (the well-type phoswich counter) [1]. The counter consists of a small inorganic scintillator with a fast decay time (the detection part) glued to the interior bottom surface of a well-shaped block of another inorganic scintillator with a slow decay time (the shielding part). The well-shaped shielding part acts as an active collimator as well as an active shield. The whole assembly is viewed by a phototube from the exterior bottom surface of the shielding part. The pulse-shape discriminator (PSD) selects hard X-rays/gamma-rays that have deposited energy only in the detection part.

Phoswich counters requires a PSD to extract signals from admixture of background pulses. Several PSD methods have been proposed until now[2,3]: (1) the leading edge/zero crossing method, (2) the double integration method, and (3) the rise-time measurement method using constant fraction discriminators.

For applications where a large number of channels is used within limited space and electric power consumption, the circuit must be compact and simple. Only the first method satisfies these conditions, but it suffers from time slewing especially for small pulses. The present PSD circuit was developed to obtain a good S/N ratio even in the lower energy region.

The design of the present circuit was optimized for signals from the first well-type phoswich counter. The counter uses a new scintillator (GSO) [4,5] in the detection part and CsI(Tl) in the shielding part. Signals from the photomultiplier is fed to a charge sensitive pre-amplifier before reaching the PSD.

The pulse shape discriminator is composed of a shaping amplifier and a timing logic. In the shaping amplifier, the signal is differentiated and integrated to form the unipolar, bipolar and triplepolar pulses. The time interval between the first and second zero crossings in the triple polar pulse is measured by the timing logic circuits. Physically the PSD is composed of four hybrid IC's: three for the shaping amplifier (150mW/channel/IC) and one for the timing logic (200mW/channel). Sixteen PSD's and additional circuits for monitoring are arranged in two double-width NIM (Nuclear Instrumentation Module) modules.

A detector system consisting of 64 well-type phoswich counters (total area $\sim 740 cm^2$) and the PSD's was flown on board a balloon, setting a limit to the ^{57}Co line flux from SN1987A at around $10^{-4} cm^{-2} s$. The sensitivity for continuum flux was around a few $\times 10^{-6} cm^{-2} s^{-1} keV^{-1}$ between 100 and 200keV. In the paper, the circuit and the performance of the PSD will be presented. The well-type phoswich counter is described in a separate paper [1].

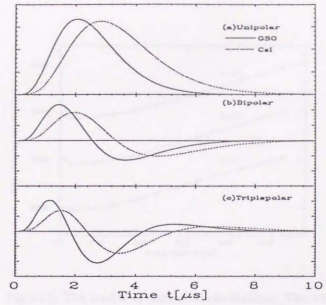

Figure 1: The wave forms of the shaping amplifier with a RC time constant of 500ns: (a)unipolar,(b)bipolar, and (c)triplepolar pulse. The GSO signal is shown by the solid line and the CsI signal by the dotted line.

II. Triple Polar Pulse Shaping

The triplepolar shaping is realized by adding one CR differentiation to a bipolar shaping amplifier. A triplepolar shaping amplifier needs 3 CR differentiation and N RC integration stages (CR^3-RC^N). In this shaping amplifier, the number of stages are CR^1-RC^4 for the unipolar, CR^2-RC^4 for the bipolar, and CR^3-RC^4 for the triple-polar pulses (See Fig. 1).

There are two zero cross points in the triplepolar waveform. The time interval between the first zero and second zero-crossing points depends on the rise time of the input pulse. The transfer function of the CR^3-RC^N pulse shaping amplifier is,

$$G(s) = \frac{s^3}{T^N(s+1/T)^{N+3}} \tag{1}$$

where T is the RC time constant of the shaping amplifier. The input to the PSD is a signal through a charge- sensitive pre-amplifier, and takes the following shape:

$$V_i(s) = \frac{Q}{\tau}\frac{1}{s+1/\tau}\frac{1}{sC_f} \tag{2}$$

where τ is the decay time constant of the input current pulse, which is the time constant of the scintillator. The signal at the output of the shaping amplifier in the PSD is given as,

$$\begin{aligned} V_o(s) &= V_i(s)G(s) \\ &= \frac{Q}{\tau}\frac{1}{s+1/\tau}\frac{1}{sC_f}\frac{s^3}{T^N(s+1/T)^{N+3}} \end{aligned} \tag{3}$$

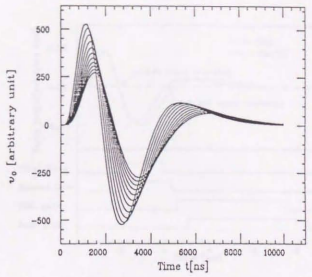

Figure 2: The calculated wave forms of triple-polar shaping. The waveform is shown as a function of t for τ=50ns, 150ns, 250ns, ..., 850ns, 950ns and 1050ns.

where Q is the total charge of the input signal. The inverse Laplace Transformation of V(s) is given as

$$\begin{aligned} v_o(t) &= \frac{Q}{C_f}\frac{1}{\tau T^N N!}\left\{\left(\frac{T}{\tau-T}\right)^2\left(\frac{\tau T}{\tau-T}\right)^{N+1}N! \right. \\ &\quad \times\left[e^{-t/\tau} - e^{-t/T}\sum_{r=0}^{N}\frac{\left(\frac{\tau-T}{\tau T}t\right)^r}{r!}\right] \\ &\quad +\frac{\tau}{T-\tau}t^{N+1}e^{-t/T}\left[\left(\frac{1}{N+1}-\frac{1}{N+2}\right)\frac{t}{T}\right. \\ &\quad \left.\left.+\frac{\tau-2T}{T-\tau}\frac{1}{N+1}\right]\right\} \end{aligned} \tag{4}$$

The results of numerical calculations is shown in Fig. 2. The intervals of the two zero crossings is shown as a function of τ in Fig. 3.

In general signals from the phoswich counter are mixture of two scintillator components. The output waveform of the shaping amplifier is,

$$v_o(Q,t) = v_o(Q_f,\tau_f,t) + v_o(Q_s,\tau_s,t) \tag{5}$$

where Q_f and Q_s are the fast and slow components of the input charge.

When there is only the fast component(Q_s=0), the interval becomes shortest, while there is only the slow component(Q_f=0), it is longest. When the two components are mixed, the interval is between the minimum and the maximum.

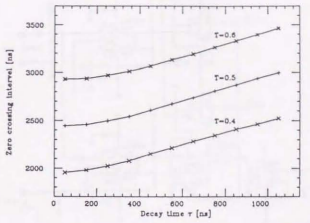

Figure 3: The results of numerical calculations. The interval between the two zero-crossings is shown as a function of τ for T=0.4μs,0.5μs and 0.6μs

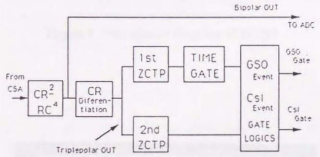

Figure 4: The block diagram of the PSD. CSA: a Charge Sensitive pre-Amplifier, ZCTP: Zero Cross Time Pick-off discriminators.

III. Pulse Shape Discrimination Circuit

Because of the large volume of the shielding crystal, the S/N ratio (the ratio of the clean hits on GSO(Ce) to all other hits) is expected to be very low. The circuit must select a small admixture of the faster scintillation light. The decay time of GSO(Ce) is about 60ns and decay time of CsI(Tl) is about 1μs.

The block diagram and the principle of operation of the PSD are shown in Figs 4 and 5.

The first zero crossing point is detected by the positive to negative zero cross time pick-off. The second zero crossing is detected by the negative to positive zero cross time pick-off. The lower level discriminator in the first time pick-off circuit defines the minimum energy accepted . If the signal exceeds the discriminator level, two logic gates are generated at the first zero crossing timing. If the second

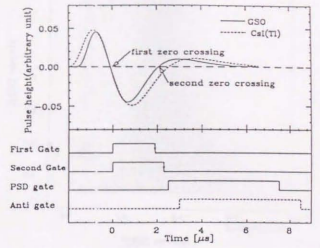

Figure 5: Principle of the pulse shape discriminator. The PSD pulse is issued only if the second zero crossing point falls in the first gate and the second gate.

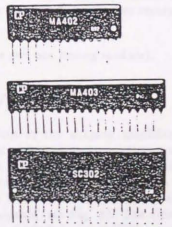

Figure 6: The photograph of PSD's hybrid IC's.

zero crossing points falls in between the two gates, the PSD system issues a pulse(the PSD gate) at the second zero crossing timing. If the second zero crossing points does not fall between the gates, the Anti gate is issued.

The shaping amplifier is composed three hybrid IC's (one MA402 and two MA403's)[6], and the timing logic composed one hybrid IC(SC302)[6]. (see Fig. 6)

The MA402 takes care of the amplification and the first CR differentiation stages. The first MA403 works as one RC^2 integrator, and the second MA403 as the other RC^2 integrator and the second CR differentiator.

The SC302 performs the third CR differentiation as well as the two zero crossing time pick-off. The circuit diagram of SC302 is given in Fig. 7. The power consumption is 150mW/channel /IC (450mW/channel) for the shaping amplifier and 200mW/channel for the timing logic.

Sixteen PSD's and additional circuits for monitoring are arranged in two double-width NIM modules(;one shaping

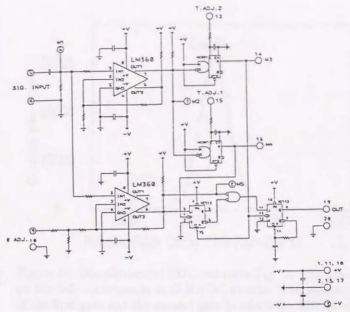

Figure 7: The circuit diagram of SC302

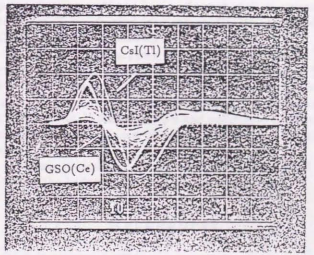

Figure 8: The wave form of the triplepolar pulse from GSO(Ce)/CsI(Tl) phoswich counter. The fast signals are from GSO(Ce) and the slow signals are from CsI(Tl).

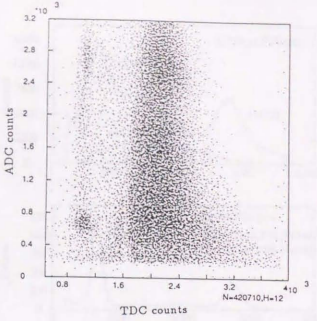

Figure 9: Distribution of ADC's and TDC's obtained by Welcome-1 when irradiated by ^{57}Co and ^{22}Na. The depletion of events along the time interval of 1.6μs is an artifact caused when the plot was taken in two separate runs.

amplifier module and one timing module).

IV. Performance

The time constant of the shaping amplifier was set at 0.5μs. The measured peaking time of the unipolar pulse was about 1.6μs: that means the actual RC time constant is 0.4μs. The measured time interval between the two zero crossing is about 2.2μs for the GSO(Ce) signals, and 2.6μs for the CsI(Tl) signals (see Fig. 8). The difference in the time intervals for GSO(Ce) and CsI(Tl) is around 0.4μs . The time interval of CsI(Tl) signals is nearly equal to the calculated result (see Fig. 3 T=0.4μs). For the GSO(Ce) signals it come out different, because the bandwidth of the amplifier was not wide enough.

The operation of the PSD was monitored by measuring the time interval between the two zero-crossings by TDC. Fig. 9 shows the 2-dim distribution for the TDC counts and the ADC counts produced by the 122keV line from ^{57}Co and the 511 keV line from ^{22}Na. In the plot, the band on the left corresponds to GSO(Ce) events and the band on the right is due to the events in which hard X-rays/γ-rays deposited most of their energy in the CsI(Tl) crystal. Fig. 10 is the projection of Fig. 9 onto the x-axis, on the distribution of the TDC counts.

The PSD performance is demonstrated in Fig. 11 where the energy spectra with and without the PSD gate are shown. By applying the PSD gate, the events in which the hard X-rays/γ-ray deposited a part or all of its energy in the shield are suppressed. In the figure, two peaks are clearly seen.

When the number of photo-electrons becomes low ($E \leq$

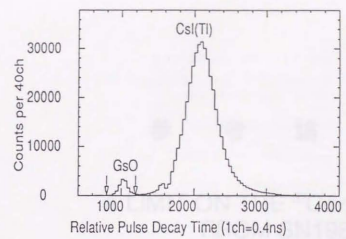

Figure 10: Distribution of TDC counts in Fig. 9. The peak on the left corresponds to GSO(Ce) events. The position of the first gate and the second gate to select the GSO(Ce) event are also shown.

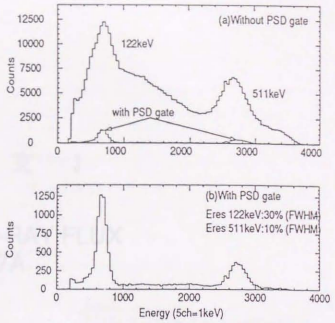

Figure 11: Energy spectra for ^{57}Co and ^{22}Na: (a) Without the PSD gate and with the PSD gate(lower curve); (b) the enlargement of the lower curve in (a).

50keV), the shape of CsI(Tl) pulses begins to fluctuate. If the pulse shape narrows significantly, they passes through the PSD filter. This seems to set the minimum detectable energy limit of the well-type phoswich counter.

V. Conclusion

The new pulse shape discriminator based on the triple-polar shaping method, has performed well in selecting the hard X-rays/γ-rays incident on GSO(Ce) crystal in GSO(Ce)/CsI(Tl) phoswich counter.

By the this PSD scheme, we significantly reduced the effect of the time slewing in the low energy region. The PSD is composed of four hybrid IC's, three for the shaping amplifier and one for the timing logic and consumes 650mW in total. Sixteen PSD's and additional circuits for monitoring are arranged in two double-width NIM modules.

We have successfully operated sixty-four channels of the PSD in the balloon-borne hard X-ray experiment.

References

[1] T.Kamae et al., This symposium.

[2] P.W.Nichlson, Nuclear Electronics, WILEY,1974,p233

[3] G.F.Knoll, Radiation Detection and Measurement second edition, WILEY, 1989, p646

[4] H.Ishibashi,K.Shimizu,K.Suwa,and S.Kubota, IEEE Trans. Nucl. Sci. **NS-36** (1989) 170

[5] H.Ishibashi, Nucl. Instr. and Meth. **A294** (1990) 271

[6] Made by Clear Pulse Co.,Ltd.

参　考　論　文　3

A LIMIT ON THE ^{57}Co γ-RAY FLUX FROM SN1987A

宮崎聡

THE ASTROPHYSICAL JOURNAL, 397:L83–L86, 1992 October 1

A LIMIT ON THE ^{57}Co GAMMA-RAY FLUX FROM SN 1987A

S. GUNJI, T. KAMAE, S. MIYAZAKI, Y. SEKIMOTO, T. TAKAHASHI, T. TAMURA, M. TANAKA, AND N. YAMAOKA
Department of Physics, University of Tokyo, Bunkyo-ku, Tokyo 113, Japan
T. YAMAGAMI
Institute of Space Astronautical Science, Sagamihara, Kanagawa 229, Japan
M. NOMACHI
National Laboratory for High Energy Physics (KEK), Tsukuba, Ibaraki 305, Japan
H. MURAKAMI
Department of Physics, Rikkyo University, Toshima-ku, Tokyo 171, Japan
AND
J. BRAGA AND J. A. NERI
Instituto Nacional de Pesquisas Espaciais, São Jose dos Campos, São Paulo, Brazil
Received 1992 March 30; accepted 1992 July 21

ABSTRACT

We studied the γ-ray flux from SN 1987A with a balloon-borne detector in Brazil on 1990 November 29. By comparing on- and off-source data, we obtained limits to the total γ-ray flux due to ^{57}Co decays and presumed pulsar activity. If the pulsar contribution is neglected, an upper limit (90% confidence limit) is set to the total ^{57}Co contribution above 60 keV at 2.7×10^{-4} cm^{-2} s^{-1} where the 122 keV line contribution is 1.0×10^{-4} cm^{-2} s^{-1}. The corresponding limit on the abundance ratio of ^{57}Co and ^{56}Co is 3.4 times that of the Sun. The present upper limit implies that the reported leveling off in the light curve of SN 1987A is primarily due to the pulsar activity. If the pulsar is Crab-like (photon index -2.2), the light curve requires an energy outflow greater than 0.95×10^{37} ergs s^{-1} (above 1 keV) now being supplied to SN 1987A by its presumed pulsar.

Subject headings: gamma rays: observations — nuclear reactions, nucleosynthesis, abundances — supernovae: individual (SN 1987A)

1. INTRODUCTION

Since the advent of SN 1987A, theoretical studies of the nucleosyntheses in supernovae and the chemical composition of supernova remnants have been deepened to higher accuracy and greater details (see, e.g., Nomoto et al. 1991a; Chevalier 1992). Observations on SN 1987A in several wavelength regions have allowed us to determine the abundance of some critical nuclides including ^{56}Ni. Analyses of observational data including the early turn-on of the γ-ray and X-ray fluxes have been interpreted as manifestations of the turbulent nature of the supernova explosion.

Among the multitude of nuclides produced in the supernova, the abundance of a few unstable nuclides with long-lived decay chains is of great interest since they are expected to become energy sources as time progresses. These nuclides are ^{56}Co ($\tau \sim 0.3$ yr), ^{57}Co ($\tau \sim 1.1$ yr), and ^{44}Ti ($\tau \sim 68$ yr). Among them ^{56}Co is the dominant energy source in the early life (4 months to 3 yr) of the supernova. In fact the bolometric light curve kept decaying monotonically until recently, in accordance with the lifetime of ^{56}Co (e.g., Nomoto et al. 1991a; Chevalier 1992). From the light curve, the amount of ^{56}Ni (the parent of ^{56}Co) produced in the supernova has been estimated at 0.073 $M_\odot$ (Nomoto et al. 1991b). Direct measurements of the line γ-ray fluxes due to the decay $^{56}\text{Co} \rightarrow {}^{56}\text{Fe}$ ($E = 847$ keV, 1238 keV) by the *Solar Maximum Mission* (Matz et al. 1988; Leising & Share 1990) and four balloon experiments (Mahoney et al. 1988; Sandie et al. 1988; Rester et al. 1989; Tueller et al. 1990) gave values consistent with the above estimate of the initial ^{56}Ni abundance. It is, however, the only nuclide among the three whose abundance has been determined to some accuracy.

Recently, CTIO (Cerro Tololo Inter-American Observatory) and ESO (European Southern Observatory) reported that the UVOIR light curves started to level off since $\sim$900 days after the explosion (Bouchet, Danziger, & Lucy 1991; Suntzeff et al. 1991). Such a change has been expected to occur when either ^{57}Co, ^{44}Ti, or the presumed pulsar activity becomes an appreciable energy source.

The theoretically expected abundance of ^{44}Ti falls short of being of any significance at this stage of the supernova's life (e.g., Nomoto et al. 1991a; Woosley & Hoffman 1991). Observations in the mid-IR made by Danziger (1991) suggest that the abundance ratio of ^{57}Co to ^{56}Co cannot be significantly higher than that in the Sun $\langle {}^{57}\text{Co}/{}^{56}\text{Co}\rangle^1 = 1.5$. No X-ray flux has been detected since around day 800 after the explosion (Inoue et al. 1991; Sunyaev et al. 1990). Sunyaev et al. (1990) calculated an upper limit to the pulsar luminosity in the energy band between 1 and 1000 keV: $L_{>1\,\mathrm{keV}} < 4.4 \times 10^{38}$ ergs s^{-1} for photon index 2.1 for day 830. This is, however, not inconsistent with the UVOIR light curve measured by CTIO and ESO. Woosley & Hoffman (1991) concluded from a theoretical study of explosive silicon burning that $\langle {}^{57}\text{Co}/{}^{56}\text{Co}\rangle$ is likely to be between 0.5 and 2.5.

The current status calls for direct measurements on the two possible gamma-ray sources. The observation was carried out

[1] $\langle {}^{57}\text{Co}/{}^{56}\text{Co}\rangle$ is the abundance ratio of the $A = 57$ and $A = 56$ isotopes in the $\text{Ni} \rightarrow \text{Co} \rightarrow \text{Fe}$ decay chain normalized to that in the Sun: $\langle {}^{57}\text{Co}/{}^{56}\text{Co}\rangle \equiv [X({}^{57}\text{Ni})/X({}^{56}\text{Ni})]/[X({}^{57}\text{Fe})/X({}^{56}\text{Fe})]_\odot$.

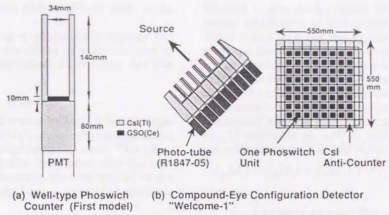

FIG. 1.—Schematic drawings of one well-type phoswich counter unit (*a*) and the Welcome 1 detector (*b*)

on 1990 November 29 (local time, day 1375 after the outburst) in the area around São Paulo, Brazil, for about 160 minutes with our hard X-ray/γ-ray detector aboard a stratospheric balloon.

2. DETECTOR

The detector system used in the observation consists of 64 "well-type" phoswich counters (Kamae et al. 1992; Murakami et al. 1992) and 36 anticounters (Fig. 1). This detector system will be referred to as Welcome 1.

The well-type phoswich counter is made of a small inorganic scintillator with a fast decay time (the detection part) glued to the interior bottom surface of a well-shaped block of another inorganic scintillator with a slow decay time (the shielding part). The well-shaped shielding part acts as an active collimator as well as an active shield. The whole assembly is viewed by a phototube from the exterior bottom surface of the shielding part (Kamae et al. 1992). By using an appropriate pulse-shape discriminator (PSD), hard X-rays/gamma-rays that have deposited energy only in the detection part can be selected.

The present counter is the first model of the well-type phoswich counter and uses a new scintillator Gd_2SiO_5 doped with Ce(0.5%) (GSO) for the detection part (Takagi & Fukazawa 1983; Ishibashi et al. 1989), and CsI(*Tl*) for the shielding part. The characteristics of the detector are summarized in Table 1.

Since the well-type phoswich counter integrates the shielding and collimation parts and facilitates finer active collimation, it not only reduces external background but also provides the instrument with a nearly 4π anticounter for the internal β-γ background (Kamae et al. 1992). Its simple shape and reduced count rate allow units to be assembled in a compound-eye configuration (Fig. 1*b*). Here each unit is surrounded by eight neighbors which can be used as additional active shields. The observed off-source count rate (after the event selection described below) and the internal background rate (the rate due to radioactivity in GSO crystals) of Welcome 1 are shown in Figure 2 with a Monte Carlo estimation of the external background rate (the rate due to external sources). The measured S/N ratio for the Crab nebula is about 1.2/1.0 in the energy range between 100 and 200 keV: should the atmospheric attenuation (1/2.5 at 4 g cm^{-2}) have not existed, the S/N would have reached 3/1.

TABLE 1

CHARACTERISTICS OF WELCOME-1

Characteristic	Value
Energy range	60–800 keV
Energy resolution (FWHM)	28% at 122 keV, 12% at 511 keV
Geometrical area	740 cm^2
Full peak efficiency	98 at 122 keV, 30% at 511 keV
Background rate	1.5×10^{-4} cm^{-2} s^{-1} keV^{-1} at 122 keV
Pointing	Elevation: fixed Azimuth: $\sim \pm 1°$
Aperture (HWHM)	7:7 at 122 keV; 9:1 at 511 keV

3. OBSERVATION

Welcome 1 was flown from the Instituto Nacional de Pesquisas Espaciais (INPE) balloon base in Cachoeira Paulista, in the state of São Paulo, Brazil, (45°00'34" *W*, 22°39'44" *S*) on 1990 November 29 (local time, 1375 days after the explosion of SN 1987A). The detector reached ceiling altitude of 37.7 km (4 g cm^{-2}). The observation of SN 1987A started at 1:00 A.M., 1990 November 30 (local time). On-source and off-source observations were alternated at an interval of ~20 minutes. In total we observed SN 1987A (on-source) for about 85 minutes and background (off-source) for about 75 minutes. During the observation, the detector was set at a fixed elevation angle (43°), and its azimuth angle was adjusted to follow the direction of SN 1987A approximately every 10 minutes. During the

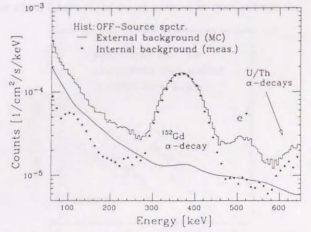

FIG. 2.—Observed off-source spectrum (*histogram*), the measured internal background (*filled circles*), and the Monte Carlo simulated external background (*solid line*). Broad peaks at around 368 and 511 keV are due to ^{152}Gd α-decays (2.14 MeV) in GSO and to e^+ annihilations, respectively.

background run, the detector was pointed 20°–30° away to the east or west of SN 1987A.

Pointing was done by using a geomagnetic sensor. The direction of the detector was monitored by a star camera to about ±0°02. During the observation, all counters but one operated normally.

4. DATA ANALYSIS

In data analysis we rejected events within 1.5 ms of large-energy-depositing events (≥ 50 MeV, mostly charged particles) in the same counter or in a neighboring counter. This effectively eliminated unwanted baseline fluctuation after the incidence of high-energy charged particles. We then rejected events with one or more hits in the neighboring counters to eliminate Compton-scattered γ-rays.

As the result of the above event selection, the total on-source and off-source live times were reduced to 3397 and 2997 s for 23 counters (efficiency of about 66.6%). The spectrum after the event selection was well reproduced by the measured internal background due to radioactive contamination in the detection part (GSO) and simulated atmospheric and celestial diffuse background with the energy dependence given by Gehrels (1985).

The overall gain and the live time were calibrated for every counter by using the broad peak at around 368 keV (Fig. 2) due to α-decays of ^{152}Gd in GSO (E_α = 2.14 MeV, rate = 0.167 Hz/counter). To follow the time variation at fine steps and yet to keep high statistical accuracy, the ^{152}Gd α-decays were integrated for 90 minutes centered around time bins set at 5 minute steps. This procedure eliminated overcompensation of statistical fluctuations by gain adjustment. The resultant time variation of the overall gain is consistent with what is expected from the temperature variation recorded during the observation.

The four sets of on- and off-source spectra were then normalized according to the effective live time and the effective area, and then four on-off subtractions are made: the results do not show any significant deviation from zero when integrated over the detector energy resolution. The electronically measured effective live times for on and off observation were in accord with those estimated from the total numbers of the ^{152}Gd α-decays counted. Finally the four on-off spectra were summed to give the histogram shown in Figure 3*a*. The statistical significance of data points are shown in Figure 3*b*. When folded with the energy resolution, we do not see any deviation greater than 1.3 σ up to 400 keV.

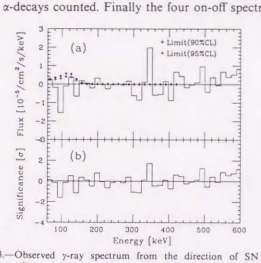

FIG. 3.—Observed γ-ray spectrum from the direction of SN 1987A: (*a*) Difference between the on-source and the off-source spectra (effective time 3397 s, effective area 592 cm^2); (*b*) Statistical significance of data points. The crosses and the filled circles are the 90% and 95% CL upper limits, respectively.

The nonobservance of any line feature in our data has led us to set upper limits on the ^{57}Co γ-ray flux and the pulsar energy outflow from SN 1987A. We assume here that there are two γ-ray sources of a fixed flux amount, ^{56}Co of 0.073 $M_\odot$ as determined from the early light curve, and ^{44}Ti of 9.2 × 10^{-5} $M_\odot$ (Nomoto et al. 1991b), and two γ-ray sources of an unknown amount ^{57}Co, and pulsar activity:

$$f_{\rm obs}(E_\gamma) = f_{56}(E_\gamma) + f_{44}(E_\gamma) + N_1 f_{57}(E_\gamma) + N_2 f_{\rm pulsar}(E_\gamma) , \quad (1)$$

where

$f_{\rm obs}(E_\gamma)$: Observed γ-ray flux ,

$f_{56}(E_\gamma)$: ^{56}Co γ-ray flux for ^{56}Co = 0.073 $M_\odot$,

$f_{44}(E_\gamma)$: ^{44}Ti γ-ray flux for ^{44}Ti = 9.2 × 10^{-5} $M_\odot$,

$f_{57}(E_\gamma)$: ^{57}Co γ-ray flux for $\langle ^{57}{\rm Co}/^{56}{\rm Co}\rangle = 1$,

$f_{\rm pulsar}(E_\gamma)$: pulsar γ-ray flux for the energy outflow 10^{38} ergs s^{-1} (photon index = −2.2 assumed) ,

E_γ: γ-ray energy ,

N_1, N_2: Normalization factors .

The functions f_{56}, f_{44}, f_{57}, and $f_{\rm pulsar}$ are numerically supplied by S. Kumagai (1992, private communication; the same functions have been used in Kumagai et al. 1989, and we take the distance to SN 1987A to be 55 kpc) at the abundances or intensity listed above. These numerical functions were calculated using Model 14E1 of Shigeyama & Nomoto (1990).

Chi-square is calculated for the data shown in Figure 3*a* by assuming the form given in equation (1) for various normalization factors. The sets of points (N_1, N_2) where the confidence level (CL) reaches 68.3%, 90%, or 95% form three lines shown in Figure 4. The two superposed curves in Figure 3*a* correspond to the 90% CL upper limit (N_1 = 3.4, N_2 = 0) and the 95% CL upper limits (N_1 = 4.8, N_2 = 0). The 90% CL upper limit (N_1 = 3.4, N_2 = 0) corresponds to the ^{57}Co 122 keV line flux of 1.0 × 10^{-4} cm^{-2} s^{-1}. The 90% CL upper limit (N_1 = 0, N_2 = 2.3), on the other hand, corresponds to a Crab-like pulsar with energy outflow of $L_{>1\,\rm keV}$ = 2.3 × 10^{38} ergs s^{-1} or about 2.3 times the energy emitted by the Crab nebula.

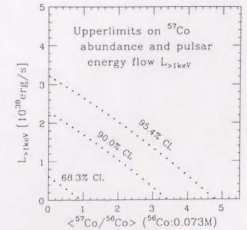

FIG. 4.—Upper limits at 68.3%, 90.0%, and 95.4% CL for the ^{57}Co abundance and the pulsar energy outflow.

5. CONCLUSIONS

Several theoretical analyses have already been made on the measured light curve (Kumagai et al. 1991 and Suntzeff et al. 1991). According to Kumagai et al. (1991), $\langle {}^{57}\mathrm{Co}/{}^{56}\mathrm{Co}\rangle$ needs to be greater than 20 to reproduce the ESO light curve if the energy is supplied only by the ^{57}Co decay. They determined that $\langle {}^{57}\mathrm{Co}/{}^{56}\mathrm{Co}\rangle$ between 5 and 10 is required if the CTIO light curve is to be reproduced by the ^{57}Co decay. Suntzeff et al. (1991) fitted the CTIO data up to day 1600 and concluded that $\langle {}^{57}\mathrm{Co}/{}^{56}\mathrm{Co}\rangle$ is 5 ± 1.

In the present study, an upper limit (90% CL) is set to the total ^{57}Co γ-ray flux above 60 keV at 2.7×10^{-4} cm^{-2} s^{-1} where the 122 keV line contribution is 1.0×10^{-4} cm^{-2} s^{-1}. The corresponding limit on the $\langle {}^{57}\mathrm{Co}/{}^{56}\mathrm{Co}\rangle$ is 3.4 and somewhat inconsistent with $\langle {}^{57}\mathrm{Co}/{}^{56}\mathrm{Co}\rangle = 5 \pm 1$ obtained by Suntzeff et al. (1991). Our limit implies, instead, that the major energy source of the present SN 1987A is not ^{57}Co decays but probably pulsar activity. If the ESO data around 950–1350 days are combined with the present upper limit, the energy flow out of the presumed Crab-like pulsar is calculated at $L_{>1\,\mathrm{keV}} \sim (0.91, 0.87, \text{or } 0.80) \times 10^{38}$ ergs s^{-1} in addition to that supplied by ^{56,57}Co decays with $\langle {}^{57}\mathrm{Co}/{}^{56}\mathrm{Co}\rangle$ of 1.0, 1.7, or 3.4, respectively. If the CTIO light curve around day 900–1450 is taken, the energy flow of the presumed pulsar is $L_{>1\,\mathrm{keV}} \sim (1.50, 1.35, \text{or } 0.95) \times 10^{37}$ ergs s^{-1} in addition to that supplied by ^{56,57}Co decays with $\langle {}^{57}\mathrm{Co}/{}^{56}\mathrm{Co}\rangle$ of 1.0, 1.7, and 3.4, respectively.

This work has been carried out under support of Grant-in-Aid by Ministry of Education, Culture and Science (Monbusho) of Japan. The authors wish to thank Professors J. Nishimura, M. Oda, K. Kikuchi, Y. Tanaka, F. Makino, N. Yajima, K. Sato, and K. Nomoto on the Japanese side, and the INPE directorate and the Government of Brazil on the Brazilian side for advice and assistance that made this Brazilian-Japanese collaboration a success. Special thanks are due to V. W. J. H. Kirchhoff who supervised the project in Brazil and to the INPE and ISAS balloon groups who cooperated in the successful launch. We owe Professor K. Nomoto and S. Kumagai thanks for the theoretical γ-ray spectra used in the fitting.

REFERENCES

Bouchet, I. J., Danziger, I. J., & Lucy, L. B. 1991, AJ, 102, 1135
Chevalier, R. A. 1992, Nature, 355, 691
Danziger, I. J. 1991, Supernovae, ed. S. E. Woosley (Berlin: Springer), 69
Gehrels, N. 1985, Nucl. Instr. Method, A239, 324
Inoue, H., et al. 1991, PASJ, 43, 213
Ishibashi, H., et al. 1989, IEEE Trans. Nucl. Sci., NS-36, 170
Kamae, T., et al. 1992, IEEE Trans. Nucl. Sci., submitted
Kumagai, S., et al. 1989, ApJ, 345, 412
Kumagai, S., et al. 1991, A&A, 243, L13
Leising, M. D., & Share, G. H. 1990, ApJ, 357, 638
Mahoney, W. A., et al. 1988, ApJ, 334, L81
Matz, S. M., et al. 1988, Nature, 331, 416
Murakami, H., et al. 1992, IEEE Trans. Nucl. Sci., submitted
Nomoto, K., et al. 1991a, Supernovae and Stellar Evolution (Singapore: World Scientific)
Nomoto, K., et al. 1991b, Supernovae, ed. S. E. Woosley (Berlin: Springer), 176
Rester, A. C., et al. 1989, ApJ, 342, L71
Sandie, W. G., et al. 1988, ApJ, 334, L91
Shigeyama, T., & Nomoto, K. 1990, ApJ, 360, 242
Suntzeff, M. B., et al. 1991, AJ, 102, 1118
Sunyaev, R., et al. 1990, Soviet Astron. Lett., 16, 403
Takagi, K., & Fukazawa, T. 1983, Appl. Phys. Lett., 42, 43
Tueller, J., et al. 1990, ApJ, 351, L41
Woosley, S. E., & Hoffman, R. D. 1991, ApJ, 368, L31

参　考　論　文 4

Newly Developed Low Background Hard X-ray/Gamma-ray
Telescope with the Well-type Phoswich Counter

宮崎聡

Newly Developed Low Background Hard X-ray/Gamma-ray Telescope with the Well-type Phoswich Counters

T. Takahashi, S. Gunji, M. Hirayama, T. Kamae, S. Miyazaki,
Y. Sekimoto, T. Tamura, M. Tanaka, and N.Y. Yamasaki
Dept. of Physics, University of Tokyo, Bunkyo-ku, Tokyo, JAPAN 113
T. Yamagami,
Inst. of Space Astronautical Science, Yoshinodai, Sagamihara, Kanagawa, JAPAN 229
M. Nomachi,
Nat. Lab. for High Energy Physics (KEK), Tsukuba, Ibaraki, JAPAN 305
H. Murakami,
Dept. of Physics, Rikkyo University, Toshima-ku, Tokyo, JAPAN 171

Abstract

We have developed a low background hard X-ray/gamma-ray telescope (Welcome-1) for balloon-borne experiments in the energy range from 40 keV to 800-1000 keV. The detector is based on newly developed well-type phoswich counters. In the first well-type phoswich counter, GSO(Ce) (Gd_2SiO_5 doped with Ce) is used as the detection part and CsI(Tl) as the shielding part. Welcome-1 consists of 64 GSO/CsI well-type phoswich counters assembled in the "compound-eye" configuration and the effective area is 740 cm^2 at 122 keV and 222 cm^2 at 511 keV line. The well-type phoswich counter and the compound eye configuration reduces background significantly both external and internal and allows us a high signal-to-noise ratio in balloon-borne experiments.

The data from the detector is taken by the versatile data acquisition system based on the VME computer specially designed for balloon-borne experiments. In the system, the arrival time of each event is recorded by the clock system which utilizes GPS satellite.

The background levels at an altitude of 4.5g/cm^2 are 1×10^{-4}/cm^2/s/keV at 122 keV. Crab nebula has been observed with the signal to background ratio better than unity between 100 and 200 keV. In this paper, the desine of the telescope and the flight performace are presented.

I. Introduction

The precise measurements of hard X-rays and γ-rays from astronomical sources are very important. Hard X-rays/γ-rays is a unique probe to understand nuclear processes in the supernova remnants or the mechanism of the non-thermal emission from pulsars, black hole candidates, and AGN's. To extend knowledge obtained in the previous soft X-ray satellite missions such as the Ginga satellite, observations of low flux sources at a level of 10^{-6}~10^{-7}/cm^2/s/keV will be required in the energy range from a few 10 keV to a few MeV.

In these energy range, however, the signal from the object is weak compared with the background. In most cases the signal is extracted by subtracting the off-source data from on-source data. The sensitivity of a celestial hard X-ray/γ-ray telescope has been limited by its signal to noise ratio in the on-source data. In order to detect the emission of hard X-rays/γ-rays at the required level, one needs a detector which can realize very low background rate with appropriate detector size.

In order to fulfill the above requirements and to achieve the high sensitivity even in the limited observation time of balloon-borne experiments, we have developed a well-type phoswich counter [1]. Using the first prototype of the well-type phoswich counter, we developed a balloon-borne telescope, "Welcome-1", for the observations in the energy range from 40keV to 800keV. Primary scientific aim was to detect the ^{57}Co line γ-rays (122 keV) from SN1987A[2]. The detector was flown successfully from Brazil in 1990. Subsequent observations were performed for Cen-A, PSR1509-58 and GX339-4 in 1991[3, 4]. In this paper, we summarize the description and the flight performance of the telescope.

II. Welcome-1 Telescope

A. *Overview*

Figure 1 shows the schematic view of the Welcome-1 telescope. The hard X-ray/γ-ray detector is stored in an Al-honeycomb box and the box is attached to a gondola by two bearings which allows changes in the elevation angle of the detector. Electronics system, telecommunication equipments and batteries are mounted inside the gondola. On the top of the gondola, a torque motor is attached. The whole instrument is suspended by the straps through the motor axis.

During the flight, the source pointing is carried out by the combination of elevation control of the detector and

Energy range	40 keV – 800 keV
Type	64 well-type phoswich counters
	detection part:
	GSO 3.4×3.4×1.0cm^3
	shielding/collimation part:
	CsI(Tl) 8×8 matrix config.
	36 CsI anti counters
Total area	740 cm^2
Full peak efficiency	100 % at < 200 keV
	30 % at 511 keV
Energy resolution	28 % at 122 keV
	12 % at 511 keV
Aperture	± 7.4°
Time resolution	32 μsec
Weight	680kg

Table 1: Characteristics of the Welcome-1 telescope

azimuth control of the gondola. The elevation angle is controlled by a ball screw drive located on the gondola. The azimuth pointing and rotation are achieved by "Yorimodoshi" method , in which a magneto-meter on the gondola and the torque motor forms the stabilization system. We monitor the pointing accuracy with a geomagnetic sensor, a sun camera, and a star camera.

Table 1 summarizes the basic characteristics of the Welcome-1 detector.

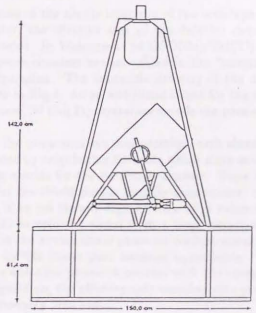

Figure 1: The schematic drawing of the Welcome-1 detector and the gondola

B. *Well-type Phoswich Counter*

In the well-type phoswich counter, a small inorganic scintillator with a fast decay time (the detection part) is glued

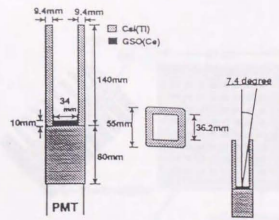

Figure 2: A unit of the first prototype well-type phoswich counter.

to the interior bottom surface of a rectangular well-shaped block of another inorganic scintillator with a slower decay time (the shielding part)as shown in Fig. 2. The whole assembly is viewed by a photomultiplier from the exterior bottom surface of the shielding part. By using a specially designed pulse-shape discriminator (PSD), hard X-rays/gamma-rays that has deposited energy only in the detection part can be selected.

The well-type phoswich counter differs from the conventional phoswich counter in that it has a long protruded collimation part. This well-shaped shielding part acts as an active collimator as well as an active shield. It defines the field of view of the counter. In order to minimize the X-rays from the aperture, mainly by the diffuse component and atmospheric background, the longer well, thus the narrower field of view will be used.

The active shield/collimator reduces the background events which are caused by γ-rays from the off-aperture and/or charged particles penetrating through the detection part. In addition, γ-rays from $\beta-\gamma$ decays of unstable isotope, which are produced in the detector volume, are able to be detected effectively by the shield surrounding the detection part almost in 4 π str.

In the first well-type phoswich counter, GSO(Ce) (Gd_2SiO_5 doped by Ce) is used as the detection part and CsI(Tl) is used as the shielding part. The size of the GSO crystal placed in the well is 3.4 × 3.4 × 1.0 cm^3. The shielding part consists of the collimation part of 0.94 cm thick and 14 cm long and the the bottom shield of 5.5 × 5.5 × 8.0 cm^3. The counter is viewed by a single 2-inch photomultiplier (HAMAMATU R1847-05). GSO(Ce) is newly developed inorganic scintillator [5]. When GSO(Ce) is used as a detection part in the phoswich counter, its merits are :(1) the scintillation light decays much faster (60ns) than widely used inorganic scintillators (the decay time of CsI(Tl) is 1μs); (2) the light yield is reasonably high; (3) the attenuation coefficient for γ-ray is large. For example, the full peak efficiency of 1 cm thick GSO(Ce) and NaI(Tl) at 511 keV is 30 % and 10 %, respectively.

The energy resolution of GSO scintillator (3.4 × 3.4 ×

1.0 cm^3) is measured to be 19.4% at 122 keV and 8.4% at 511 keV γ-rays. The light from GSO in the well , however, is attenuated to 50-60% when traversing the shielding part (8cm of CsI). The energy resolution of 28% at 122 keV and 12% at 511 keV γ-rays are achieved for the well-type phoswich counter. Fig.3 shows the energy spectrum of GSO scintillator in the CsI(Tl) well for ^{57}Co, ^{22}Na and ^{137}Cs radio active sources. The signal from GSO is selected out by means of the PSD described later.

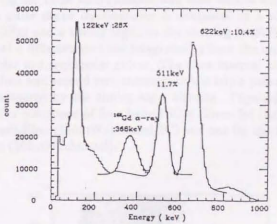

Figure 3: Energy resolution of the GSO scintillator in the well-type phoswich configuration

C. *Compound Eye Configuration*

Because of the simple structure of the well-type phoswich counter, the effective area of the detector can be easily expanded. In Welcome-1, 64 GSO(Ce)/CsI(Tl) well-type phoswich counters are assembled in the "compound-eye" configuration. The schematic drawing of the detector is shown in Fig.4. As an additional shield for the outermost counters, 36 CsI(Tl) crystal surrounds the phoswich counters.

In the compound eye configuration, each element is surrounded by neighboring elements which serve as additional active shields for the particular element. Since the count rate of the shield part is roughly proportional to its volume, if we use the anti-signal from a large volume of shield crystal to veto the signal from a large detection part as seen in the conventional phoswich configuration, the dead time by the shield part becomes appreciable. Whereas, in the well-type phoswich counter with the compound eye configuration, the effective anti-counting rate per element is reasonably kept low.

The effective area of the detection part of Welcome-1 is 740cm^2 for 122 keV line and 222cm^2 for 511keV line. The field of view (FOV) of the detector is determined by the detection efficiency of the protruded part of the well. The angular acceptance was measured by ^{57}Co (122 keV) and ^{22}Na (511 keV). Fig.5 shows the results of the experiments and the comparison with the MonteCarlo calculation. By fitting the data, the angular acceptance (HWHM) was calculated to be 7.7$\pm$0.1° at 122 keV and 9.1$\pm$0.2° at 511 keV.

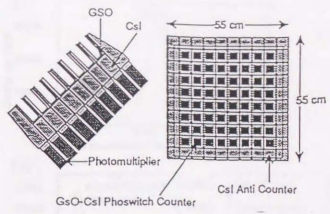

Figure 4: The first detector system based on the well-type phoswich counters. The whole detector system consisting of 8×8 well-type phoswich counters and 36 dedicated shielding counters.

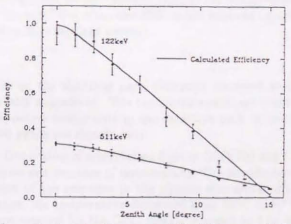

Figure 5: Angular Response of the Welcome-1 Detector

D. *Electronic System*

The electronic system of the telescope for a balloon-borne experiment is the most difficult part because of its operating environment. We must ensure the proper operation even at an altitude of 40 km where the atmospheric pressure is 4mb and thus the operating temperature of the circuit reaches 60-70 degree. The electronic system for the Welcome-1 is specially designed to process data from many channels under nominal constraints for space experiments: low power consumption, high reliability and compactness[7].

1) *Electronics for Phoswich Counters:* Because of the large volume of the shielding crystal, the S/N ratio (the ratio of the clean hits on GSO(Ce) to all other hits) is expected to be very low. The circuit must select a small

admixture of the faster scintillation light. This circuit, pulse shape discriminator (PSD), is thus critical for the successful operation of the phoswich counter. The circuit must be simple and consume as little power as possible, because we have to operate a large number of channels within limited power consumption.

In order to satisfy these conditions, a new PSD circuit was developed[6]. In the present system, signal from the photomultiplier is first fed to charge sensitive pre- amplifier having the 16 μs time constant and then sent to the PSD. The pulse shape discriminator is composed of a shaping amplifier and a timing logic. In the shaping amplifier, the signal is differentiated and integrated to form the unipolar, bipolar and triplepolar pulses. The time interval between the first and second zero crossings in the triple polar pulse is measured by the timing logic circuits. Physically the PSD is composed of four hybrid IC's: three for the shaping amplifier (150mW/channel/IC) and one for the timing logic (200mW/channel).

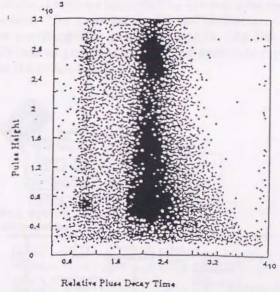

Figure 6: Distribution of ADC's and TDC's obtained by Welcome-1 when it is irradiated by ^{57}Co and ^{22}Na.

The operation of the PSD was monitored by measuring the time interval between the two zero-crossings by TDC. Fig. 6 shows the 2-dim distribution for the TDC counts and the ADC counts produced by the 122keV line from ^{57}Co and the 511 keV line from ^{22}Na. In the plot, the band on the left corresponds to GSO(Ce) events and the band on the right is due to the events in which hard X-rays/γ-rays deposited most of their energy in the CsI(Tl) crystal.

Figure 7(a) is the projection of Fig.6 onto x-axis and shows the distribution of the TDC counts. The interval between GSO band and CsI band is about 450 ns. The PSD performance is demonstrated in Fig. 7(b) where the energy spectra with and without PSD gate are shown. By selecting events in the left band by PSD gate in Fig.6,

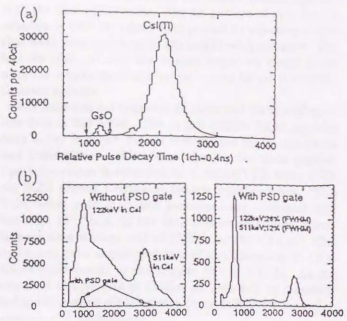

Figure 7: (a) The timing spectrum, a peak on the left corresponds to GSO events, and (b) the energy spectra for ^{57}Co and ^{22}Na when the PSD is not required (upper) and when it is required (lower).

hits on the shielding part, Compton scattered events are greatly suppressed. The remaining events are those which deposited energy only in the detection part. In the figure, two peaks are clearly seen.

Decay time of scintillation light in GSO(Ce) and CsI(Tl) varies as a function of temperature. The temperature variation of the response in the circuits also affects the pulse shape. As temperature decreased from 30°C to 10°C, the time interval for the GSO signals changed by 6 ns and for the CsI signals by 15 ns.

Analog output from the shaping amplifier in the PSD is split into two paths: one goes to the logic and the other to ADC. The outputs of four neighboring PSD's are ORed for triggering, forming 16 trigger lines in total for the well-type phoswich counters. The signals from active anti CsI(Tl) crystals are summed in analog sum units and sent to the discriminators. Because of the limitation of the space and the electric power, sixteen PSD channels are monitored by TDC in flight.

When there is a large energy deposit (at least E$\geq$60 MeV) in CsI(Tl) crystal, CsI(Tl) generates the train of pulses with random shape during 400μs - a few ms. When the pulse shape is similar to the pulse shape of GSO accidentally, PSD misbehaves and generates the consecutive train of triggers. In order to prevent these fake triggers, we incorporate a discriminator in the preamplifier that sense the period until the amplifier baseline is restored after large-energy-depositing events.

2) *Online System:* In Welcome-1, each element is arranged electronically so that each element acts as an active shield to the neighboring ones. There are 64 PSD signals and 36 anti signals to be processed in the system. The fast and versatile online system is needed to operate many independent channels of Welcome-1 properly. The online system consists of two sub-systems, one is to acquire data from the detector and the other from the star camera. The block diagram of the online system is shown in Fig. 8. Each sub-system is controlled by its own 32bit microprocessor through VME (Versa Module Europe) bus. Since the VME standard is a widely used standard for real-time operation in industry, the design technique of the circuit has been established and also many kinds of modules are commercially available. It supports 32 bit access for both addressing and data transfer and facilitates design of a high speed online system. The microprocessor is MC68000 CMOS CPU operated at 10 MHz. The CPU is operated on the software stored in the PROM. Controlling and processing of data is done by a set of interrelated processes and interrupt routines controlled by the real time operating system. The operating modes and parameters in the system are changed by ground commands. The Data I/O module receives ground commands and issues interrupt signals to the microprocessor.

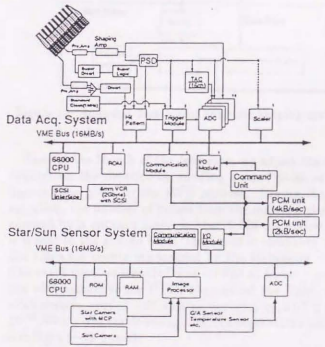

Figure 8: Schematic drawing of the online system. Upper part of the figure shows the data acquisition subsystem and the lower part of the figure shows the star camera subsystem.

In the data acquisition system, when a trigger signal is generated from one counter, the ADC's in the particular group of four, the hit-pattern of the lower discriminator, and the hit-pattern of the upper discriminator in the preamp's are recorded by the online system together with the time of the event. The hit pattern of neighboring counters is used to reduce background by rejecting events that have been scattered in the neighboring counters. The fact we read out only the nearest neighbors serves to reduce the overall dead time as well as the failure rate of the detector system.

The data size per trigger is 34 bytes and the size of monitor data is 216 bytes. The 512kB CMOS RAM provides data buffer in which data is reformatted for the recording and transmission. The data taken by the data acquisition sub-system is recorded on a EXABYTE 8mm VCR via SCSI (Small Computer System Interface) bus. This VCR holds upto 2GB and provides error correction rate less than 10^{-13}bits. In our data acquisition system, a continuous data storage rate of 82kB/s can be achieved. The maximum data acquisition rate of this system is 51 kB/s which corresponds to the trigger rate of 1.5kHz. At the expected trigger rate of 150Hz, all data will be transmitted to the ground via telemetry (max 4kB/s) for the online analysis and monitoring.

We use a star camera and a sun camera to monitor and to guide the direction of the telescope. The cameras are mounted on the housing of the detector units. The star camera is a MCP (micro channel plate) coupled to a CCD camera and image stars the sky. Its field of view is 9.1×6.3 degrees and identifies stars of magnitude ~8.1 . Wheres, the sun camera is a normal CCD camera with a wide field lens of 60°×60°. In the star/sun camera subsystem, the image on the CCD camera (512×512 pixels) is digitized by the image processing board on the VME bus. The microprocessor selects the bright points and then transmits brightness and position of each point to the ground through the telemetry (max 2kB/s). On the ground station the star image is reconstructed every 2 seconds by using a workstation. The star image near SN1987A region is shown in Fig.9

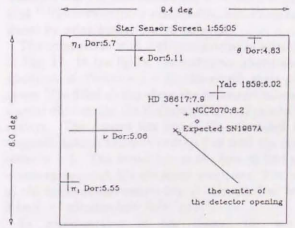

Figure 9: Reconstructed star image taken by the star camera. The field of view of the image is 6.0°×9.4°.

3) *Absolute Time Keeping System:* For observations of pulsars, a clock system which is highly stabilized

in its frequency and precisely calibrated against UTC is needed. It is required to record the absolute arrival time of events, when we try to compare the results with other experiments done at a different epoch. The time of X-ray/γ-ray incidence is recorded by making reference to the onboard quartz clock to 32 μs resolution with the frequency stability of $\Delta f/f \sim 10^{-10}$ for 10^8s.

Figure 10 shows the block diagram of the time keeping system. On the ground, the master clock system backed up by GPS satellites is settled. The system consists of a GPS receiver and a Rubidium clock. The GPS receiver receives signals from more than three GPS satellites and generates 1Hz clock signal which is used as the standard signal with reference to the UTC. The Rubidium clock has the frequency stability of $\Delta f/f \sim 10^{-11}$ for 10^5 s and its frequency is calibrated by using the 1Hz signal from the GPS receiver.

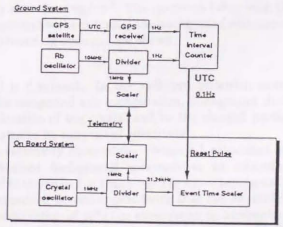

Figure 10: Scematic diagram of the time keeping system

Prior to the launch of the telescope, we adjust the time counter on the detector by sending a reset pulse at the known time given by the GPS receiver. During the observation, the number of pulses from the onboard clock is counted by a onboard scaler in the 15.625 ms period and it is sent to the ground base. The count is compared with the reference counts maintained by the Rubidium clock. The event time we recorded was verified to be accurate to 2μs with respect to the UTC. Throughout the flights, our clock system worked well with an accuracy of $\Delta f/f < 3 \times 10^{-9}$, which was stable enough for the observation time in one flight (~12 hours).

4) *Power Supply and Power Consumption:* The total power consumption of the data acquisition and star systems are about 220 W. With this power consumption, the entire system can be operated for 24 hours. Lithium batteries were used for the power supply on the ceiling. The voltage of one battery is 3.95 V and has 30Ah of capacity.

III. Balloon-borne Experiments

We have carried out a series of balloon-borne experiments in Brazil in the past three years to observe astronomical objects in the southern hemisphere. Welcome-1 was flown from INPE balloon base in Cachoeira Paulista, in the state of Sao Paulo, in Brazil (45.00'34"W, 22.39'44"S, cutoff rigidity ~ 12 GV). Table.2 summarizes sources we observed in our campaign.

Objects	Observing Time	Date
SN1987A	1.8 hrs	1990/11/29
Cen A	7 hrs	1991/11/19, 12/03
PSR1509-58	3 hrs	1991/11/19
Galactic Center	0.5 hrs	1991/12/03
GX339-4	1.3 hrs	1991/12/03
Vela Pulsar	2.0hrs	1991/11/19

Table 2: Summary of the observation in the past three years.

A. *Background Spectrum at the Ceiling*

Figure 11 shows the background spectrum obtained at an altitude of 4g/cm^2 (37.8km). The figure demonstrates how effectively the anti-active shield which surrounds the particular counter in the compound eye configuration works. Using the hit information of the surrounding crystals, background events due to Compton scattering and/or 511keV annihilation in the material are clearly suppressed. In the figure, a broad peak at 368keV is conspicuous. It is mostly due to ^{152}Gd (abundance=0.2%, 2.14MeV α decay, half-life 1.1×10^{14}y). Bumps above 600keV in the spectrum are due to the radioactive contamination of the Thorium and the Uranium series in the GSO crystal. Note that ^{152}Gd is chemically inseparable, but others can be reduced by using higher purity materials.

The comparison with a MonteCarlo calculation is shown in Fig. 12. In the figure, the histogram shows the energy spectrum of Welcome-1 with the zenith angle of 30 degrees. The filled circles show the measured internal background obtained in the Pb(5cm)/Cu(5cm) cave in the laboratory. The dashed line shows the calculated detector response against incident photon flux with the power law index of 1.7. The broad line is the sum of backgrounds, which agrees with the observed spectrum. The intensity of the incident downward flux is calculated to be about $3.5 \times E^{-1.7}$ photons/cm^2/s/sr/keV.

As demonstrated in the figure, the low background rate was realized by the well-type phoswich counter. Background levels at 122keV and 511 keV are 1×10^{-4}/cm^2/s/keV and 4×10^{-5}/cm^2/s/keV, respectively. By our analysis, the spectrum below 300 keV is dominated by the flux entering through the aperture, whereas above 300 keV, internal background by isotopes in the detector

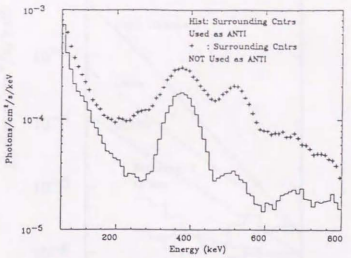

Figure 11: Back ground spectrum obtained with Welcome-1 at an altitude of 4g/cm^2. The spectrum taken with (hitstogram) and without (cross) the background reduction by the surrounding counters are shown.

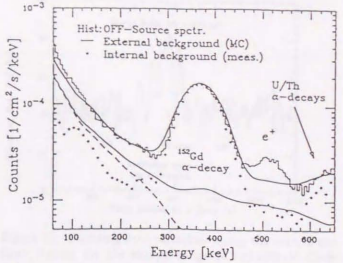

Figure 12: The observed back ground spectrum (histogram), the measured internal background (filled circles), the Monte-Carlo simulated external background (solid line), and sum of these backgrounds (broad line). The dashed line shows the background components entering through the opening aperture.

crystal is dominant. In the well-type phoswich counter and the compound eye configuration, background due to the activation of the crystal and/or the charged particles are shown to be suppressed effectively.

The sensitivity curve of the Welcome-1 calculated from the obtained background spectrum at an altitude of 4g/cm^2 is shown in Fig.13and 14. The curve represents the three standard deviation sensitivity that can be achieved in an observation of 10^4s (no attenuation by atmosphere). In Welcome-1, a sensitivity of $\sim$ a few $\times$ 10^{-6}/cm^2/s/keV and $\sim 10^{-4}$/cm^2/s by 10^4s observation can be attained for the continuum spectrum and line spectrum respectively.

B. *Flight Results*

In 1990, the counting rate variation from 100keV to 200 keV during our unplanned scan of the Crab Nebula is shown in Fig. 15. Since the star camera monitored the detector pointing every 2 sec, we know that the detector oscillated rapidly and the effective area varied during 63s shown in the figure. Note that the signal to background ratio is better than unity and this shows the excellent performance achieved by Welcome-1 in the hard X-ray region.

In 1991, we used Crab Nebula/Pulsar to verify the detector performance. The period of the observation was , however, devoted to the calibration of the pointing accuracy of the telescope using our star camera. In this calibration period, Crab Nebula/Pulsar was observed 10 - 13 degree away from the line of insight of the detector. Thus the effective area of the detector was reduced to 37-16% , which corresponds to 370 - 160 mCrab emission in Welcome1-1. Fig.16 shows the energy spectrum of Crab Nebula plus Pulsar in 1410s observation time when the telescope pointed 11 degrees away from Crab Nebula/Pulsar. The spectrum reasonably agree with the reported measurements by other experiments[8]. During the calibration period of 3300s which corresponds to a flux of $\sim$20% of Crab pulsar, the time profile of the pulsar is obtained (Fig.17) The location of the first peak in the time profile agrees well with that expected from radio observations at the solar system barycenter[9].

In order to obtain the energy spectrum from the direction from the objects, we must subtract the off-source spectrum from the on-source spectrum. In such a situation, the careful gain calibration is crucial throughout the observation period. The overall gain was calibrated for every counter by using the peak position of α-deacays of ^{152}Gd. To follow time variation at finer steps and yet to keep high statistical accuracy, the peak is integrated for 30 min, centered around time bins set at 5 min. steps. This procedure eliminates overcompensation of statistical fluctuations by gain adjustment. The resultant time variation of the overall gain is consistent with what is expected from the temperature dependence of the GSO light yield (-0.5%/degree) and the phototube gain. Furthermore, the area of the peak of ^{152}Gd is used to calculate the net live time of the detector system.

The high signal-to-background ratio of Welcome-1 is demonstrated in the Fig.18. In the figure, the on/off variation in Cen-A observation for 1991 flight. CenA is a brightest radio galaxy and identified as AGN. The emission at 100 keV roughly amounts to 100 mCrab. With Welcome-1, the high quality data can be obtained for a short observation time $\sim 10^4$s.

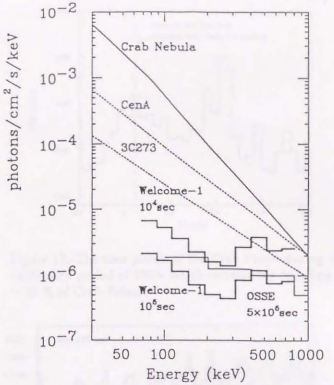

Figure 13: 3σ sensitivity of Welcome-1 for the continuum spectrum. X/γ-rays are assumed not to be attenuated by the atmosphere. The attenuation factors by 4mb atmosphere are 0.55 and 0.71 for 122keV and 511 keV, respectively.

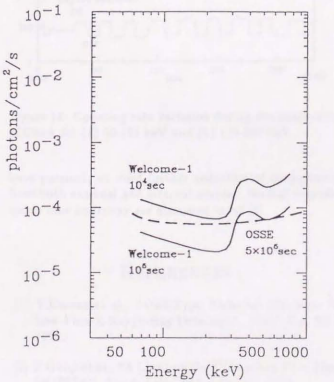

Figure 14: 3σ sensitivity of Welcome-1 for 10,000s for the line emission.

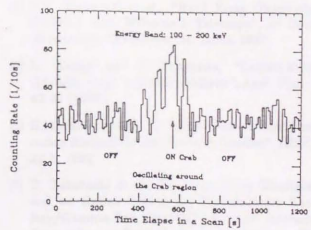

Figure 15: Counting rate variation during the scan of the Crab Nebula for the energy range of 100-200keV: Crab Nebula was observed just before the pointing operation.

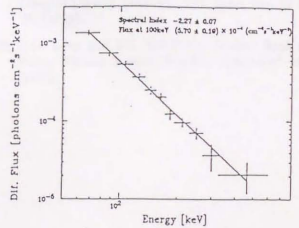

Figure 16: Energy Spectrum of Crab Nebula/Pulsar in 1410s observation time when the telescope pointed 11 degrees away from Crab Nebula/Pulsar (~300 mCrab emissions).

IV. Conclusion

We succeeded in developing a new hard X-ray telescope based on the well-type phoswich counter (Welcome-1) that reaches 3σ detection sensitivity as low as 5×10^{-6} photons/s/cm^2/keV (almost comparable with a CGRO-satellite observation) even in a balloon experiment where signals are attenuated to 1/2-1/3 by atmosphere and a typical observation time is only 10^4 seconds.

With Welcome-1, we set an upper limit on the ^{57}Co abundance and pulsar energy flow from SN1987A[2]. In 1991, we detected the pulsation from PSR1509-58 in our energy range. This pulsar is only the second pulsar detected in hard X-ray region after Crab pulsar. In the same campaign, we obtained high quality energy spectrum from Cen A (an active galactic nuclei) together with GX339-4 (a black hole candidate).

In order to achieve higher sensitivity along the line we

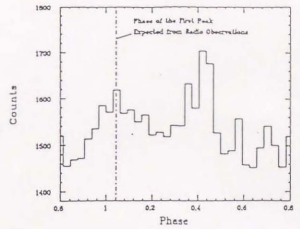

Figure 17: The time profile of the Crab Pulsar during the calibration period of 3300s which corresponds to a flux of ~ 20 % of Crab Pulsar.

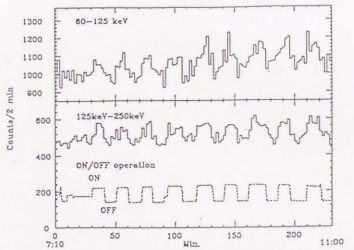

Figure 18: Counting rate variation during the observation of CenA for (a) 60-125 keV and (b) 125-250 keV.

have pursued, we need further reduction of backgrounds from both external and internal sources. Several improvements now underway are discussed in ref [1].

References

[1] T.Kamae et al., "Well-Type Phoswich Counters for Low-Flux X-Ray/γ-Ray Detection", *IEEE N.S.* 39 5, 1992.

[2] S.Gunji et al., "A Limit on the ^{57}Co γ-Ray Flux From SN1987A", *Ap. J. Lett.*, 397, L83-L86, 1992.

[3] T.Takahashi et al., "Hard X-ray Observation of Cen A and Break in the Spectrum", in *Compton Observatory Symposium*, St. Loius, 1992.

[4] N.Y. Yamasaki et al., "Hard X-ray Observation of GX339-4 with Welcome-1 Telescope", in *Compton Observatory Symposium*, St. Loius, 1992.

[5] K. Takagi and T. Fukazawa, "Cerium-activated Gd_2SiO_5 single crystal scintillator",*Appl. Phys. Lett.* 42 43 (1983).

[6] H.Murakami et al., "A Simple Pulse Shape Discrimination Method for the Phoswich Counter", *IEEE N.S.* 39 5, 1992.

[7] T. Takahashi et al., "A Pulse Shape Discriminator and an Online System for Balloon-Borne Hard X-Ray/Gamma-Ray Detector", in: *17th International Symposium on Space Technology and Science*, Tokyo, 1990.

[8] W.R. Cook et al.,"Recent Results of Gamma-ray Imaging Observations of the Galactic Center and Crab/A0535+26 Regions", *Adv. Space Res.* 11 8 (8) 191 (1991).

[9] A.G. Lyne and R.S. Pritchard, "Jodrell Bank Crab Pulsar Timing Results Monthly Ephemeris" March (1992).